MULTIPHYSICS COMPUTATIONS ON CELLULAR INTERACTION IN COMPLEX GEOMETRIES AND VORTEX-ACCELERATED VORTICITY DEPOSITION IN RICHTMYER-MESHKOV INSTABILITY

by

GAOZHU PENG

A dissertation submitted to the

Graduate School-New Brunswick

Rutgers, The State University of New Jersey

In partial fulfillment of the requirements

For the degree of

Doctor of Philosophy

Graduate Program in Mechanical and Aerospace Engineering

Written under the direction of

Professor Norman J. Zabusky

And approved by

_____

_____

_____

_____

New Brunswick, New Jersey

January, 2008

ABSTRACT OF THE DISSERTATION

MULTIPHYSICS COMPUTATIONS ON CELLULAR INTERACTION IN COMPLEX GEOMETRIES AND VORTEX ACCELERATED VORTICITY DEPOSITION IN RICHTMYER-MESHKOV INSTABILITY

By GAOZHU PENG

Dissertation Director:

Professor Norman J. Zabusky

The cellular interactions during leukocyte margination and adhesion cascade in cardiovascular microcirculations are multi-scale and multiphysics phenomena, involving fluid flow, cell mechanics, chemical reaction kinetics and transport, fluid structure interaction. The vascular network *in vivo* has rather complicated topology unlike straight and flat channels and pipes where most biological experiments *in vitro* and numerical simulations are carried. A computational framework is formulated towards a goal of building a virtual blood vessel system to simulate the hydrodynamic and kinetic interactions of blood cells in complex vascular geometries, including vascular network bifurcations and irregular shapes of the endothelial monolayer lining the blood vessel lumen *in vivo*. Mixed front tracking, immersed boundary and ghost cell methods are applied. The codes are benchmarked and validated with five selected problems. We find that the erythrocyte-leukocyte interaction, leukocyte-leukocyte interaction, and vascular geometries play important roles in leukocyte margination, initial tethering and adhesion to the vascular endothelium.

In part II of the dissertation, we studied the two-dimensional microscale Richtmyer-Meshkov interfaces and discovered the self-driven vortex-accelerated vorticity deposition (VAVD)

process. Opposite-signed secondary vorticity deposited by the VAVD is rolled into vortex double layers which are extremely unstable and lead to enhanced fluid mixing. The VAVD process examined and the new quantification procedure, the circulation rate of change, comprise a new vortex paradigm for examining the effect of specific initial conditions on the evolution of Richtmyer-Meshkov and Rayleigh-Taylor interfaces through intermediate times.

Acknowledgements

First I would like to thank my dissertation supervisor, Professor Norman J. Zabusky, for his constant support and encouragement throughout this research. His steadfast enthusiasm as well as physical insight, scientific computation and visualization experience make him the best possible director of this work. He has fostered my growth in U.S.A. since the first day I arrived.

I express my gratitude to my dissertation committee members: Professors A. Zebib, W. Craelius, and P. Bagchi for their review of this dissertation. Their comments help improve the clarity of this dissertation.

I really want to thank my former laboratory colleague Dr. Shuang Zhang with whom I had a lot of valuable discussions on Part II of this dissertation. He was also friendly and helped me during my early times in U.S.A. Special thanks to Mr. Zhanyu Sun who helped me a lot especially while I was not on campus.

I acknowledge discussions with many colleagues, including Dr. R. Samtaney, D.-K. Lee, J. Jacobs and H. Lin.

I thank our current graduate director Dr. Baruh and his assistant M Jenkins a for their considerate help when my PhD defense was delayed due to accidents when I just moved to Boston area in the spring of 2006.

I thank Rutgers University for the Raisler Graduate Fellowship awarded to me from 2000 to 2002. Also I express my thanks to CAIP center for computing and visualization facilities.

At last but not at least, I want to thank my wife Li Chen, my son Rich Peng, my daughter Rebecca Peng for their love, encouragement and patience during the tough periods. Li taught me never to give up and find peace even in trouble. I thank my parents-in-law and parents for their help in caring for Rich and Rebecca.

Dedications

To my parents and parents –in-law

To my wife, Li Chen

To my kids, Rich and Rebecca Peng

Table of Contents

List of Tables

List of Figures

Part I:

MULTIPHYSICS COMPUTATIONS ON CELLULAR INTERATIONS IN COMPLEX GEOMETRIES

Chapter 1

Introductions, Overview and Motivations

The understanding of interactions and control mechanisms in complex biological systems has become an increasingly important area of scientific inquiry as new technologies have been developed for measuring, representing and modeling the structure and function of living organisms in their dynamic environments. The coupling of fluid dynamics and biology at the level of the cell is an intensive area of investigation among them because of its critical role in immunology and cardiovascular diseases. Interest in this field has been driven both by the richness of the fluid-dynamic phenomena and by their fundamental biologic importance via mechanotransduction, a process mechanical effects are transduced to biological signals.

The original motivation to this part of the dissertation is the cellular interactions in cardiovascular system, especially cell adhesion. Cell adhesion is instrumental in diverse biological processes, including inflammation and thrombosis. Atherosclerosis is a progressive inflammatory disease where its early lesion begins with the recruitment of the leukocytes and its subendothelial accumulations inside blood vessel wall tissue layers, called intima (Figure 1.1). One distinctive feature of the atherosclerosis is that there are preferred sites of lesion formation within the heterogeneous blood vessel network and the lesion tends to form in regions where the blood flow is disturbed, such as bifurcations and large curvature regions.

In the cardiovascular system, cells are exposed to hemodynamic forces generated by dynamic blood flows. Cell adhesion and attachment to the blood vessel wall depend on the balances between the dispersive hydrodynamic forces (both pressure and shear force) and the adhesive forces governed by the chemical kinetic interactions of membrane-bound receptors and their ligands on the vascular wall. Cell adhesion has to be highly specific for proper regulation of

events to result in homeostatic inflammation and coagulation processes. Excessive activated leukocyte migration to healthy tissues can lead to unwanted disorders and pathologic conditions.

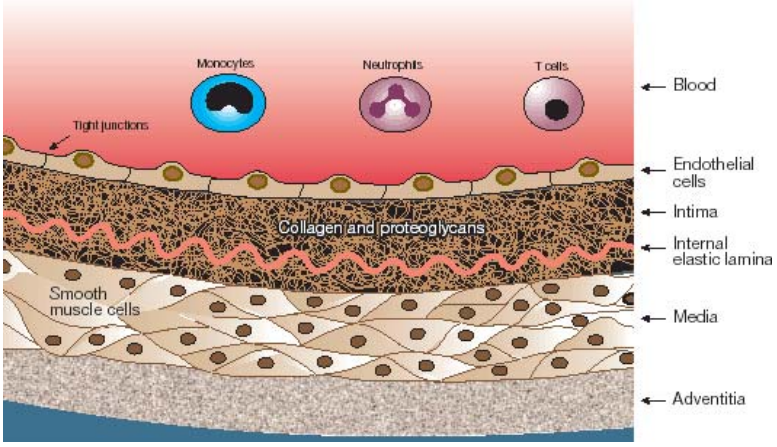

Figure 1.1 The anatomy of a blood vessel adapted from Fig 1 in Lusis (2001).

The cellular interactions involved in cell adhesion are multiphysical and multiscale phenomena, physics including blood flows (Newtonian or non-Newtonian fluid dynamics), adhesion and bond formations (chemical reaction), cell modeling and deformation (multifluid flows), interaction among blood cells and non-circulating endothelial cells lining the blood vessel lumen (fluid-structure interactions) in complex geometries mainly due to blood vessel network heterogeneity and irregular endothelial layer topology. Other physics can include the electrokinetics and gene signaling/transduction. The length scales involved can have several orders of magnitude difference, from adhesion molecule (nm), cell membrane (nm), cell itself (μm), and dimension of the blood vessel (μm to cm). Understanding this coupled multiphysical interplay at the multiscale levels is crucial for developing novel tissue-engineering-based approaches for therapeutic interventions in inflammatory and thrombotic disorders and for improving drug delivery targeting at the diseased areas. We will give a short introduction and review selected work on cellular interactions in the following sections.

1.1. Blood Circulation

Blood is a suspension of circulating cells in plasma with scattered proteins. Circulation cells are essentially the red blood cell (RBC) or erythrocytes, white blood cells (WBC) or leukocytes of various categories, and platelets. Red blood cells and leukocytes exert a strong influence on rheological properties of the blood as it flows through the circulation system. In large arteries and veins where the blood can be treated as a homogeneous fluid, their primary effects are an increase in the viscosity and, at low shear rates, non-Newtonian effects (Fung 1993).

In the microcirculations, however, where vessel dimension becomes comparable to that of a single cell, the effects are more complex and the blood cell interaction has to be taken into account. At the level of the arterioles and venules (diameters in the range of tens to a few hundred microns), the effective viscosity of blood exhibits an unusual pattern, first decreasing to a minimum of about 1 cPoise for vessels roughly 8 μm in diameter (Gaehtgens 1980), then rapidly increasing as the diameter is further reduced to a dimension small compared to that of the red cell. This has been known as the Fahraeus–Lindqvist effect, which is attributable to the appearance of a zone of lower red blood cell concentration near the vascular wall and, in the smallest capillaries, the need for red blood cells and leukocytes to deform in order to squeeze through the narrow lumens. The circulating blood cell interactions and blood cell interaction with the endothelial cell layer lining the blood vessel lumen also lead to a non-linear increase of viscosity with increasing hematocrit defined as the volume fraction of the red blood cells (Chien 1970). For reviews on red blood cells, see Skalak et al. (1981), Secomb (1995), and Pries et al. (1996). For reviews on blood flow in large blood vessels, see Ku (1997), Berger and Jou (2000), Taylor and Draney (2004).

Despite the small number of leukocytes relative to erythrocytes, leukocytes also contribute significantly to the blood flow rheology and resistance in microcirculations. This is mainly due to the fundamental difference between the mechanical properties of the leukocytes and the erythrocytes, and their mutual interactions (Helmke et al, 1997). When the leukocytes

adhere to the endothelial cells, the effect becomes even more significant (Skalak, 1972; Chapman and Cokelet 1998). In Chapman and Cokelet (1998), fixed rigid spheres were used to model the adherent leukocytes. In chapter 5, we model the cellular interactions involved and include modeling the adhesion kinetics and cell deformations.

1.2. Leukocyte Adhesion Cascade

Leukocyte margination and adhesion *in vivo* are characteristic features of an inflammatory response and have been associated with the pathogenesis of a number of inflammatory disease states such as atherosclerosis and myocardial infarction. The selective targeting of leukocytes to sites of inflammation is viewed as a multistage process of sequential involvement of distinct adhesion molecules on the leukocyte and endothelial cell (EC) surface that is dictated by the local fluid dynamic environment and cell interactions (Figure 1.2, Springer 1994): leukocyte first migrates close to the endothelial cell layer (margination), forms initial contact on the endothelial cells, adheres, rolls and then finally transmigrates to extravascular tissue space through the junctions formed between endothelial cells. The initial contact and rolling along the vessel wall are mediated primarily by selectins, molecules bound on the cell membranes to selectively form receptor-ligand bonds with their counterparts via chemical kinetic reaction and transport. Subsequent firm adhesion requires activation of integrins and binding to their ligand ICAM-1 on the EC surface. The margination, initial contact, adhesion and rolling are studied in current work, and the final stages of the leukocyte adhesion cascade involve chemical process and cell activation, which are outside the scope of current work.

The leukocyte adhesion has been under intensive experimental and computational studies during the two decades. The achievements in cell structure and adhesion kinetics measurements, together with the ever-growing high-performance computers, have facilitated the emergence of advanced computer modeling, which considered the fluid dynamics associated with the interaction between an adherent or rolling leukocyte and the adhesion receptors on the endothelium. These studies are complicated by the multiphysics nature of the flow, the

compliance of the interacting surface structures, fluid structure interaction, and chemical kinetic receptor-ligand dynamics. Computer modeling can be used to set up an ideal condition for cell adhesion study, which cannot be achieved easily in experiments. Deep physical insight can be obtained since the parameter space is reduced. Studies of cellular interactions in this field can also benefit the understanding of many other fields, such as multiphase flows, chemical surface reactions, and fluid structure interaction.

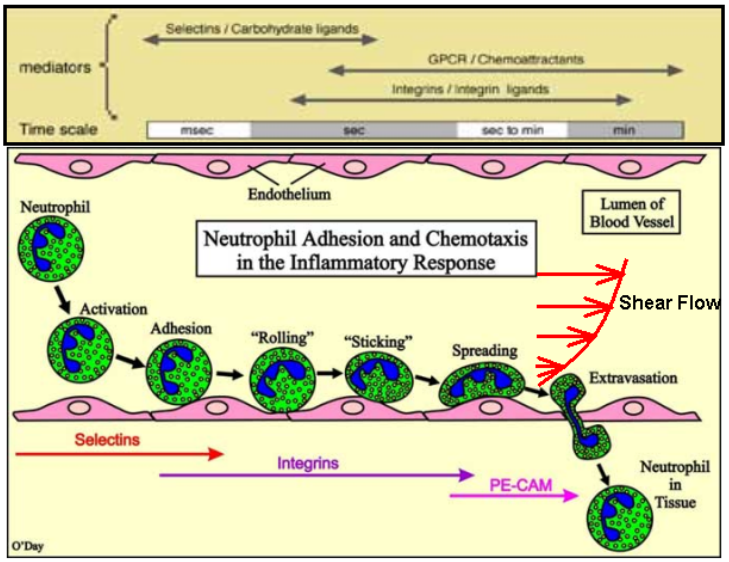

Figure 1.2 A cartoon sketch of the neutrophil adhesion cascade, a multi-stage process of cellular interaction, adhesion and activation events: margination, tethering, rolling, crawling, and transmigration (adapted from O'Day and Springer (1994)). The erythrocytes are not sketched.

1.2.1 Cell Deformation

A blood cell deforms under external force and torque. The mechanical properties of the cells at the passive state (without chemical activation) are determined by its compositions and structures as well as the surroundings with which the cells interact. As we know, the deformability of blood cells is critical in microcirculations where blood cells squeeze through them. The cell deformability also contributes the cell distribution: more deformable erythrocytes tend to move towards the

center of the blood vessel lumen and effectively drives the leukocyte towards the vascular wall (Melder et al, 2000).

Cell deformation in adhesion had been omitted in most of early work. In a series of studies, Hammer and co-workers (Hammer and Apte, 1992; Chang et al. 2000) have computed the viscous force and torque acting on a rigid sphere, as a model for leukocyte, near a planar wall from the mobility matrix based on the analytical solution from a sphere moving close to a wall in Stokes flow limit (Goldman et al. 1967) and the Bell model of receptor-ligand binding (Bell 1978). The cell deformation was neglected. However, these properties have been shown to have substantial effect on the adhesion process (Farrell and Lipowsky 1989; Damiano et al 1996; Dong et al. 1999; Dong and Lei 2000). Especially the side-view channel pioneered by Dong's group captures sharp image of the deformed leukocyte *in vitro*; Damiano et al (1996) and Lipowsky's group at Penn State University captured it *in vivo*. And the cell deformation has been proposed to one of the contributing mechanisms for cell rolling automatic stabilization (Chen and Springer 1999; Yago et al. 2002) and the threshold phenomenon in leukocyte-leukocyte interaction and leukocyte "string" formation where multiple leukocytes adhere each other to form a string-like structure (Alon et al 1996; Kadash et al. 2004). The effects of cell deformation are examined critically in current work.

1.2.2 Erythrocyte-Leukocyte Interaction

Leukocyte adhesion and rolling on the vascular endothelium layer require initial contact between leukocytes and the vessel wall. As a prerequisite, leukocytes need to migrate close enough to the vascular wall in order to form receptor-ligand bonds. The local fluid pattern and rheological mechanisms, especially erythrocyte and leukocyte interaction, have been experimentally observed to play significant roles (Abbitt and Nash, 2003; Melder et al 2000). But a clear understanding of how the red cells drive the leukocytes close to the vascular wall is lacking. A computer model of this type is built in current work.

After leukocytes adhere to the vascular wall, the red cells will continue to interact with these leukocytes. Especially in the context of sickle cell disease, Turhan et al (2001) discovered a new paradigm for the pathogenesis of sickle cell vasoocclusion in which the sickle red blood cells interact and bind to the adherent leukocytes and caused enhanced vasoocclusion. They proposed that vasoocclusion is a complex, sequential, multistep phenomenon involving different cellular interactions at different stages (1) endothelial activation by sickle erythrocyte or red cell (RBC), (2) leukocyte (WBC) adhesion to the endothelium, and (3) the direct interaction between sickle RBCs and adherent WBCs, which leads to reduced blood flow and tissue ischemia.

1.2.3 Leukocyte Interaction and String Formation

Besides the leukocyte adhesion to the endothelial cells, free-stream leukocyte can adhere to adherent leukocytes through a similar type of receptor-ligand bond system in the leukocyte-endothelium adhesion. When a free-stream leukocyte under hemodynamic shear flow gets close to an already adherent leukocyte on the endothelial cell, it adheres to the adherent leukocyte, slows down, changes its trajectory, and tends to bind on the endothelial cells downstream of the originally adherent leukocyte. This secondary capture of leukocyte and a positive feedback loop in the leukocyte adhesion have been shown both *in vivo* and *in vitro* experiments (Alon et al 1996; Kunkel et al 1998; Eriksson et al 2001; Mitchell et al 2000; Sperandio et al 2003; Hill et al 2003). This recruitment process plays a critical role of enhancing the leukocyte accumulation in inflammations. For example, this secondary capture occurs on atherosclerotic lesions (Hill et al 2003).

One interesting recent study by Kadash et al (2004) provides insight into the dynamics of neutrophil-neutrophil interaction and adhesion. They discovered a shear threshold phenomenon in neutrophil-neutrophil collision which the authors proposed a theory based on the neutrophil deformation. Cellular hydrodynamic interaction and adhesion with proper account of the cell deformations are examined in chapter 5.

1.3 Complex Geometries: Artery Bifurcations and Non-uniform Endothelial Cell Layer

In vivo microvascular networks are composed of short blood vessel segments, which exhibit irregular shapes and are linked by frequent bifurcations (Figure 1.3). The distinctive hemodynamic flow patterns in bifurcation regions impact the cell adhesion cascade. Within each short blood vessel segment, the endothelial cells to which the leukocyte adheres also have an irregular topology and extrude towards the blood lumen. This extrusion changes the local fluid pattern of the hemodynamic shear flow, redistributes the pressure and shear stresses acting on the cells and the molecular bonds.

Fluid dynamics in these complex geometries without accounting of circulating blood cells had been examined by several groups in the context of endothelium biological remodeling and mechanotransduction. Satcher et al. (1992) considered the endothelial surface to vary sinusoidally in height and examined the pressure and shear stress variations. At the same time, the variations in height were measured directly by using interference confocal microscopy (Sakurai et al. 1991), by combining confocal microscopy with fluorescence exclusion (Yamaguchi et al. 1993), and later by atomic-force microscopy of living endothelial cells, cultured under either no-flow or constant-flow conditions (Figure 1.4) (Barbee et al. 1994). These geometries and height variations were then used to calculate the changes in shear stresses. All of these studies clearly demonstrated that the variations in shear stresses due to surface waviness were significant, with the highest values of shear stresses acting on the protruding surfaces at the locations of endothelial cell nuclei. However none of these studies considered the possible role of the variations of shear stresses and pressure due to complex geometries in cellular interaction and adhesion. These are examined in chapters 5 and 6.

1.4. Motivations and Objectives

As reviewed above, several important aspects in cell interaction and adhesion are mostly omitted in current literature. Our current work addresses these issues. Multiple-cell interaction and

adhesion in planar and complex geometries are examined via high performance computing in current work. The blood cells are modeled with deformable liquid capsules enclosed with elastic membranes. Multiple-cell interactions are facilitated with the front tracking method. Complex geometries, endothelial topology and blood vessel bifurcations, are modeled with the ghost cell method without the need for computationally expensive deformed mesh. The effects of these factors are examined in chapters 5 and 6. Before we apply the codes developed to cellular interaction, we extensively validate and verify them in chapter 4.

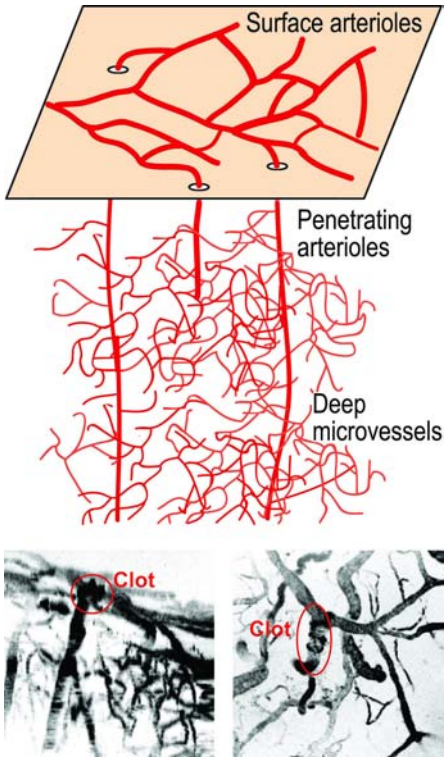

Figure 1.3 The complexity of the blood vessel network: Image showing network of blood vessels that supply the brain's gray matter along with images of clots in the penetrating arterioles (courtesy of David Kleinfeld, UCSD)

Multiphysics and multiscale computer modeling of the cellular interactions is important to understanding the physiological functions of the circulatory system such as the lymphocyte homing, and the pathophysiology of cardiovascular disease processes such as atherosclerosis

and sickle cell disease, and as well as to predictive medical treatment. Knowledge of the cell interactions is important for establishing guidelines for the design of drug particle size, drug particle mechanical/chemical properties, and receptor density for efficient drug delivery to the targeted inflammatory areas.

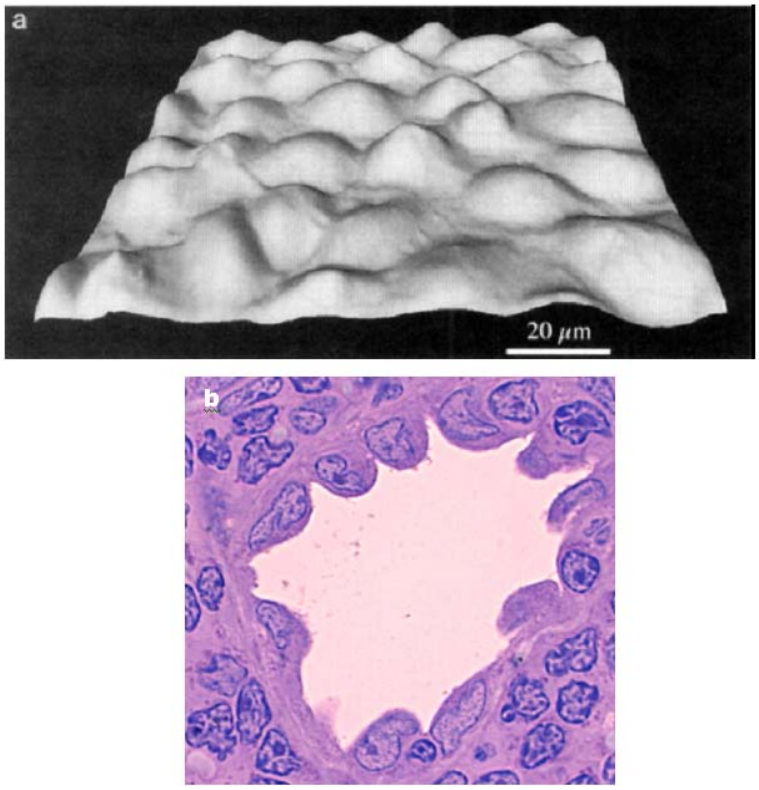

Figure 1.4 (a) Atomic force microscope images of confluent bovine arotic endothellal cells (Images courtesy of Barbee, Drexel University); (b) High endothelial cell venule, found in lymphoid tissue. Endothelial cells are tall and lack tight junctions. This facilitates entry of lymphocytes into lymphoid tissue from the blood (Image courtesy from Atlas of Histology, www.med.uiuc.edu/histo)

Chapter 2

Blood Cells:

Structure, Mechanics and Adhesion Models

Blood cells possess integrated structures that enable them to survive and function in dynamic physiological environments of hemodynamic shear flows, cellular interaction and adhesion. The mechanical properties of the cells are determined by their biological structures, biochemical activations and mechanical environments. To conduct a quantitative computational study of the cellular interactions in shear flows, it is an essential prerequisite to model the mechanical properties of the cells.

In cell adhesion, it has long been recognized that the leukocyte tethering and rolling are mediated principally by specific interactions between receptors and ligands involving a family of cell adhesion molecules called selectins (Springer 1994; Vestweber and Blanks 1999). We also need to understand and model the mechanics and kinetics of molecular receptor-ligand bonds, especially the formation and breakage rates and their shear stress dependence.

2.1 Blood Cell Structures

Blood cells have complex internal structures enclosed by the plasma membranes, which define the boundaries between the cytoplasm and extracellular environment (Alberts et al 2002). The plasma membrane consists of a continuous double layer of lipid molecules (lipid bilayers) with embedded and trans-membrane proteins. A pure lipid bilayer excluding any membrane proteins is self-sealing with a uniform thickness about 5nm. The most important feature of the lipid bilayer

itself is its incompressibility and fluidity. The fluid nature of a membrane is important in membrane protein mobility (e.g. selectin that mediates the cell adhesion) and cell deformation. The incompressibility of the lipid bilayer makes a vesicle conserves it membrane surface area besides its volume during its mechanical deformation and motion in hemodynamic shear flows (Kraus et al 1996; Seifert 1999; Abkarian et al 2002; Kantsler and Steinberg 2005; Kantsler et al 2007; Kessler et al 2007). Whereas the lipid bilayer defines the basic structure of blood cell membranes, the membrane proteins are principally responsible for the functionalities and mechanical properties of blood cell membranes. Membrane proteins and cell cytoskeleton form a supporting network on the endoside of the membrane.

The blood consists of mainly erythrocytes, leukocytes, platelets and proteins dispersed in the ambient fluid called plasma. The erythrocytes (red blood cells) are the most common type of blood cells, about 50% of the whole blood in volume. Erythrocytes are of disk shape. The diameter of a typical human erythrocyte disk is 6-8 μm (Figure 2.1). The red blood cell membrane separates the cytoplasm and the extracellular plasma. The cytoplasm contains the cytosol and proteins, including cytoskeleton. The erythrocyte does not have nucleus and functions mainly for oxygen delivery.

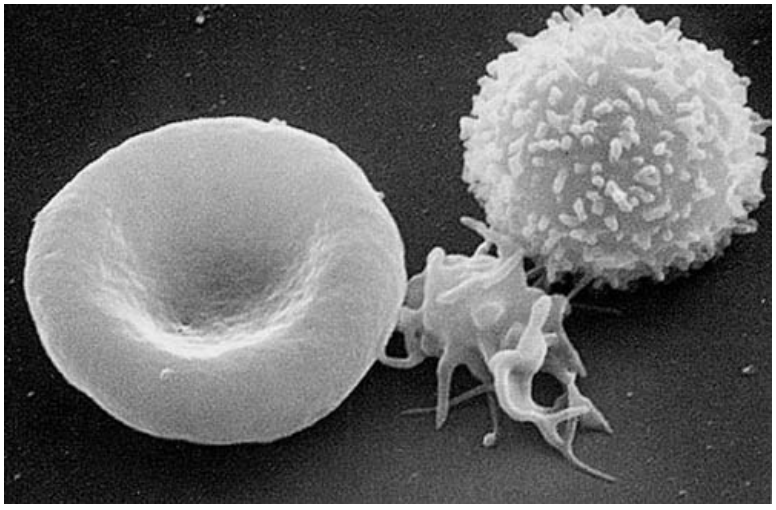

Figure 2.1 Juxtaposition of lymphocyte, erythrocyte and platelet.

Blood contains much fewer leukocytes, less than one percent of the blood in volume. Leukocytes exist in several types, including lymphocyte, monocyte and neutrophil. The lymphocytes are responsible for effective immune responses such as the production of antibodies in the process of lymphocyte recirculation and homing to lymphoid organs (Rosen 2004). Neutrophils and monocytes tend to move to sites of infection and inflammation for example in atherosclerosis (Segal 2005; Osterud and Bjorklid 2003), where they ingest bacteria and debris. All leukocytes under suspension have spherical shapes but differ in terms of overall dimension, size and internal structure. Their surfaces are covered by microvilli that protrude a short distance (0.3 ~ 0.4 μm) from the surface (Bruehl et al. 1996; Shao et al. 1998) and, because adhesion molecules are often localized to the tips of the microvilli, these can play a role in allowing the leukocyte to attach to a vascular in the early stages of the leukocyte adhesion cascade (von Andrian 1995), but do not effect the leukocyte rolling velocity (Stein et al 1999). Leukocyte membrane folding caused by the microvilli makes the actual membrane area about twice as its nominal or apparent area. One notable structure difference between the erythrocyte and leukocyte is that leukocyte has nucleus with the nucleus membrane separating the nucleus and cytoplasm, while the interior of erythrocyte is pretty much homogeneous. Leukocyte nucleus has much denser structures than the cytoplasm. Therefore its mechanical role can be important and hence need to be modeled.

2.2 Blood Cell Mechanical Models

The structure heterogeneities of a blood cell pose significant challenges for modeling the cell mechanical constitution law. In molecular scales, the cell cytoskeleton is considered and modeled as the main structure in various types of cells (Satcher and Dewey, 1996; Wang et al 1993; Ingber, 2003). This is important when studying how the external mechanical forces are transmitted to the cell interior and trigger subsequent biological signaling. We study the cell mechanics using the continuum approach instead. We are interested in applying and developing continuum mechanical models, which give apparent mechanical properties, to characterize

mechanical responses of blood cells subject to hemodynamic shear flows and chemical adhesions. Although providing less insight into the detailed molecular mechanical events, the continuum approach is more suitable to use in computing the mechanical properties of the cells if the biomechanical response at the cell level is the main interest.

2.2.1 Liquid Drop and Capsule Models

Erythrocytes and leukocytes behave like liquid drops in suspension and under hemodynamic shear flows. Erythrocytes and leukocytes can deform continuously to squeeze through microcirculations. In micropipette experiments, leukocytes can be absorbed into a micropipette with a smaller diameter when the pressure difference exceeds a certain threshold and recover its initial spherical shape upon release (Evans and Kukan, 1984). This fluid-like behavior motivated to develop a liquid drop model by Yeung and Evans (1989). In their model, the cell interior is assumed to be a homogeneous Newtonian viscous liquid with constant surface tension 0.02–0.04 $x10^{-3}$ N/m (Evans and Yeung, 1989; Needham and Hochmuth, 1992) until the area expansion limit (80–120%) is reached (Schmid-Schonbein et al., 1980; Evans and Yeung, 1989).

An erythrocyte has no cell nucleus and nearly homogeneous interior with little internal structures other than certain concentration of hemoglobin and other proteins, and a supporting protein network comprised largely of spectrin, a type of filamentous protein, on the endoface of the cell membrane. Hemoglobin makes the cell interior about four times more viscous than the blood plasma for a physiologically normal erythrocyte. The Newtonian drop model enclosed by nearly incompressible elastic membrane (see below) predicts quite satisfactory results for the erythrocyte deformation in shear flows. The bending stiffness can be readily included to smooth out nonphysical high curvature cusp formation (Secomb et al. 2001; Pozrikidis 2001)

The leukocyte interior consists of single or multiple nucleus compartments immersed in cytoplasm (see Figure 2.2). Lymphocyte has one single nucleus while neutrophil and monocyte can have multi-lobed nuclei. The cytoplasm includes the cytosol, cytoskeleton and various suspended organelles; the nuclei consist of nucleoplasm with genetic materials enclosed with an

envelope-like structure, which can be treated as another type of membrane, which is however not composed of the lipid bilayers as the plasma membrane. It has been demonstrated that the nucleus is stiffer and more viscous than the surrounding cytoplasm (Dong et al., 1991). One important phenomenon observed in micropipette experiments is that the apparent overall viscosity and stiffness vary continuously with the degree of deformation and the deformation rate (Dong et al., 1991; Dong and Skalak, 1992; Hochmuth et al., 1993). Therefore, an improved model accounting for the cell interior structural heterogeneity is needed.

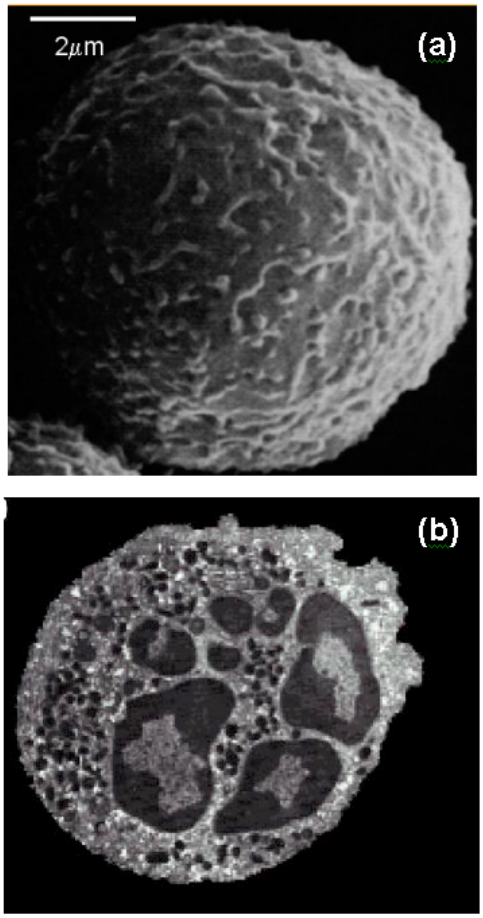

Figure 2.2(a) Scanning electron micrograph of neutrophils showing their spherical shape with numerous microvilli distributed over the surface. (b) Transmission electron micrograph showing the internal structure of a neutrophil including the multilobed nucleus, cortex, and cytoskeleton. Reproduced from Dong and Skalak (1992).

The compound liquid drop model was proposed (Dong et al. 1991; Hochmuth et al. 1993) to this end. It is treated as a three-layered structure (Figure 2.3). The plasma membrane and the ectoplasm, which make up the outer layer, have a thickness of 0.1 μm (Zhelev et al., 1994) and are under persistent tension with elastic properties. The middle layer is the endoplasm, which is fluid-like and is the softest region of the cell. The core layer is composed of the condensed region of the nucleus and surrounding cytoskeleton. The nuclear membrane is also under persistent tension (Tran-Son-Tay et al, 1994). The compound drop model has been applied to explain the vast disparity of estimated apparent viscosity of the leukocytes measured with different experimental methods or under different conditions. It is based on the fact that the nucleus is more viscous and stiffer than the surrounding cytoplasm and aims at explaining some nonlinear experimentally observed phenomena, which cannot be accounted for using the homogeneous drop model. Since it has been estimated that the nucleus is approximately 10 times more viscous than the cytoplasm (Dong et al., 1991), it is possible that the apparent viscosity represents nonlinear combination of the nucleus viscosity, cytoplasm viscosity, membrane stiffness and incompressibility. For example, at the beginning of the micropipette aspiration, the less viscous cytoplasm will be deformed preferentially, leading to a lower apparent viscosity (Kan et al., 1998). This may partially explain the rapid initial entry (Dong et al., 1988). As another example, in aspiration using larger micropipettes, the nucleus will not be deformed much and thus, the apparent viscosity will be lower. Conversely, the reverse is true when smaller micropipettes are used (Kan et al., 1998). This can explain why the apparent viscosity appears smaller in small deformation analysis (Hochmuth et al., 1993).

2.2.2 Cell Membrane Model

A cell membrane defines a physical boundary between the cell's internal compartment and its outer environment. Lipids and proteins are dominant components of membranes. One of the principal types of lipids in membranes is phospholipid. A phospholipid molecule has a polar

hydrophilic head group and two hydrophobic hydrocarbon tails. The hydrophilic heads shield the hydrophobic tails from the water surroundings due to the hydrophobic forces.

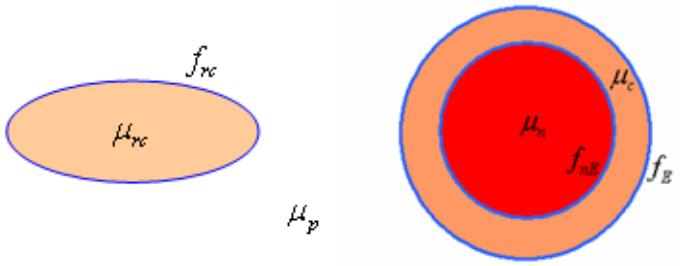

Figure 2.3 Homogeneous (lef) and compound (right) capsule models for erythrocyte and leukocyte, respectively. In both cases, the cytoplasm membranes separate the cell interior with different viscosities from the extracellular plasma space. For leukocytes, the cell interior is further divided into a dense nucleus with another membrane separating from the softer cytoplasm layer. Notations: μ_p μ_{rc} μ_c and μ_n denotes the viscosities for the exterior plasma, erythrocyte cytoplasm, leukocyte cytoplasm, leukocyte nucleus; f_{rc} f_E f_{nE} stands for the elastic force on the membranes.

The widely accepted model for cell membranes is the fluid mosaic model (Singer and Nicolson, 1972). In this model, the cell membrane is considered as a lipid bilayer where the lipid molecules can move freely in the membrane surface like fluid, while the proteins are embedded in the lipid bilayer. Some proteins are called integral membrane proteins because they traverse entirely in the lipid bilayer and play the role of information and matter communications between the interior of the cell and its outer environment. The others are called peripheral membrane proteins because they are partially embedded in the bilayer and accomplish other biological functions. Beneath the lipid membrane, the membrane cytoskeleton, a network of proteins, links with the proteins in the lipid membrane (Figure 2.4).

The first step to study the elasticity of cell membranes is to study the lipid bilayers. A good model for this is a vesicle, which consists of a pure lipid bilayer membrane enclosing certain protein solution (Kraus et al 1996; Seifert 1999; Abkarian et al 2002; Kantsler and Steinberg 2005; Kantsler et al 2007). However a true cell membrane is most simplified as lipid bilayers plus

membrane skeletons. The skeleton is a cross-linking protein network and joins to the bilayer at some points. Assume that each protein in the membrane skeleton has similar length which is much smaller than the whole size of the cell membrane, and that the membrane is locally two-dimensional uniform and homogenous. The thickness of the membrane is much smaller than the scale of the whole cell membrane. It is reasonable to describe the cell membrane by a surface.

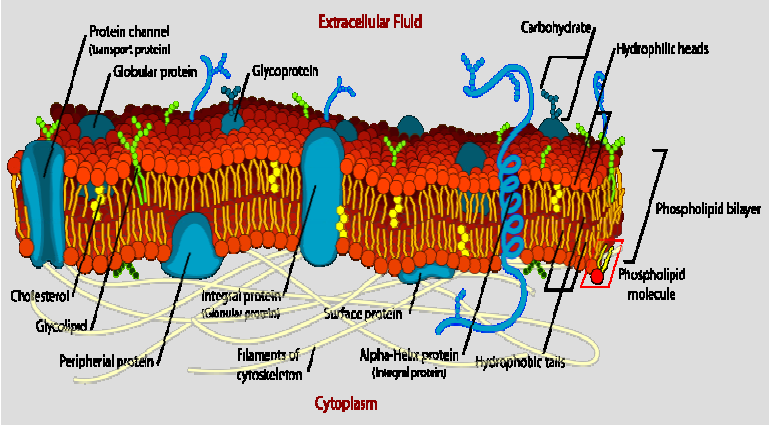

Figure 2.4 Cell membrane and fluid mosaic model (from wikipedia, 2007)

Salient features of the red and white cell membranes are: 1) capability for large deformations; 2) stress and strain history not affecting its equilibrium shape. These motivated to model them with elastic constitutive material. One notable difference between the cell and a simple liquid drop with constant surface is that the cell can reach an equilibrium shape unlike a liquid drop, which can break up into smaller ones under shear stretching (Scardovelli and Zaleski, 1999).

The red cell membrane can be modeled with nearly incompressible elastic thin structure (Evans and Skalak 1980; Fung 1993; Eggleton and Popel, 1998; Pozrikidis 2001). To derive constitutive relations for the elastic tensions, we introduce the principal stretches or extension ratios λ_1 and λ_2 respectively (Figure 2.5). The equilibrium equations can be derived by considering a smaller section of the membrane in the local curvilinear coordinates defined according to the principal stretching directions. To this end, we have two main choices reflecting

the assumed nature of the membrane. First, we may regard the membrane as a distinct two-dimensional elastic surface and express the principal stress resultants in terms of the surface strain energy function or the two-dimensional generalized stress-strain relationship (Fung and Tong, 1968; Evans and Skalak, 1979; Fung, 1993):

$$W = K(\lambda_1\lambda_2 - 1)^2 + E(\frac{\lambda_1^2 + \lambda_2^2}{2\lambda_1^2\lambda_2^2} - 1) \tag{2.1}$$

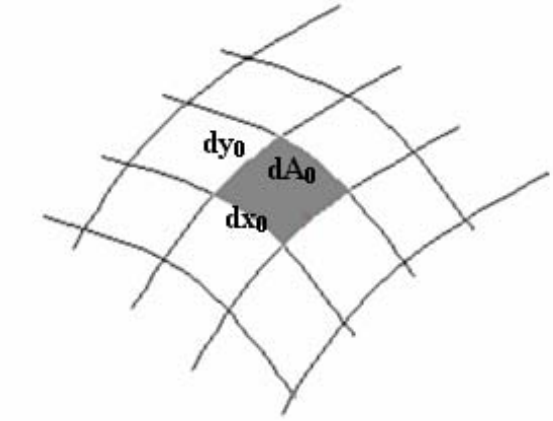

(a)

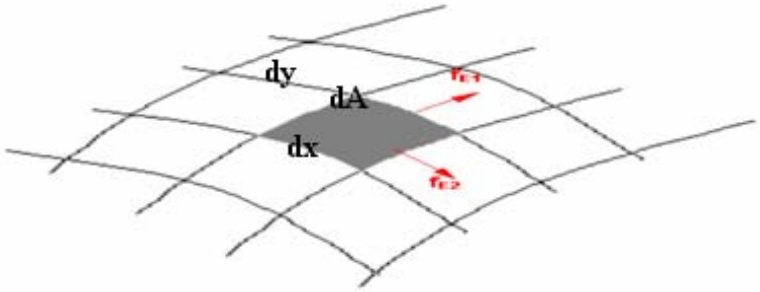

$$\lambda_1 = dx / dx_0, \lambda_2 = dy / dy_0$$

(b)

Figure 2.5 Deformation of a membrane infinitesimal section: (a) unstressed; (b) stressed.

where K is the membrane elastic modulus for area dilatation, and E is the membrane shear modulus. Alternatively, we may regard the membrane as a thin sheet or shell of a three-dimensional incompressible elastic material and introduce the volume strain invariants with the Mooney-Rivlin strain-energy function. A special case of the later is the neo-Hookean material model:

$$W = \frac{Eh}{6}(\lambda_1^2 + \lambda_2^2 + \lambda_1^{-2}\lambda_2^{-2} - 3) \tag{2.2}$$

where E is the Young's Modulus and h is the membrane thickness. Besides the shear and dilatation deformations, the bending moments can be taken into account by introducing the bending energy function based on Love's first approximation (Helfrich 1973; Pozrikidis 2001). The bending modulus is about 1.8e-12 dyne/cm, which is significantly smaller than the shear and area dilatation moduli, which are of the order of 1e-3 and 1e3. Since the membrane thickness is much smaller than the cell global scale, the bending stiffness can be ignored.

The leukocyte membrane is under persistent tension in its unstressed state. Also the leukocyte membrane has regular distributions of structural protrusions due to microvilli. The microvillus dimensions are much smaller compared with the leukocyte itself. It would be exceedingly difficult to model the topology of the microvilli. This requires special care to develop a leukocyte membrane model. Dong and Skalak (1988) proposed the following stress and strain relationship,

$$f_{Ei} = f_{E0} + E_a A(\lambda_1, \lambda_2) + E_s B_i(\lambda_1, \lambda_2) \tag{2.3}$$

where f_{E0} is a finite persistent tension; f_{E1} and f_{E2} are and two principal membrane tensions; E_a and E_s are area dilation and shear extension moduli, respectively. A and B_i are functions of principal stretch ratios, λ_1 and λ_2 , in the principal stretching tangent directions, which characterize the isotropic and anisotropic elastic deformation, respectively, which are suggested as (Dong and Skalak, 1992; Fung 1993) as,

$$A(\lambda_1,\lambda_2)=(\lambda_1\lambda_2-1)^n$$
$$B_i(\lambda_1,\lambda_2)=\frac{1}{2\lambda_1\lambda_2}(\lambda_i^2+\frac{1}{\lambda_i^2}) \tag{2.4}$$

where $n\geq 1$ usually to account for the leukocyte membrane folding caused by the microvilli. A large value of n (=29) is necessary to take into account the fact that the apparent leukocyte membrane surface area is about half of the actual membrane area. A large exponent n implies that the membrane can hardly be stretched when the area stretch ratio is larger than 2, the ratio of the actual leukocyte membrane area and the nominal one without accounting for the leukocyte microvilli. In another word, the area dilation resistance is nearly zero when the area expansion is less than 2 and increases in power when it becomes greater than 2. For two dimensions (2D), we set $\lambda_1=\lambda,\ \lambda_2=1.$

$$\begin{aligned} f_E &= f_{E0}+E_aA(\lambda)+E_sB(\lambda) \\ &= f_{E0}+E_a(\lambda-1)^n+\frac{E_s}{2}(\lambda-\lambda^{-3}) \end{aligned} \tag{2.5}$$

In our computations, we use the following parameters unless otherwise specified

$$f_{E,0}=0.12\ \text{dy n/cm},\ E_a=0.01\ \text{dyn/cm},\ E_s=0.14\ \text{dyn/cm} \tag{2.6}$$

which gave good agreement with Schmid-Schonbein et al. (1980). We normalize the parameters with the cell radius, (wall) shear rate, and blood plasma viscosity:

$$\frac{1}{\text{Re}}\left[\frac{f_{E0}}{\mu_p\dot{\gamma}a}+\frac{E_a}{\mu_p\dot{\gamma}a}(\lambda-1)^n+\frac{E_s}{\mu_p\dot{\gamma}a}(\lambda-\lambda^{-3})\right]\boldsymbol{\tau} \tag{2.7}$$

We denote the dimensionless parameters as following:

$$Gc_0=\frac{\mu_p\dot{\gamma}a}{f_{E0}},Gc_s=\frac{\mu_p\dot{\gamma}a}{E_s},Gc_a\frac{\mu_p\dot{\gamma}a}{E_a} \tag{2.8}$$

They are important and determine the relative importance of viscous force to the elastic membrane forces and bond force. $(f_{E,0},\ E_a, E_s)/\mu_p\dot{\gamma}a$. For the leukocyte nucleus membrane, quantitative studies are mainly missing to the author's best knowledge. To reduce the modeling parameter space, we take a simplified version of leukocyte membrane model and adopted,

$$f_{nEi} = f_{nE0} + E_{na}A(\lambda_1, \lambda_2) \tag{2.9}$$

with n = 1 in (2.2). In two dimensions, it reads

$$f_{nE} = f_{nE0} + E_{na}(\lambda - 1) \tag{2.10}$$

From Tran-Son-Tay et al. 1994, we take,

$$f_{E0} = 0.04\ \ dyne/cm, \qquad E_a = 2\ \ dyne/cm \tag{2.11}$$

and their normalizations are as following:

$$\frac{1}{\mathrm{Re}}\left[\frac{f_{E0}}{\mu_p\dot{\gamma}a} + \frac{E_a}{\mu_p\dot{\gamma}a}(\lambda - 1)\right]\boldsymbol{\tau} \tag{2.12}$$

There are many other types of cell models proposed, including elastic and viscoelastic solid models, and biphasic models. However the liquid capsule models are so far the most successful models which have given many satisfactory results compared with experiments. In most of our computations, this is adopted. For an overview of different cell mechanical models, please see the review by Lim et al (2006).

Let us comment on the blood vascular wall before we turn to the cell adhesion modeling in next section. The endothelial cells lining the endoface of blood vascular wall are important to cell adhesion in the leukocyte-endothelial adhesion. Selectins or selectin ligands are located on the endothelial surfaces and formed the molecular bonds with the leukocytes. The mechanics of the endothelium has been studied by Fung and Liu (1993). The deformability of the endothelial

cells is much less than the blood cells including erythrocytes and leukocytes (Sato et al 1986; Janmey et al 1991). We assume the endothelial behaves as a non-deformable solid wall to reduce the parameter space in our studies. Similarly, we neglect the effects of the up-to-now controversial endothelial surface layer, which covers the surface of endothelium (Vink et al; Pries et al. 2000; Squire et al 2003; Weinbaum et al. 2003).

2.3 Microscopic Kinetics and Mechanics of Cell Adhesion

The adhesion of blood cells to the blood vascular wall and their mutual adhesions are of crucial importance in governing a range of cell functions in normal physiological lymphocyte recirculation (Butcher and Picker, 1996), pathological inflammatory diseases (Ross 1999; Lusis 2000; Libby 2002) and biotechnological drug delivery (Eniola et al. 2002; Ehrhardt et al 2004). It is a multiphysical process involving the dynamic cell motion in hemodynamic shear flow and chemical reaction forming the specific receptor-ligand molecular bonds.

The adhesion of leukocytes mainly occurs in post-capillary expansion venules where hemodynamic shear stresses are minimized and the blood cell interactions are augmented. The leukocyte adhesion cascade is a multi-step process (Figure 1.2). The critical first step is the transient tethering of a flowing leukocyte to the vessel wall. This tether is not much stable itself and the cell either detaches back into the fluid stream or begins to roll along the vessel wall. Rolling is a form of reversible adhesion where new adhesive bonds have to be continuously formed at the leading edge of the cell-cell contact zone matched by rapid breaking of the at the trailing edge as (Lawrence and Springer 1991). If the bond formation and dissociation are well balanced, the leukocyte can roll for a period long enough to become activated by inflammatory chemokines or lipid mediators in order to arrest, spread and finally transmigrate into the underlying blood vascular tissue through the endothelial-endothelial junctions; otherwise, it can be detached and return to the blood stream again. This multistep process of tethering, rolling, firm adhesion, crawling, and transendothelial migration requires the coordinated expression of different adhesion and signaling molecules (Butcher, 1991; Springer 1994).

The tethering and rolling adhesion of leukocytes, which are essential prerequisites on arrest and subsequent transmigration into tissues, are mediated specifically by a group of three specialized cell-adhesion molecules called selectins: L-selectin, P-selectin and E-selectin (Lawrence and Springer 1991; Kansas, 1996; Vestweber and Blanks, 1999). L-selectin, expressed on leukocytes, binds to ligands on endothelial cells and on other leukocytes (leukocyte-endothelial adhesion; leukocyte-leukocyte adhesion); P-selectin, expressed on activated endothelial cells, binds to ligands on leukocytes (leukocyte-endothelial adhesion); E-selectin, expressed on activated endothelial cells, binds to ligands on leukocytes (leukocyte-endothelial adhesion). Figure 2.6 sketches the selectins and their ligands involved in leukocyte-endothelial and leukocyte-leukocyte adhesions (Vestweber and Blanks 1999; McEver 2002). These selections can form bonds by themselves or coordinated to strengthen the blonds (Springer 1990). Note, the selectin and ligand are modeled as elastic springs without account for their molecular structures as indicated in Figure 2.6.

Cell adhesion, a multiphysical phenomenon, has attracted much attention and interest from multiple disciplines including biochemistry, bioengineering, biophysics and cell biology. Several mathematical models have been proposed for describing the interaction of the leukocyte with the endothelium cells. They can be classified into three classes based on thermodynamics equilibrium (Bell et al 1984), mechanical peeling (Skalak et al 1981; Evans 1985), and reaction kinetics (Bell 1978; Hammer and Lauffenburger, 1987; Dembo et al 1988; Evans and Ritchie, 1997):

1). Mechanical peeling analysis: It relates adhesion energy density, γ, defined as the mechanical work required to separate a unit are of the adherent surface, to the work done by external forces and the energy stored in and viscously dissipated by the deformed cell.

2). Thermodynamic equilibrium: The adhesion between the cell and the substrate is analyzed by studying the equilibrium of the free energy or chemical potentials and the strain energy accounting for the external forces at a given instant in time.

3). Specific reaction Kinetics: The kinetic models come from the fundamental biochemical reaction kinetics governing the specific receptor-ligand interactions in cell adhesions. It includes

describing adhesive interactions using chemical reaction kinetics and defining the kinetic rates as functions of the force applied on the bonds (Bell 1978; Dembo et al 1988; Evans and Ritchie 1997).

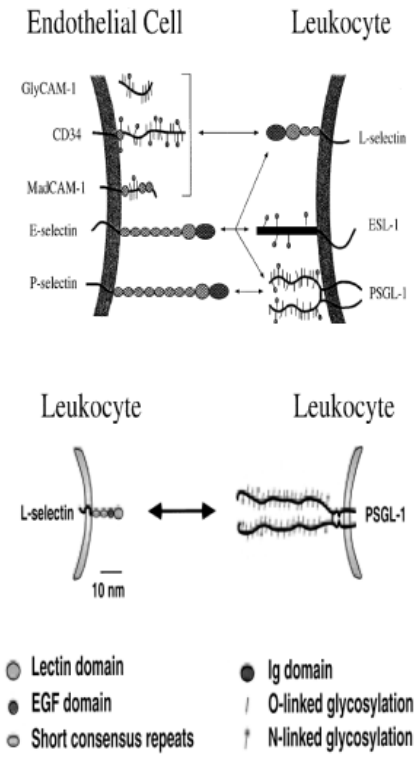

Figure 2.6 Selectins and their ligands in leukocyte adhesions for: (a) leukocyte-endothelial adhesion; (b) leukocyte-leukocyte adhesion (Adapted from Vestweber and Blanks, 1999).

There has been a paradigm shift in the cell adhesion to the kinetic concept, which has its foundations on the specific non-covalent interactions between the receptors and ligands mediating the adhesion. And the kinetics models define the coupling of kinetics and mechanics via the force-dependent kinetic rates, which need to be modeled. It is well suited to be applied to the quantitative computational (and experimental) studies. In the computational fluid dynamic studies of leukocyte-endothelial and leukocyte-leukocyte adhesions under shear flow, stress on the molecular bonds can be computed from the detailed fluid field and bond distributions and this force from bonds balances with the hemodynamic force and torque applied to the cell from fluid

flow to determine how likely, how fast, how strongly a cell adheres. Significant progress has been made toward understanding the receptor-mediated cell adhesion that is involved in the leukocyte-the endothelium interactions as reviewed in Evans (1993), Lauffenburger and Linderman (1993), Hammer and Tirrell (1996), Bongrand (1999) and Zhu (2000).

In the absence of external force, receptors and ligands associate to form bonds with an intrinsic association rate of k_f^0; the bonds can dissociate with a dissociation rate of k_r^0. The equilibrium state of the reaction kinetics is determined by the affinity constant K0 defined as the ratio of the association rate and the dissociation rate. However these kinetic properties are not adequate to determine the leukocyte adhesion in vivo where the leukocytes are subjected to continuous fluid shear stress and pressure load from the hemodynamic blood flow (van der Merwe 1999). The mechanical properties of the molecular interactions and cellular interactions must be properly taken into account (Alon et al. 1995; Ferger et al 1996; Alon et al. 1997; Lawrence et al 1997; Chen and Springer 1999; Yago et al 2002).

An important property of receptor–ligand bonds that determines adhesion is the bond strength. Drawing from the kinetic theory of the strength of solids, it can be assumed that although the forward rate should not be affected by an applied force, the reverse rate constant (and thus the affinity) will vary exponentially with force (Bell 1978),

$$k_r = k_r^0 e^{(r_0 f / k_B T)} \tag{2.13}$$

where f is the applied force to the bond, k_B is the Boltzmann constant, T is the temperature, and r_0 is the reactive compliance which can be understood by make an analogy of binding energy to an equivalent potential energy well. The reactive compliance defines the nature of the bonds (Dembo et al 1988): 1) $r_0 > 0$, the bond is called “slip” bond implying that the reverse rate increases as the applied force on the bond increases; 2) $r_0 = 0$, the bond is called “ideal” bond with force-independent reverse rate; 3) $r_0 < 0$, the bond is called “catch” bond implying that the bond gets strengthened as the force is applied on the bond (Marshall et al. 2003; Thomas et al

2002). Alternative approaches have been applied to describe the relationship between the dissociation rate and the force. Dembo et al (1988) models the receptor-ligand bond as a spring. In this case, the affinity will decrease as the bond length moves away from its equilibrium length according to the Boltzmann distribution,

$$K = K^0 \exp\left(\frac{-\sigma(l-l_0)^2}{2k_BT}\right) \tag{2.14}$$

and for the association and disassociation rates, they are defined as following,

$$k_r = k_{r0} \exp\left(\frac{(\sigma-\sigma_{ts})(l-l_0)^2}{2k_BT}\right) \tag{2.15a}$$

$$k_f = k_{f0} \exp\left(-\frac{\sigma_{ts}(l-l_0)^2}{2k_BT}\right) \tag{2.15b}$$

where σ and σ_{ts} are the regular and transitional spring constants of the bond, respectively; l^0 and l are the stress-free and stretched bond separation distances, respectively. A third and more advanced model developed by Evans and Ritchie (1997) uses the Kramers transition state theory and accounts for the loading rate of a mechanical force. This model reduces to the Bell's and spring model of Dembo et al in the limit of fast loading of which the hydrodynamic flow load is typical. Chen and Springer (2001) made significant efforts to test different models on how force affects the bond dissociation by plotting the histogram of the unbound cells vs the tether duration at different shear stresses. Then they fitted the models mentioned above and variations of the Evan-Ritchie model to the experimental data. They are all reported to predict the dissociation rates well especially at intermediate to large shear stresses.

We found that the Dembo et al (1988) spring model is more straightforward to include in computational studies. The bond association and dissociation rates are derived from the Boltzmann distribution and the bond itself can be modeled with an elastic spring which is consistent with the assumption. Based on this spring model for the bond, the bond force f_b can be computed as,

$$f_b = \sigma(l - l_0) \tag{2.16}$$

and

$$F_b = n_b f_b \tag{2.17}$$

Where F_b is the total bond force, and n_b is the number of bonds. The reaction kinetic system governing the association and dissociation of receptor-ligand bonds is given as,

$$\frac{\partial N_b}{\partial t} = k_f (N_r - N_b)(N_l - N_b) - k_r N_b \tag{2.18}$$

where N_b is the receptor-ligand bond density, k_r and k_f are the association and dissociation rates defined in Equation 2.15 respectively, N_l is the initial ligand density, and N_r is the initial receptor density. In the present study, a receptor-ligand bond will be considered broken if the bond density reduces to a critical bond density, N_{bc}, as defined by Dembo et al (1988),

$$N_{bc} = 10^{-4} N_{b0} \tag{2.19}$$

where the initial equilibrium bond density is computed from Equation 2.18 as following,

$$k_{f0}(N_r - N_{b0})(N_l - N_{b0}) - k_{r0} N_{b0} = 0 \tag{2.20}$$

We use the same characteristic scales used in the macroscopic equations above to make the microscopic model dimensionless. The dimensionless form of the bond density equation remains in the same form. Similarly, the bond force formula keeps with the variables made dimensionless correspondingly.

$$\frac{\partial N_b^*}{\partial t^*} = k_f^* (N_r^* - N_b^*)(N_l^* - N_b^*) - k_r^* N_b^* \tag{2.21}$$

$$f_b^* = \sigma^*(l^* - l_0^*) \tag{2.22}$$

$$k_r^* = k_{r0}^* \exp\left(C_r(l^* - l_0^*)^2\right) \tag{2.23}$$

$$k_f^* = k_{f0}^* \exp\left(-C_f(l^* - l_0^*)^2\right) \tag{2.24}$$

Where

$$C_r = \frac{a^2(\sigma - \sigma_{ts})}{2k_BT}, \quad \text{and} \quad C_f = \frac{a^2\sigma_{ts}}{2k_BT} \tag{2.25}$$

These kinetics equations will be solved simultaneously with the fluid equations and the mechanics of cells, which is the focus of the next chapter.

Chapter 3

Computational Methods

In this chapter, we summarize the numerical methods developed carefully for computations of cellular interactions in complex geometries. It consists of five sections: 3.1) The velocity-pressure projection method is used to solve the Navier-Stokes equations on a fully staggered Cartesian grid and the skew-symmetric second order conservative schemes are used; 3.2) The motions and interactions of cells with membranes separating different fluids are computed with the front tracking method; 3.3) Cell membrane mechanics computations in two and three dimensions; 3.4) A ghost cell immersed boundary technique is applied to the computation of flows in complex geometry within a fixed Cartesian grid; 3.5) How do we compute the bond distribution governing kinetic equation and the bond forces. Such a unifying combination of different types of numerical method is needed to compute the long time dynamics of cellular interaction and adhesion in complex geometries. The mix of ghost cell and front tracking methods is our main innovation here. It has efficiency of computing multiphase flow in complex geometries with a fixed Cartesian grid without the computationally expensive curvilinear coordinate transformation involved in a body-fitted grid.

3.1 Navier-Stokes Solver

The cellular fluid motions are governed by the transient incompressible Navier-Stokes equations

$$\nabla \bullet \mathbf{u} = 0 \tag{3.1}$$

$$\frac{\partial \rho \mathbf{u}}{\partial t} + \nabla \bullet (\rho \mathbf{u}\mathbf{u}) = -\nabla p + \nabla \bullet (2\mu \mathbf{S}) + \mathbf{F} \tag{3.2}$$

where **F** is the volumetric force and **S** is the viscous stress tensor defined as following,

$$\mathbf{S}_{ij} = (u_{j,i} + u_{i,j})/2 \tag{3.3}$$

It is convenient to normalize the Navier-Stokes equation in order to study the fundamental scaling with critical dimensionless physical parameters. The Navier-Stokes equations can be made dimensionless based on fundamental scales in cellular fluid mechanics: cell radius a, (wall) shear rate $\dot{\gamma}$, and plasma viscosity μ_p. In other word, we choose the cell radius a as characteristic length scale, inverse (wall) shear rate $1/\dot{\gamma}$ as characteristic time scale, and $a\mu_p/\dot{\gamma}$ as characteristic mass scale. After some rearrangement, we have the following dimensionless Navier-Stokes equation,

$$\nabla \bullet \mathbf{u}^* = 0 \tag{3.4}$$

$$\frac{\partial \mathbf{u}^*}{\partial t^*} + \mathbf{u}^* \bullet \nabla \mathbf{u}^* = -\nabla p^* + \frac{1}{\mathrm{Re}} \nabla \bullet (\mu^* \nabla \mathbf{u}^* + \mu^* (\nabla \mathbf{u}^*)^T) + \mathbf{F}^*. \tag{3.5}$$

We drop the star superscripts from here on to simplify the notations. The volumetric force **F** includes the local source force contributed from the cell membrane in front tracking method and/or the virtual force from the ghost cell immersed boundary technique which is applied to enforce the boundary conditions on the blood vascular wall embedded in a fixed Cartesian grid. We will discuss these methods after giving the detail about the time-marching and spatial discretization scheme used for computing the Navier-Stokes equations.

The method of lines with the four-step velocity-pressure fractional step/projection scheme is applied to march the transient Navier-Stokes equations in time (Choi and Moin, 1994; Fergizer and Peric, 1999),

$$\frac{\tilde{u}_i - u_i^n}{\Delta t} + \left[\frac{3}{2}\left(\frac{\partial}{\partial x_j}(u_i u_j) - F_i - \frac{\partial}{\partial x_j}(\nu \frac{\partial u_j}{\partial x_i}) \right)^n - \frac{1}{2}\left(\frac{\partial}{\partial x_j}(u_i u_j) - F_i - \frac{\partial}{\partial x_j}(\nu \frac{\partial u_j}{\partial x_i}) \right)^{n-1} \right]$$

$$= -\frac{\partial p^n}{\partial x_i} + \frac{1}{2\,\mathrm{Re}}\left(\frac{\partial}{\partial x_j}(\nu^n \frac{\partial \tilde{u}_i}{\partial x_j}) + \frac{\partial}{\partial x_j}(\nu^n \frac{\partial u_i^n}{\partial x_j}) \right) \qquad (3.6a)$$

$$\frac{u_i^* - \tilde{u}_i}{\Delta t} = \frac{\partial p^n}{\partial x_i} \qquad (3.6b)$$

$$\frac{\partial^2 p^{n+1}}{\partial x_i \partial x_i} = \frac{1}{\Delta t}\frac{\partial u_i^*}{\partial x_i} \qquad (3.6c)$$

$$\frac{u_i^{n+1} - u_i^*}{\Delta t} = -\frac{\partial p^{n+1}}{\partial x_i} \qquad (3.6d)$$

where superscripts $n-1$, n and $n+1$ denote the variables (velocity and pressure) at time steps t^{n-1}, t^n and t^{n+1}, respectively; $\tilde{u}_i$ and u_i^* are intermediate velocities obtained with and without the pressure term, respectively. The explicit second–order Adams-Bashforth scheme is used for the nonlinear convective terms, source terms and off-diagonal viscous terms; and the fully implicit Crank-Nicholson scheme is used for the diagonal viscous term. These ensure the second order accuracy of the whole discretization. Please note, that this is important to treat the diagonal viscous term implicit since the viscous diffusion stability limit is much more restrictive than the convection CFL condition in micro scale cellular fluid mechanics. The use of explicit pressure gradient term at the time step n in Equation (3.6a) is important and helps to eliminate the need for special treatment of the intermediate velocity boundary condition within the framework of a full second-order time marching scheme (Kim and Moin, 1985). The pressure equation of Poison type (3.6c), which projects the velocity to a solenoidal field, is solved by implicit direct inversion. It works efficiently for fluid flows with constant density in the whole computational domain, which is true for neutrally buoyant blood cell motions in cardiovascular system (Smith et al 2003). It makes use of the fact that we can store and invert the system matrix during the assembly stage, and reuse it without any change for every time step of the full computations.

The Navier-Stokes equations are spatially discretized on a fully staggered or the so-called Marker and Cell grid (MAC) as shown Figure 3.1 for a 2D sketch to avoid the non-physical oscillations of the pressure field from the pressure Poisson Equation 3.6c to enforce the zero-divergence or incompressibility of the velocity field. This is due to the odd-even decoupling when using the central difference on a regular and collocated grid for the Poisson equation (Ferizger and Peric 1999).

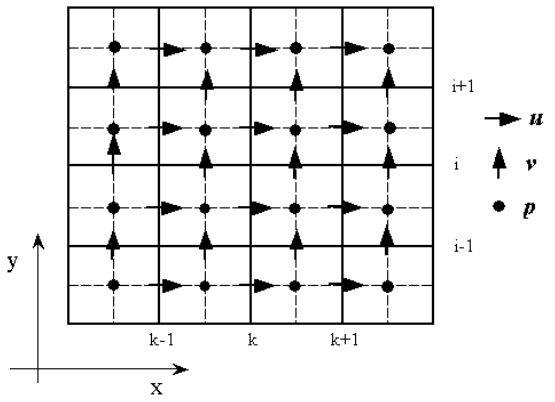

Figure 3.1 Staggered grid systems: the velocities are defined on the edges of the computational cells, and pressure is defined on the center of the cell.

Special care is taken to apply the proper skew-symmetric second order accurate conservative scheme to the convection terms in a fully staggered grid system (Figure 3.2). Morinishi et al (1998) examined divergence, advective, skew-symmetric, and rotational schemes in regular, staggered, and collocated grid systems with regard to their conservation properties. The proper conservation properties of the skew-symmetric convective scheme proper were discussed and applied in Lai and Peskin (2000) where they developed the formally second order immersed boundary method and used it for computing flow around a rigid cylinder. We apply these second-order accurate skew-symmetric convective schemes in a fully staggered grid system. That is necessary for long time computations where the proper conservations become critical.

We use three kinds of boundary conditions for the velocity field: The periodic boundary condition (Couette or linear shear flow), the Dirichlet boundary condition (Couette or Poiseuille flow), and Neumann boundary condition (outlet/symmetry). Consistent with these boundary

conditions for the velocity, the boundary conditions for the pressure are periodic boundary condition, Neumann boundary condition, and the Dirichlet boundary condition, respectively. The use of the fully staggered grid makes the treatment of the pressure boundary condition easier compared with the regular grid method where the pressure values on the boundaries have to be computed explicitly with non-trivial extrapolations.

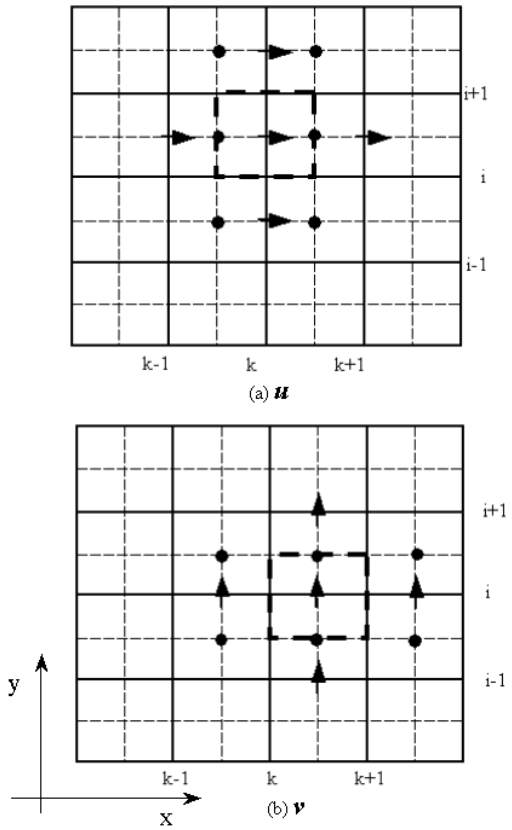

Figure 3.2 Dashed rectangles represent the computational stencils for: (a) the x-direction momentum discretization; (b) the y-direction momentum discretization.

The first step of the fraction steps, Equation (3.6a) is solved with an approximate factorization method. After multiplying both sides with the time step size Δt, moving the explicit terms to the right hand side of the equation and denoting them as RHS, we arrive at

$$\left[1-\frac{\Delta t}{2\,\mathrm{Re}}\left(\frac{\partial}{\partial x}(2\nu\frac{\partial}{\partial x})+\frac{\partial}{\partial y}(\nu\frac{\partial}{\partial y})+\frac{\partial}{\partial z}(\nu\frac{\partial}{\partial z})\right)\right]\tilde{u}_i = RHS \qquad (3.7)$$

The coefficient 2 for the diagonal term is due to the fact that the fully implicit scheme is used for it while the Crank-Nicholson scheme is used for non-diagonal viscous terms. To invert the matrix on the left hand side of Equation 3.7, we employ the approximate factorization scheme,

$$\left(1-\frac{\Delta t}{2\,\mathrm{Re}}\frac{\partial}{\partial x}(2\nu\frac{\partial}{\partial x})\right)\left(1-\frac{\Delta t}{2\,\mathrm{Re}}\frac{\partial}{\partial y}(\nu\frac{\partial}{\partial y})\right)\left(1-\frac{\Delta t}{2\,\mathrm{Re}}\frac{\partial}{\partial z}(\nu\frac{\partial}{\partial z})\right)\tilde{u}_i = RHS \qquad (3.8)$$

It is straightforward to prove that the error of the above factorization is of order of $O(\Delta t^3)$, which can be safely used with a second order accurate discretization. The inversion of the left-hand side of Equation (3.8) requires solving only three tridiagonal matrices in 3D and two tridiagonal matrices in 2D. For This special case of a system of linear equations that is tridiagonal, the procedures of LU factorization, forward- and back-substitution each take only O (N) operations, where N is the number of grid points. This is insignificant compared to the solution of the pressure equation. And also naturally, one does not reserve storage for the full N × N matrix, but only for the nonzero components, stored as three vectors. For periodic boundary conditions, the matrix is cyclically tridiagonal, and we use the Sherman-Morrison formula and treat the system as tridiagonal plus a correction (Press et al. 2001). The solution of these systems can still be done in O (N) operations.

3.2 Mixed Front Tracking/IBM Method for Cellular Fluid Mechanics

A blood cell in suspension or hemodynamic shear flows behaves as a complex liquid drop or capsule with the cell membrane separating fluids with different properties (cf. chapter 2). The cell membrane can be treated as fluid interfaces or elastic structure with complex surface rheology and elastic-type surface tension. Computational methods in multiphase flow and fluid-elastic structure interaction studies can be therefore adopted.

Various types of methods have been developed to represent, track or extract the moving interfaces, including the particle methods (Koumoutsakos, 2005), phase-field method (Lowengrub and Truskinovsky 1998), boundary-integral method (Pozrikidis 2001; Hou et al 2001), level set

method (Sethian and Smereka, 2003), volume of fluid method (Scardovelli and Zaleski, 1999), immersed interface method (Hou and Lowengrub, 2003), immersed boundary method (Peskin 2003) and the front tracking method (Tryggvason et al, 2001). These methods are based on different views and characterizations of the interface movements. The Lagrangian representation leads to the particle methods; the Eulerian formulation leads to the level set and the volume of fluid methods, where the signed distance and the volume fractions are used to extract the fluid interface, respectively; while the mixed Eulerian-Lagrangian formulation leads to the immersed boundary and the front tracking methods. Boundary integral methods are boundary-discretization method by solving the integral equation on the boundaries only, and hence are not (immediately) applicable to more general interfacial fluid flows, such as those governed by the viscous Navier–Stokes equations, which are the main interest in current work. The immersed interface method (Lee and Leveque, 2003) instead incorporates part of this force into jump conditions for the pressure, avoiding discrete dipole terms that adversely affect the accuracy near the immersed boundary.

The mixed Eulerian-Lagrangian formulation used in the immersed boundary and front tracking methods, keeps tracking Lagrangian particles initially distributed on the fluid interface while solving fluid equations in the fixed Eulerian Cartesian grid. The principal advantage of mixed formulation is their inherent accuracy and robustness, partly due to the ability to use a large number of Lagrangian particles on the interface. The mathematical formulation of the immersed boundary method can be derived from the principle of least work in the mixed Eulerian and Lagrangian spaces coupled with the Dirac delta function (Peskin 2002). The two-way interaction of the Lagrangian particles and the fluid is via a Dirac delta function in strict mathematical sense and its various smoothed version in numerical computations. The smoothed delta function is applied to both force spread from Lagrangian interface to the fluid (Lagrangian to Eulerian) and the velocity interpolated from the fluid nodes to the Lagrangian particles on the interface (Eulerian to Lagrangian):

1) Spreading the membrane force to the local surrounding fluid as volumetric source terms in the momentum equations to satisfy the dynamic Young-Laplace condition across the interface;
2) Advancing the interface with the locally interpolated fluid velocities to satisfy the no-slip boundary condition between the fluid and the membrane.

The original immersed boundary method was developed by Peskin (1972) for the computation of the fluid structure interaction in the cardiac heart valve motions. The fluid properties were assumed as constants around the structure. In these cases where the tracked interface carries only forces that vanish everywhere except at the interface, the procedure described above is all that needs to be done. However, for blood cell interaction and adhesion, the blood cells have different properties than the blood plasma and are modeled with (compound) liquid capsules with elastic membranes separating fluids with different viscosities (cf. Chapter 2). Therefore it is also necessary to update the fluid properties on the Eulerian grid every time the Lagrangian interface moves across them. The front tracking method developed by Undervi and Tryggvason (1992) proposed a fast global approach to computing the smoothed Heaviside function based the geometric information stored with the Lagrangian-represented interface. Then, the smoothed Heaviside function, called an index function, is used to update the fluid properties,

$$\mu(\mathbf{x}) = \mu_1 + (\mu_2 - \mu_1) I(\mathbf{x}) \tag{3.9}$$

where $I(\mathbf{x})$ is the index function ranging from 0 to 1 smoothly across the interface. The essential elements of the fast global approach for updating the fluid properties are reiterated briefly here (Unverdi and Tryggvasson, 1992):

(1) Compute the gradient of the smoothed index function with finite thickness from the Lagrangian representation of the interface. Let $\mathbf{G}(\mathbf{x})$ be the gradient of the index function

evaluated at a stationary grid points **x**, and D is a smoothed delta function discussed above (see 3.9 or 3.10), then

$$\mathbf{G}(\mathbf{x}) = \sum_l D(\mathbf{x} - \mathbf{x}^{(l)})\mathbf{n}^{(l)}\Delta s^{(l)} \tag{3.10}$$

where $\mathbf{n}^{(l)}$ is the unit normal vector to an interface element $\Delta s^{(l)}$ with its centroid at $\mathbf{x}^{(l)}$. The normal vector is calculated directly from a Legendre polynomial fit through the end points of each elements and the end points of the adjacent elements. The initial interface element size is a quarter of the Eulerian grid size.

(2) Compute the divergence of the smoothed interface gradient $\mathbf{G}(\mathbf{x})$ and solve the identity condition which the smoothed index function must satisfy:

$$\nabla^2 I \equiv \nabla \bullet \mathbf{G} \tag{3.11}$$

The Poisson equation is discretized in the staggered grid and solved by direct inversion the same way as for the pressure Poisson equation (3.6c).

This approach leads to a smoothed Heaviside function $I(\mathbf{x})$ across the interface location with a small- but finite-thickness interface transition layer.

We use a cosine-shaped 'filter' function as an approximation of the delta function for both force distribution from interface Lagrangian particles to Eulerian grids and velocity interpolation from Eulerian grids to interface Lagrangian particles. In one dimension, it takes the form (Peskin 1977; Unverdi and Tryggvason 1992),

$$D(x_i - x^{(l)}) = \begin{cases} \dfrac{1}{4h}\left(1 + \cos\dfrac{\pi}{2h}(x_i - x^{(l)})\right), & \text{if} \quad \left|x_i - x^{(l)}\right| < 2h \\ 0, \quad \text{otherwise} \end{cases} \tag{3.12}$$

where $x^{(l)}$ and x_i donate the coordinate of the center of the smoothed Delta function interval and a point where the function will be evaluated; h is the grid size, implying the smoothed Delta function has a transition zone with thickness of four grids. For multi-dimensions, the smoothed Delta function is the product of the ones in each direction. In the case of two dimensions here, we can write it as following,

$$D(\mathbf{x}_i - \mathbf{x}^{(l)}) = \begin{cases} (4\Delta x)^{-2} \prod_{i=1}^{2} \left(1 + \cos \frac{\pi}{2\Delta x} (x_i - x^{(l)}) \right), & \text{if} \quad \left| \mathbf{x}_i - \mathbf{x}^{(l)} \right| < 2h \\ 0, \quad \text{otherwise} \end{cases} \tag{3.13}$$

Then we can apply the smoothed Delta function for interaction of Lagrangian particles and Eulerian fluid nodes. For force spreading or distribution, it applies the membrane force to the fluid locally surrounding it,

$$\mathbf{F}(\mathbf{x}_i) = \sum_l D(\mathbf{x}_i - \mathbf{x}^{(l)}) \mathbf{f}^{(l)}. \tag{3.14}$$

This force acts as a local source of the volumetric forces on the right hand side of the momentum equations (3.5). At the same time, the velocity is interpolated from the Eulerian grid where the fluid velocities are solved and stored for the Lagrangian particles,

$$\mathbf{u}(\mathbf{x}^{(l)}) = \sum_i D(\mathbf{x}_i - \mathbf{x}^{(l)}) \mathbf{u}_i. \tag{3.15}$$

The interface particles are advected with this locally interpolated velocity to satisfy the no-slip boundary condition,

$$\frac{d\mathbf{x}^{(l)}}{dt} = \mathbf{u}(\mathbf{x}^{(l)}). \tag{3.16}$$

These ordinary differential equations are solved with the second-order Adams-Bashforth integration scheme the same way as the convection terms are handled in the Navier-Stokes equations for consistency.

For compound liquid models for the leukocytes, care is taken to compute the index functions across the nuclear membrane and cytoplasm membrane respectively. Things become easy since we know the viscosity of the fluids in the different layers of the cells, and there are no triple junctions formed among the three fluids. The index function computed from the nuclear membrane is used to update the fluid inside the nucleus only.

$$\mu(\mathbf{x}) = \mu_p + (\mu_c - \mu_p) I_1(\mathbf{x}) \tag{3.17}$$

$$\mu(\mathbf{x}) = \mu_n + (\mu_n - \mu_c) I_2(\mathbf{x}) \tag{3.18}$$

where μ_p, μ_c and μ_n stand for the blood plasma viscosity, cytoplasm viscosity and nucleus viscosity, respectively, and $\mu_n \geq \mu_c \geq \mu_p$. The update of (3.18) applies only inside the cell after the first round of update (3.17).

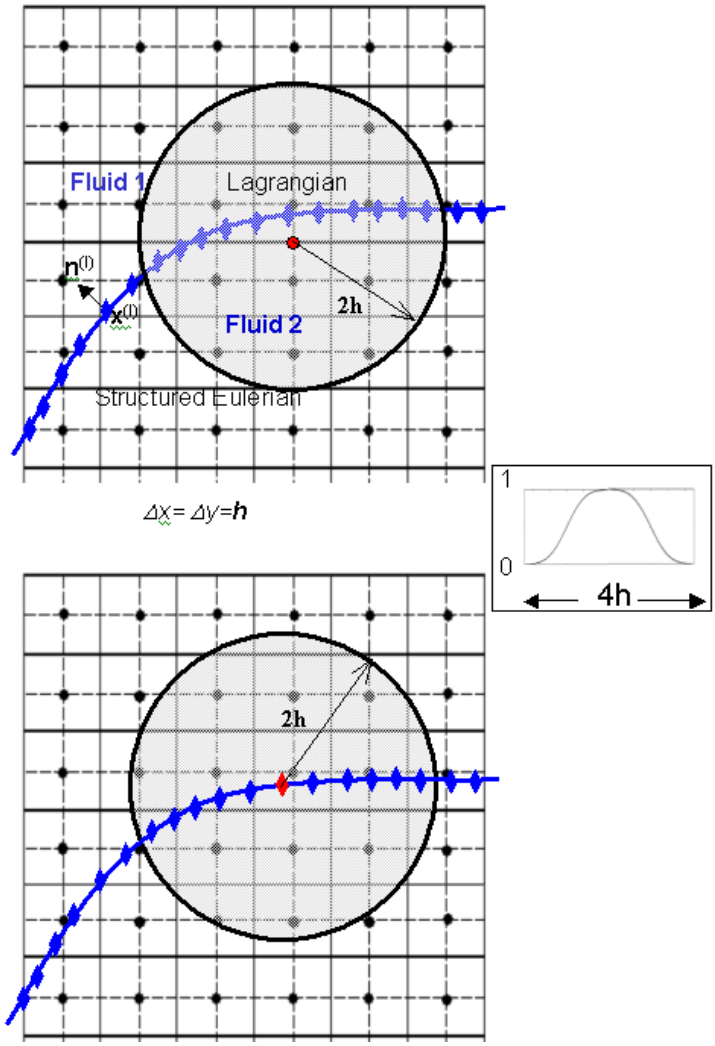

Figure 3.3 (a) Lagrangian particles contributing force to the grid point X are enclosed in the gray circle with the center at the grid point X.; (b) Grid points contribution to the velocity of the Lagrangian particle P are enclosed in the gray circle with the center at the Lagrangian Particle, where h stands for the grid size. Diamond: Lagrangian particles; Circle: Eulerian grid.

3.3 Cell Membrane Discretization

Lagrangian points connected by elements are used to represent the cell membrane. Both the points and their connectivity are stored at each time step. In two dimensions, the points are connected with linear or higher order elements. For each element, data is stored for its connecting points, principal stretch ratios, normal and tangent vectors, surface force and the jump of viscosity. In three dimensions, the membrane is a mathematical surface and represented in the same way but with linear triangular elements.

For elastic membranes, the surface force depends on the local strain unlike a simple fluid interface with constant surface tension. To compute the local strain at each time step, our three-dimensional membrane computation is based on the model developed by Charrier et al. (1989) and applied to red cell modeling in Eggleton and Popel (1998). As discussed above, the displacements of the connecting nodes for an element can be computed from the interpolated fluid velocities to the nodes. The deformed elements do not necessarily remain in the same plane as the original elements in its unstressed state. Hence the deformed element is transformed to the plane of the undeformed element to determine the relative displacement of the nodes, principal stretch ratios (λ_1, λ_2), and the corresponding forces. Given these data and material properties of the membrane, we can compute the surface force on the membrane based on the principal of virtual work. The resultant total force **F** on a specific node is computed from the sum of the forces exerted by all elements connected to the node. The force is spread to the local fluid as a volumetric force source term in the fluid flow momentum equation as discussed in Section 3.2. Quantities on an element are approximated by linear functions in the plane of the element,

$$\phi(x, y) = ax + by + c$$

where the coefficients can be obtained from the local interpolations from the values of the connecting nodes of a triangular element. This can be extended to higher order elements when necessary.

For periodic boundary conditions, the front can move out of the domain on one side and move in through the other side. All that is needed is to correctly identify the grid point that corresponds to a given front position. For periodic fronts, the end point in one period is connected to the first point in the next period, and when computing the length or area of such elements, or when a line or a surface is fitted through the end points, it is necessary to correct for the positions of the points. For bond force computations (discussed below), we give a predefined critical length beyond which the bond is considered broken.

3.4 Ghost Cell Method for Flow in Complex Geometries

Biological fluid dynamics *in vivo* often involves complex geometries and disturbed flow patterns (cf chapter 1, section 1.3). The conventional approach to handling the complex geometry would employ structured or unstructured body-conforming grid. Depending on the computational methods (finite difference, finite volume or finite element), either grid transformation or complex discretization has to be done (Ferziger and Peric, 1999). Besides the nontrivial task of grid generation, these operations can bring significant overheads and deteriorate the performance of many efficient solvers such as the approximate factorization solvers discussed in Section 3.1. Grid transformations would require a highly accurate way of calculating the transformation Jacobian matrices, which can sometimes be quite difficult to achieve. A ghost cell method in a fixed Cartesian grid is implemented and combined with the front tracking method discussed above to compute cellular interaction and adhesion in complex geometries.

The immersed boundary technique has recently been generalized to model the complex *solid* boundaries or walls beyond its original role for immersed elastic structure and fluid interaction in fixed Cartesian grid. It has been demonstrated to require significantly less computation than conventional body-conformal grid methods (Goldstein et al 1993; Saiki and Biringen 1996; Mohd-Yusof, 1997; Fadlun et al 2000; Verzicco et al, 2000; Lai and Peskin 2000; Iaccarino and Verzicco, 2003; Tseng and Ferziger 2003; Mittal and Iaccarino 2005). The idea is to find the *right* source terms in the Navier-Stoke fluid momentum equations or equivalently

develop a local reconstruction of the discretization stencil so that the boundary conditions are satisfied on the immersed walls without altering the Cartesian grid. The main advantages of this method are memory and CPU savings and ease of grid generation compared to body-conformal grid methods.

The feedback forcing idea leads to the virtual boundary method developed in Goldstein et al (1993) and extended in Saiki and Biringen (1996):

$$\mathbf{f}(\mathbf{x}_s,t) = \alpha\int_0^t (\mathbf{u}(\mathbf{x}_s,t) - \mathbf{U}(\mathbf{x}_s,t))dt + \beta(\mathbf{u}(\mathbf{x}_s,t) - \mathbf{U}(\mathbf{x}_s,t)) \qquad (3.19)$$

where $\mathbf{x}_s$ is the coordinate of the immersed boundary, $\mathbf{U}$ is the desired velocity of the boundary in general (zero for the no-slip boundary condition), α and β are the negative tuning constants and most often take very large magnitudes to make the virtual boundary close to the real moving wall or no slip wall boundary conditions. And the elastic stiff-spring method was developed in Lai and Peskin (2000),

$$\mathbf{f}(\mathbf{x}_s,t) = k[\mathbf{x}_s^*(t) - \mathbf{x}_s(t)] \qquad (3.20)$$

where $\mathbf{x}_s(t)$ and $\mathbf{x}_s^*(t)$ are the actual location and location after the elastic deformation of an immersed boundary, respectively, and k is the user-defined elastic spring constant large enough to make the movement of the immersed boundary smaller than some criterion. In both cases, these forces are spread to the local fluid via the smoothed Delta function similarly to the discussion in section 3.2. Therefore these methods enforce an approximate no-slip boundary condition for an immersed body by adding a nearly singular feedback forcing term to the momentum equations. These types for methods have at least two disadvantages:

1) The feedback force terms have flow-dependent parameters;
2) The large constants and nearly singular feedback forces restrict the computational time step significantly.

And the stability of the calculation depends on not only the values of constants but also the exact geometry and flow field (Goldstein et al 1993; Fadlun et al 2000; Lai and Peskin 2000).

Instead, Mohd-Yusof (1997) found a natural way to obtain the *necessary* body-force directly from the momentum equation such that the desired velocity field is obtained at the location of the boundary. Let us move all the spatial derivative and source terms on the right hand side of the momentum equation (3.2) to RHS, and denote the desired and unknown force as f, then

$$\frac{u_i^{n+1} - u_i^n}{\Delta t} = -RHS_i + f_i \tag{3.21}$$

In order to satisfy the specified velocity *U* at the immersed boundary of arbitrary shape, then it reads,

$$f_i = \frac{U_i^{n+1} - u_i^n}{\Delta t} + RHS_i \tag{3.22}$$

This overcomes the issues of the feedback forcing method: No flow-dependent parameters are involved; no extra work is needed to evaluate (3.22); and most importantly, it will not influence the stability of the time stepping scheme. This effectively intrinsic force can be understood from the physical meanings of the different terms in the momentum equations, including inertial force, pressure load, viscous force, and other volume force contributions such as the surface force and receptor-ligand bond force,

$$\mathbf{f}_{inertial} = \frac{\partial \rho \mathbf{u}}{\partial t} + \nabla \bullet (\rho \mathbf{u}\mathbf{u}) \tag{3.23a}$$

$$\mathbf{f}_{pressure} = -\nabla p \tag{3.23b}$$

$$\mathbf{f}_{shear} = \nabla \bullet (2\mu \mathbf{S}) \tag{3.23c}$$

$$\mathbf{f}_{other} = \mathbf{F} \tag{3.23d}$$

where **F** is the force term shown in Eqn. (3.2). These have been shown in Fadlun et al. (2000). Later on, they also showed that, for comparable accuracy, the computational requirements for the

IBM approach are much lower than simulations on an unstructured, boundary-fitted mesh as given in previous published paper (Verzicco et al 2000).

Fadlun et al. (2000 applied momentum forcing within the flow field with a linear interpolation from the streamwise or the transverse direction depending on the flow patterns. We enforce the specified boundary condition on a rigid solid boundary immersed in a fixed Cartesian grid by extrapolating the variable to ghost nodes inside the body and outside the fluid domain of interest. A high-order extrapolation is used to preserve the overall accuracy. The numerical procedure we use is as follows,

1) Define the domain inside and outside of fluid;
2) Identify the ghost cells for each boundary;
3) Reconstruct the local solution around the boundaries to impose the boundary condition explicitly or implicitly;
4) Continue to solve the Navier-Stokes equations with these changes

The immersed body boundaries are represented as connected linear segments. We tag grid nodes according to whether they are inside and outside the body, or on the boundary of the body. The body boundaries are usually not collocated with the grid nodes for the velocities (Figure 3.4). For a fully staggered grid, it is always true since different velocity components are defined at centers of different boundaries of the computational cells. Once the inside nodes are identified, the boundary nodes lying inside the body and connected to at least one computation node in the flow domain are marked as the ghost nodes in the flow computation.

The wall boundary conditions on the immersed body boundaries are enforced with a local reconstruction scheme involving the ghost node and neighboring flow nodes. Quadratic polynomials are used for the interpolations. Higher-order polynomials are more accurate but introduce bounded-ness problems and hence numerical instability. The variable values at the ghost nodes can be updated either in an implicit or an explicit manner. Implicit updating is in general observed to have enhanced numerical stability and enforce the wall boundary conditions more accurately whereas explicit updating of the ghost node values with a direct forcing term

does not change the local pattern of the original system matrix and more straightforward to implement.

The quadratic interpolation polynomials are consistent with the second-order-accurate finite volume Navier-Stokes flow solver that uses quadratic variation of flow variables in the direction normal to the wall. This will retain the formal second order accuracy of the scheme. If the flow variables are assumed to vary in a quadratic manner along the wall normal direction and linearly along the wall, the interpolating polynomial is

:

$$\phi = a_0 + a_1 n + a_2 t + a_3 nt + a_4 n^2 \tag{3.24}$$

where the wall coordinates n and t as shown in Fig. 3.4b. The normal to the wall intersects the adjacent grid lines at two points and the variable values at these two points in turn depend on the neighboring flow node values. Hence the five constants of the assumed polynomial are evaluated from the four neighboring flow nodes, marked with filled-in circles, and the wall point (Figure 3.4). The ghost-node value is either extrapolated or evaluated using the concept of an image point. The use of the image point in case of a quadratic interpolation most often produces better weighting coefficient (Majumdar et al. 2001).

The flow solver usually needs the variable values at the ghost node as weighted combination of the values at the neighboring nodes, in the following form

$$\phi_G = w_1\phi_1 + w_2\phi_2 + w_3\phi_3 + w_4\phi_4 + w_B\phi_B \tag{3.25}$$

It is therefore most convenient to evaluate the relevant weighting coefficients and the neighboring node indices in the assembly or preprocessing stage and re-use them later in the flow solver. The weighting coefficients can always be expressed in terms of the interpolating polynomial in the following form based on Eqn. (3.24) and Eqn. (3.25):

$$[w_1, w_2, w_3, w_4, w_B] = T^{-1}[n^2, nt, n, t, 1] \tag{3.26}$$

where in the case of a quadratic interpolation T is a 5 × 5 matrix, whose elements can be computed from the local normal and tangent vectors of the five boundary points of the interpolation space.

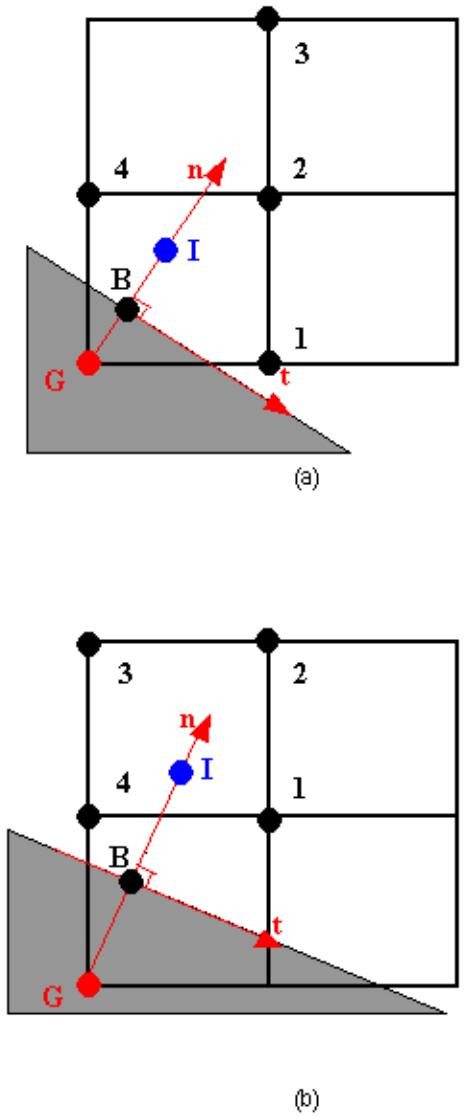

Figure 3.4 Schematic representation of the quadratic interpolation procedure in ghost cell immersed boundary method, where (G Ghost node, I Image node): (a) case 1; (b) case 2. More cases can be included.

There are a few other versions of the immersed boundary methods that have been applied to the flow in complex geometries. Ye et al. (1999) and Udaykumar et al. (2001) have presented a finite-volume Cartesian method by reshaping the immersed boundary cells to fit the

local geometry and using quadratic interpolation to calculate the fluxes across the cell faces while preserving second-order accuracy. This local reshaping the control volume make the implementation difficult and sacrifice the simplicity of the ghost-cell immersed boundary technique.

The codes are implemented for shared-memory parallel computing with the parallel derivatives. We have tested its performance at the E10k Sun machines located at Center for Advanced Information Processing of Rutgers University. The parallel scaling for a typical run in our studies is shown in Figure 3.5, where the CPU times spent on various parts of the code are plotted separately. The Navier-Stokes solver, including the approximate factorization and pressure projection Poisson equations, are most computationally intensive. For a single node or process computation, the Navier-Stokes solver takes about 90% of the total CPU time. For multiple processor parallel computations, the power-law decay of the CPU time for the Navier-Stokes solver as a function of the number of processors is quite satisfactory. The approximate factorization and the direction inversion Poisson solvers have been shown to significantly reduce the total amount of computing time compared with a bicongugate gradient stabilization method or text-book methods, such as successive over-relaxation (SOR) method. The run with SOR would have taken 10 times more CPU time than that of the approximate factorization scheme. This is very important to three dimensional computations where the SOR can take up tens of thousands iterations to converge (Tryggvason et al 2001). And the approximate factorization method is a direct solver which inverts well-behaved diagonal-dominated matrices; hen it is more robust and efficient.

3.5 Cell Adhesion Kinetics and Mechanics

The kinetic equations governing the receptor-ligand bond formation and breakage, Equation 2.19 (repeated below but dropping the superscripts), are solved with fluid equations and the membrane mechanics

$$\frac{\partial N_b}{\partial t} = k_f (N_r - N_b)(N_l - N_b) - k_r N_b$$

with the association and dissociation rates defined by Equation 2.21 and 2.22 respectively as shown below,

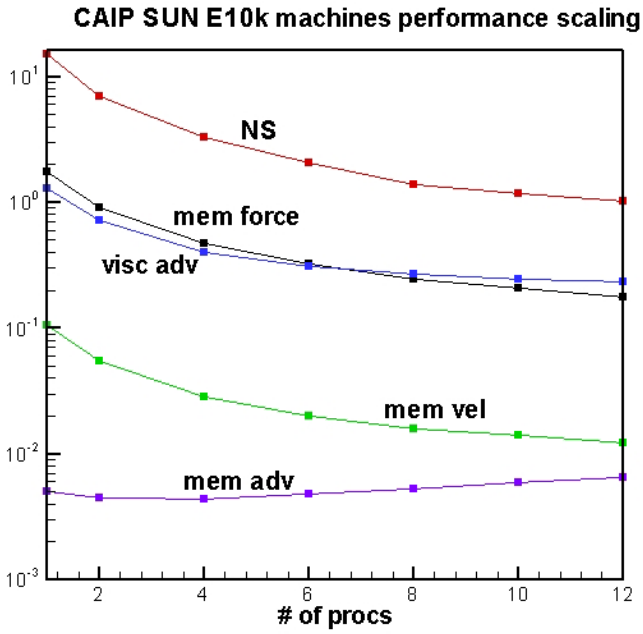

Figure 3.5 Parallel performance scaling as a function of the number processors: “NS” includes CPU time spent on the fluid solver itself (approximate factorization, and pressure Poisson equation); “visc adv” includes CPU time to obtain index function for updating the viscosities; “mem force” includes CPU time on membrane mechanics and receptor-ligand kinetics. (this data came from the benchmarking performed at the CAIP center E10 Sun machines, Rutgers University).

$$k_r = k_{r0} \exp\left(C_r (l - l_0)^2\right)$$
$$k_f = k_{f0} \exp\left(-C_f (l - l_0)^2\right)$$

The second order accurate Runge-Kutta scheme is used for time marching.

After the bond distribution is obtained, we compute the bond force according to the equation below,

$$F_b = n_b \sigma (l - l_0)$$

where l^0 and l are the stress-free and stretched bond separation distances, respectively; σ is the bond spring constant; n_b is the number of bonds per area. This force is included as part of the cell membrane force in Equation 3.14 and spread to the local fluid flow as a volumetric force term in the fluid flow equation. At the same time, as the cells are transported with fluid flow, the locations of the receptors and ligands are updated and used to compute the association and dissociation rates, bond forces in the next time step and so on.

Computational modeling of biological fluid flows is of multiphysical nature. It is important to develop a code that can handle the couplings between different physics. The codes developed are structured accordingly, including the following modules or subroutines: 1) Navier-Stokes solver; 2) front tracking method for multifluid flows; 3) cell membrane mechanics; 4) receptor-ligand chemical reaction kinetics; 5) immersed complex geometries. These are summarized in Figure 3.6. The number of components can increase when more physics are taken into account. The flow chart for the interactions of components is summarized in Figure 3.7.

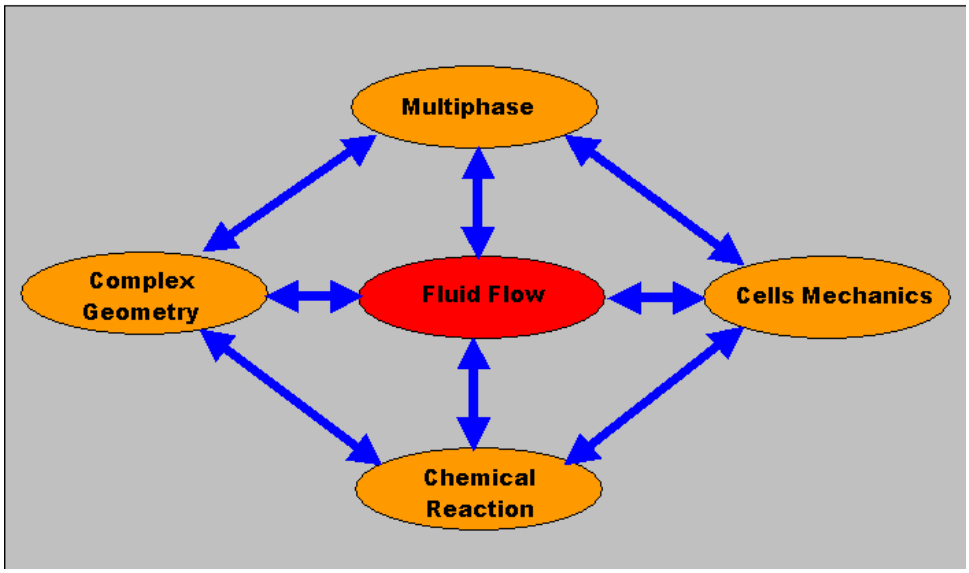

Figure 3.6 Multiphysics modeling in cellular fluid mechanics. Physics studied are shown here but other physics can be readily added when necessary.

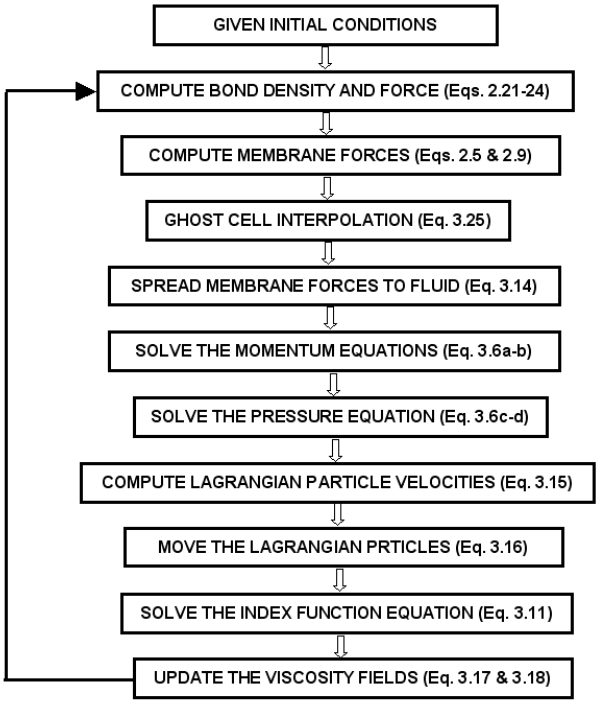

Figure 3.7 Flow chart for computing cell adhesion under shear flow in complex geometries. See sections 3.1-3.5 for more detail.

Chapter 4

Validations and Benchmarks

The computational methods introduced in the previous chapter are applied to a few selected problems to benchmark their performance and accuracy,

1) A two-dimensional flow around a rigid cylinder for the purpose to how capable the computational method can be used to model flow in complex geometries for both steady and unsteady cases (Section 4.1);

2) A three dimensional flow over a model endothelial monolayer are computed to quantify the shear stress and pressure variations along an irregular surface topology which is commonplace in vivo (Section 4.2). The results at small Reynolds number are compared with analytical solutions based on a linear perturbation analysis to Stokes equations (zero Reynolds number);

3) A two dimensional liquid drop under shear flow is benchmarked for the front tracking method developed in Section 4.3;

4) The mass loss issue is examined in Section 4.4 where a three-dimensional drop initially under stretching is computed;

5) A three-dimensional capsule with surface force modeled with an elastic membrane is examined in Section 4.5. And the results are compared with linear analytical solutions.

4.1 Flow Around a Two Dimensional Rigid Cylinder

We validate the performance of the ghost cell immersed boundary method by computing the steady and unsteady flows around a two dimensional rigid cylinder immersed in an otherwise

uniform and unbounded fluid field. This is a classic benchmark problem for computational fluid dynamics, well documented, and extensively studied by experiments and computations with different numerical methods, finite volume and finite element methods with body-conformal curvilinear grids.

The different regimes of flow signatures are determined by the fluid properties, cylinder dimension and free stream velocity, in terms of a single dimensionless Reynolds number $\mathrm{Re}_D = U_\infty D / \nu$, where U_∞ is the uniform free-stream velocity, D is the cylinder diameter, and $\nu = \mu / \rho$ is the kinematic viscosity. The flow starts from the creeping (or Stokes) flow for zero or close to zero Reynolds number. The Stokes flow is symmetric around the cylinder streamwise and span-wise axes.

At small but finite Reynolds number, the flow separates on the cylinder boundary, and two symmetric standing vortices are formed attaching to the downstream sides of the cylinder; the vortices stretches out as the Reynolds number increases. When the Reynolds number is beyond certain critical value, the vortices begin to shed from the cylinder periodically with a frequency determined by the Reynolds number. The array of alternating-sign vortices formed is called the von Karman vortex street. As the Reynolds number further increases, the flow eventually becomes turbulent. These various types of dynamic flow behaviors are challenging to capture even for an unstructured grid solver.

Computations are performed for selected Reynolds numbers (Re_D = 20, 40 and 100), the range of which covers the steady and unsteady laminar flow regimes. The results are compared with established experimental and existing computational results in the literature. The computational domain consists of a large 60D x 30D rectangle with the cylinder located at (15D, 15D). The large domain size is used to reduce the effect of the boundary conditions on the development of the vortex formation and shedding. At the inlet and top and bottom boundaries we specify velocity equal to the free stream velocity and a homogeneous Neumann boundary condition (zero gradients in the outlet normal direction) is applied at the outlet boundary. A

uniform grid, 1800 x 900, is used to discretize the equations. We have performed computations with various grid resolutions to verify the results are mesh-independent.

Figures 4.1a and 4.1b show the streamline (arrow indicating the velocity vector direction) and pressure distribution (background color plots) for Re = 20 and 40, respectively. An inverse pressure gradient is developed on the downstream side of the cylinder boundary, and flow separates from there and forms recirculation zones symmetric about the streamwise cylinder axis. From vortex dynamics point of view, two stretched vortices are formed there as shown in Figure 4.2a for Re_D = 40.

At higher Reynolds number (Re_D ~ 50), the vortices become unstable to perturbations, the symmetry about the cylinder streamwise axis breaks, vortices start to shed from the cylinder periodically and form the von Karman vortex street with alternating-signed vortices. Instantaneous vorticity snapshot is shown in Figure 4.2b for Re_D = 100. We see the von Karman vortex street, indicating the vortex dynamics and symmetry breaking are well captured with our present method. The same grid resolution is applied to this computation.

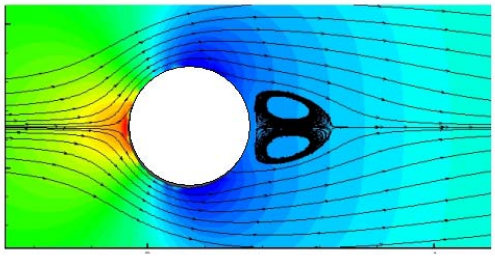

(a)

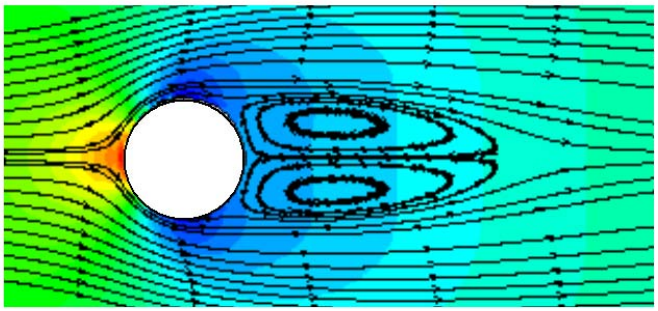

(b)

Figure 4.1 Streamlines and pressure plots of the flow around a cylinder at Reynolds number: (a) Re_D = 20; (b) Re_D =40.

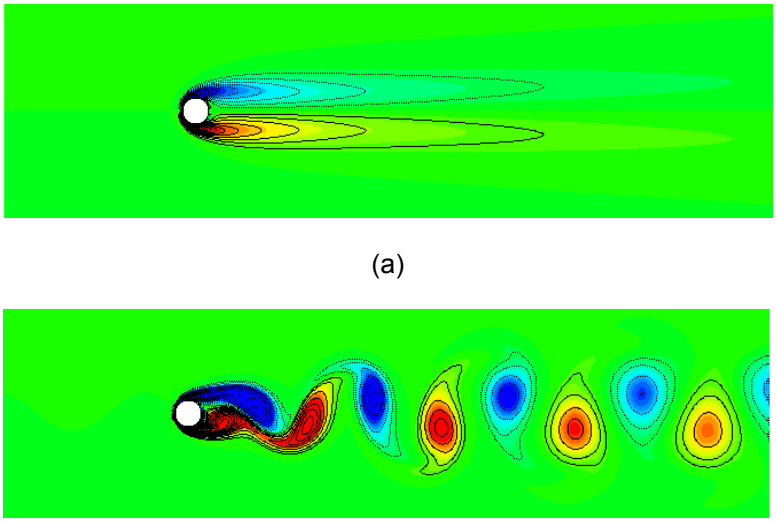

(a)

(b)

Figure 4.2 Vorticity contour and color plots (juxtaposed) for the flow around a cylinder, (a) Re_D = 40; (b) Re_D = 100.

We postprocess and verify the results by computing several key quantities for the steady and unsteady flow around a cylinder discussed above and comparing with well established computational and experimental results, including the recirculation zone length for lower Reynolds number only (Re_D = 20, 40), drag and lift coefficients for lower and higher Reynolds number (Re_D = 20, 40, 100), and Strouhal number which characterizes the frequency of the vortex shedding at higher Reynolds (Re_D = 100). The recirculation length is computed by measuring the distance between the cylinder and the end of the recirculation zone. The drag and lift coefficients are defined as $C_D = F_D/(\rho U_\infty^2/2)$ and $C_L = F_L/(\rho U_\infty^2/2)$ respectively, where F_D and F_D involve integrating the shear stress and pressure load along the immersed cylinder boundaries. The Strouhal number is defined as $St = fD/U_\infty$, where f is the vortex shedding frequency.

Proper interpolation schemes for calculating the pressure, viscous stress and vorticity on the cylinder boundary are critical for their accurate evaluations since the immersed boundaries

are often not collocated with the computational grid nodes. And for fully staggered grid, it is always needed since pressure and velocity components in coordinate direction are defined at computation grid cell centroid and centers of the cell edges respectively. The same quadratic interpolation scheme used to enforce the corresponding boundary conditions (cf. chapter 3.4) on the immersed boundary is adopted here for consistency. The pressure evaluation assumes the pressure Neumann boundary condition (zero gradients in the immersed boundary normal direction) is satisfied on the immersed boundary instead of a Dirichlet boundary as it is for velocity filed. The wall vorticity and shear stress are obtained from location interpolation of the velocity field based on its local reconstruction. Figure 4.3 shows the pressure coefficient along the cylinder surface at Re = 40. Numerical results agree well with body-fitted grid solver (Majumdar et al 2001). The results for both Re_D = 40 and 100 are summarized in Table 4.1 and compared with established experimental measurements and existing computational results. The present drag and lift coefficients agree well with the computational result obtained from a body-fitted mesh, where C_D is the drag coefficient (time-averaged value in case of Re D 100) and C_L is the amplitude of lift-coefficient. Interesting discussion on how to evaluate the force on a solid body in conjunction with the immersed boundary method with stiff spring to model the nearly solid wall can be found in Lai and Peskin (2000); similarly for a method based on direct forcing a variant of immersed boundary technique in Silva et al (2003).

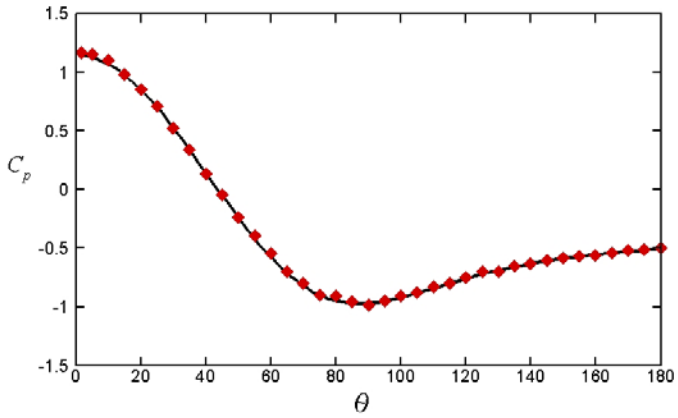

Figure 4.3 Pressure coefficient around the top cylinder (symbol) compared with body-fitted grid result (solid curve) (Majumdar et al 2001)

	Re = 40		Re = 100		
	L_w/D	C_D	St =	C_D(avg)	C_L(rms)
Present	2.23	1.52	0.164	1.41	0.29
Shyy group	2.27	1.52	—	—	—
Lai and Peskin	—	—	0.165	1.4473	0.3200
Dias and	2.69	1.54	0.171	1.395	0.283
Williamson	—	—	0.166	—	—
Roshko	—	—	0.164	—	—

Table 4.1 Comparison of dimensionless recirculation zone length, Strouhal number, drag and lift coefficients with established computational and experimental results.

4.2 Flow Over a Model Endothelial Monolayer Surface

The lumen of the blood vessel is covered with a monolayer of cells, called endothelial cell (EC) or endothelium. The physiologically normal endothelium, with its intercellular tight junctions, functions as a selectively permeable barrier to the passage of macromolecules between blood flow and extravascular tissues. The endothelium has both sensory and executive functions: it can generate molecules that regulate cell adhesion and transmigration across the endothelial junctions which are important in thrombosis and inflammation, also senses and transduces the physical forces into biological signals and responses which are important in vascular tone and remodeling (Davies 1995). Among the important physical forces acting on endothelial cells (ECs) are fluid shear stress and pressure, which have effects on EC morphology. The pressure variations have not been carefully examined before; however we show here that the pressure variation has the same order of magnitude as the wall shear stresses. Cells in the tubular regions of arteries, where blood flows is uniform and laminar, are ellipsoid in shape and aligned in the direction of flow. Cells in regions of arterial branching or high curvature regions, where flow is disturbed, have polygonal shapes and no particular orientation contrasted with a streamlined

endothelial shape in non-disturbed regions. The streamlined endothelial cell morphology minimizes the shear stress applied on it and hence possible damage to it; and at the same time, the junctions become tighter. The polygonal endothelial regions often show increased permeability of the endothelial cell junctions to macromolecules such as low-density lipoprotein (LDL) and are preferential sites for lesion formation in atherosclerosis where the initial deposition of LDL to the extravascular tissue is a prerequisite step.

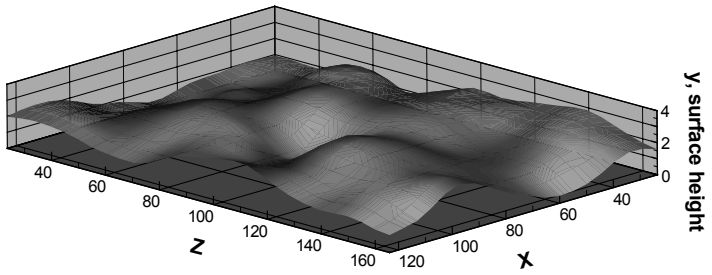

Figure 4.4 In vitro μPIV measurements of the vascular endothelial monolayer height (Courtesy of Voorhees and Wei, Rutgers University, 2004).

The endothelial cell monolayer is a rough surface, whose height has the order of microns. The variations of the shear stress and pressure load on such a wavy endothelial cell monolayer have fundamental impacts on the endothelium mechanics and mechanotransduction. In cell adhesion, shear stress and pressure variations can achieve similar or even higher order magnitudes than the receptor-ligand bond forces and hence strongly perturb the tethering efficiency and rolling stabilization of the blood cell-endothelial adhesion. Hence a detailed flow analysis is needed at least for in vivo cell adhesions. In vitro cell adhesion studies usually make use of a planar glass plate as the substrate, where the surface roughness can be neglected. The detailed shear stress and pressure load distributions are very difficult to obtain in experiments. Micro scale particles can be induced to the flow field and tracked with μPIV (Figure 4.4). But these manually added micro-scale particles could affect the cellular interaction and perturb the receptor-ligand bond formations. Computations can play a significant role here. In this section, we will study the Couette shear flow over a model endothelial wavy surface and compare the result with analytic linear analysis in the Stokes flow limit as the Reynolds number approaches zero.

We model the endothelial cell rough surface with a single-mode sinusoidal surface to a first order approximation as shown in Figure 4.5 (left). Flow field over the surface is governed by the Navier-Stokes equations as shown in Chapter 3. When Reynolds is very small which is typical in microcirculations, we can omit the nonlinear convective terms and solve only the Stokes equations.

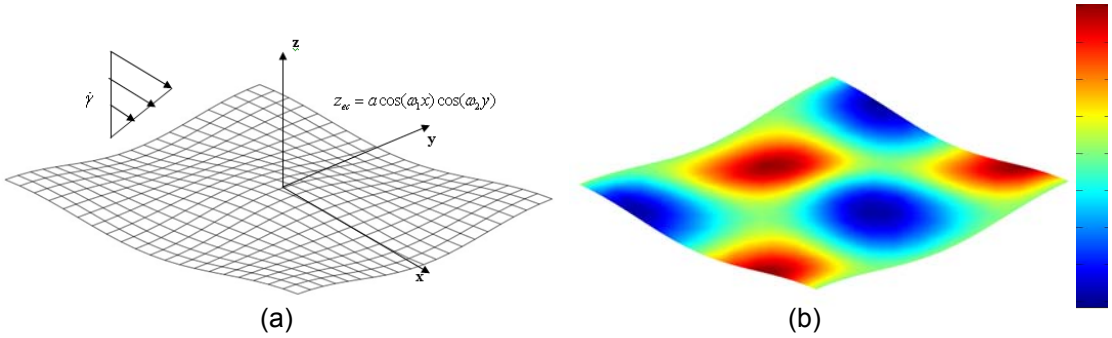

(a) (b)

Figure 4.5 Endothelial cell model surface, periodic in both x and y directions (a); variations on the model endothelial wavy surface (b)

The computational domain includes one full period of a sinusoidal shape in both x and y directions,

$$z_{ec} = a\cos(\omega_1 x)\cos(\omega_2 y) \tag{4.1}$$

where $\omega_1 = 2\pi/\lambda_1, \omega_2 = 2\pi/\lambda_2$; a, λ_1 and λ_2 are the surface amplitude, wavelengths in x and y directions, respectively. To reduce the parameter space, we take $\eta = \lambda_1/\lambda_2 = 1$, and $a = 0.025\lambda_1$ which gives the relative size of the height with the endothelial length.

Periodic boundary conditions are applied on these boundaries accordingly. The upper boundary in z-direction is about 10 times of the sinusoidal variation amplitude or the model endothelium height. A uniform shear velocity is applied on the top boundary. The endothelial cell is treated as non-deformable with the no-slip zero velocity boundary condition applied on the wavy boundary,

$$u = \dot{\gamma} z \qquad top\ \ boundary \qquad (4.2a)$$

$$u = 0, \qquad when\ \ z_{ec} = a\cos(\omega_1 x)\cos(\omega_2 y) \qquad (4.2b)$$

A physiologically typical shear rate $\dot{\gamma} = 800\, s^{-1}$ was applied. The computational grid resolution with 6 grids per amplitude is used. The interpolation scheme used in the previous section applies here to evaluate the pressure and shear stress distribution in postprocessing, and the data is plotted with the help of various visualization tools such as Tecplot. We plot the interpolated surface pressure distribution in Figure 4.5 (right).

Perturbation analysis can be used to derive analytical solutions to the flow over a small amplitude wavy surface (Satcher et al 1992),

$$\tau_{xz} = \left(1 + 2\pi \frac{2+\eta^2}{\sqrt{1+\eta^2}} \frac{a}{\lambda_1} \cos(\omega_1 x)\cos(\omega_2 y) \right) \mu\dot{\gamma} \qquad (4.3a)$$

$$\tau_{yz} = -2\pi \frac{\eta}{\sqrt{1+\eta^2}} \frac{a}{\lambda_1} \sin(\omega_1 x)\cos(\omega_2 y)\mu\dot{\gamma} \qquad (4.3b)$$

$$p = -4\pi \frac{a}{\lambda_1} \sin(\omega_1 x)\sin(\omega_2 y)\mu\dot{\gamma} \qquad (4.3c)$$

where $\eta = \lambda_1 / \lambda_2$, μ is the fluid dynamic viscosity. They are proportional to the given linear shear stress $\mu\dot{\gamma}$. The shear stress in x direction on the boundary includes the unperturbed given linear shear stress plus an in-phase variation induced by the finite amplitude wavy surface; the non-zero lateral (y-direction) stress is proportional to the uniform shear and varies sinusoidally but $\pi / 2$ out of phase in direction with the surface variation; perturbed pressure distribution is $\pi / 2$ out of phase with the surface variation in both direction. This can be shown qualitatively in Figure 4.6 for pressure distribution.

The analytical and computational results are compared in Figure 4.6. Our computations are carried for a finite Reynolds number ~ 0.01, a typical value for microcirculations in cardiovascular system, which explains their difference with the analytical solution for Stokes flow besides the interpolation errors for evaluating the quantities on the immersed boundary which

does not collocate with the computational grid nodes. The same interpolation procedure is applied as that for the flow around a cylinder benchmark.

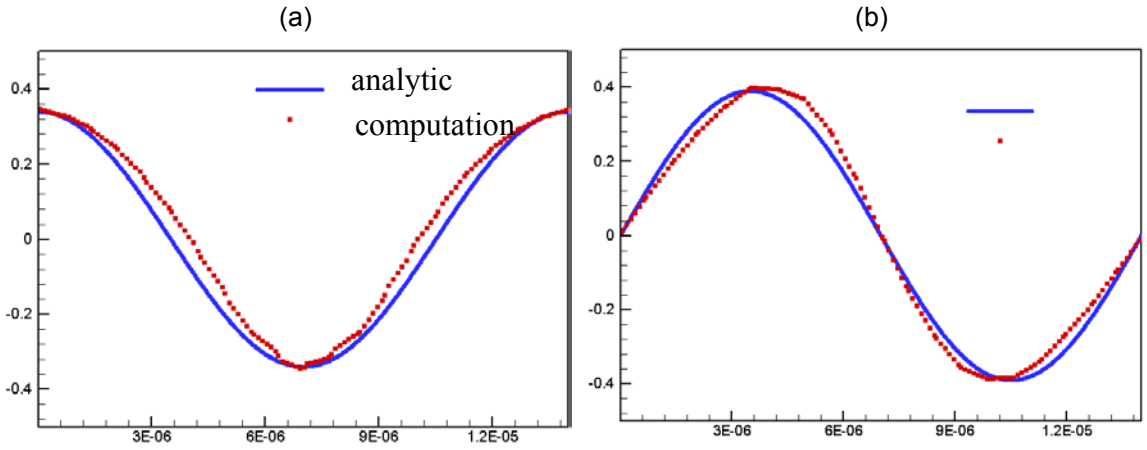

Figure 4.6 (a) shear stress in x component, τ_{xz}; (b) pressure variations. Blue lines are the analytic solutions based on linear perturbation analysis for Stokes flow, and the red squares are the computational values interpolated on the immersed boundaries.

4.3 Droplet Under Shear Flow

Dynamics of deformable objects under hydrodynamic shear flow is critical to rheological behavior of complex fluids, such blood, emulsions, bubbly suspensions, vesicles, to just name a few. From multiphysics modeling point of view, this problem is rather challenging due to the coupling between the structural deformations of the objects and the surrounding hydrodynamic flow (Kanster et al 2005; Kanster et al 2006; Kessler et al, 2007).

The flow of a periodic suspension of two-dimensional viscous drops is a model problem for this type of multiphysics phenomena. In this section, we compute the dynamics of single-filed periodic viscous droplets, with constant surface tension coefficient, driven by the relative motions of two parallel plane walls moving in opposite directions with the same magnitude of velocities (the effects of gravity are neglected). This type of configuration allows people to study the long-time non-equilibrium and equilibrium dynamics of a viscous droplet since the droplet will not move out of a computational domain quickly as in the pressure driven channel flow. The configuration is

sketched in Figure 4.7. The computational is $2\pi \times 2\pi$ (L=H); the droplet radius $a = 1$; the shear rate of initial background Couette flow is defined $\dot{\gamma} = 2U / H$. The top and bottom boundaries are given a velocity U in positive and negative x direction, respectively. The left and right boundaries are periodic. A grid resolution 128 x 128 is used in our computations unless otherwise specified. This model problem is relevant to the study of cell adhesion in vitro since the same boundary conditions can be used to model the parallel plate flow chambers (Chen and Springer 1999).

The dynamic behavior of the droplet is determined by physical properties and size of the droplet, including the surface tension coefficient, viscosity ratio, the droplet size, the wall velocity, and the shear rate as if there is no droplet. With dimensional analysis, we can tell that the flow is determined by the Capillary number $Ca = \mu a \dot{\gamma} / \sigma$, Reynolds number $\mathrm{Re} = a^2 \dot{\gamma} / \mu_1$, and viscosity ratio $\lambda = \mu_2 / \mu_1$.

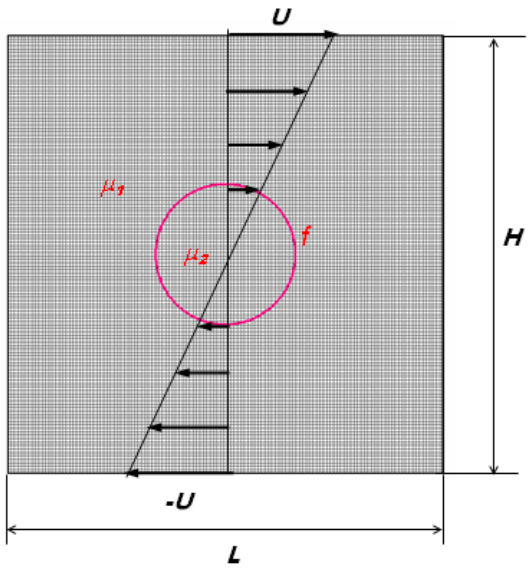

Figure 4.7 Sketch of the computational domain

A droplet with given surface tension subjected to a shear flow can acquire a stationary mean inclination angle with the droplet interface undergoing a tank-treading motion (Zhou and Pozrikidis, 1993). The stationary shape and inclination angle can result from the balance from the

balance of surface tension and shear flow effects: torque associated with the rotational component of a shear velocity field, torque due to its elongation part, and torque resulting from the tank treading motion of the interface. This has been observed in blood cell dynamics when the blood cell is modeled with a droplet with elastic-type membrane (Keller and Skalak 1982).

The results for a run ($\mathrm{Re} = 0.025, Ca = 1$) are shown in Figures 4.8 (a) and (b) for viscosity ratios of 1 and 5, respectively. The final equilibrium shape of the droplet is shown as the curve in red. The streamline plots in Figures 4.8 captured the patterns of the flow past a stationary droplet and rotating flow inside the droplet with the interface which undergoes a tank-treading motion. The equilibrium shapes of the droplets depend on the viscosity ratios. The inclination angle decreases with viscosity ratio and Capillary number.

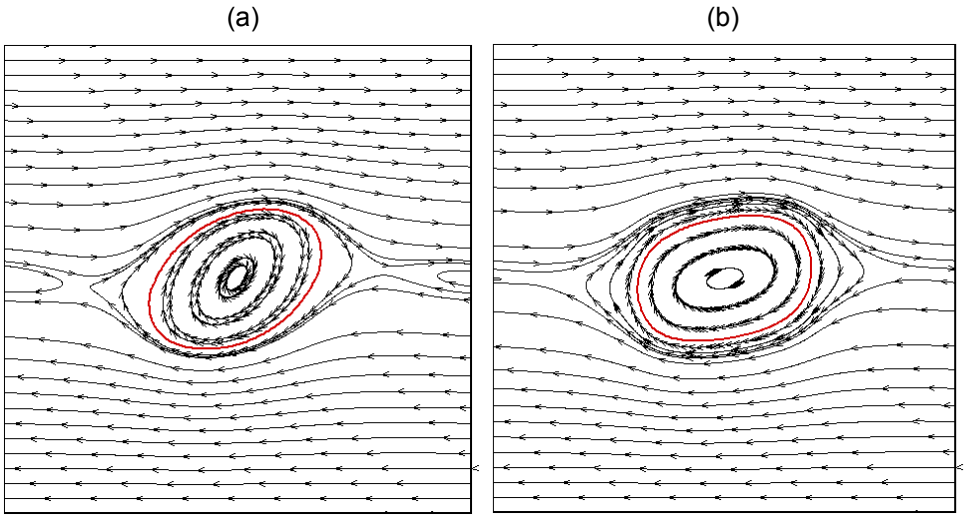

Figure 4.8 Streamline and droplet interface plots for a droplet in linear shear flow (a) viscosity ratio 1; (b) viscosity ratio 5.

We quantify the transient shape deformation and rotating angle of the droplet as sketched in Figure 4.9 as a function of Capillary number. The results are shown in Figure 4.10. The droplets asymptotically reach equilibrium states in both cases run for $(\mathrm{Re} = 0.025, Ca = 1, \lambda = 1)$ and $(\mathrm{Re} = 0.025, Ca = 2, \lambda = 1)$. The time to reach the equilibrium state increases with the Capillary number. And the drop takes more tilted elliptical shapes as the Capillary number increases. These results are quite consistent with the boundary integral

computations of the same model but in the limit of Stokes flow ($\mathrm{Re} = 0$) reported in Zhou and Pozrikidis (1993).

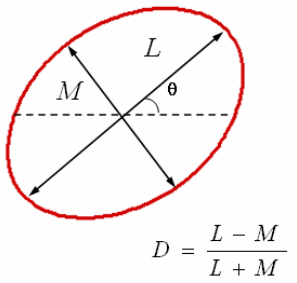

Figure 4.9 Definitions of droplet deformation parameter D and orientation angle θ.

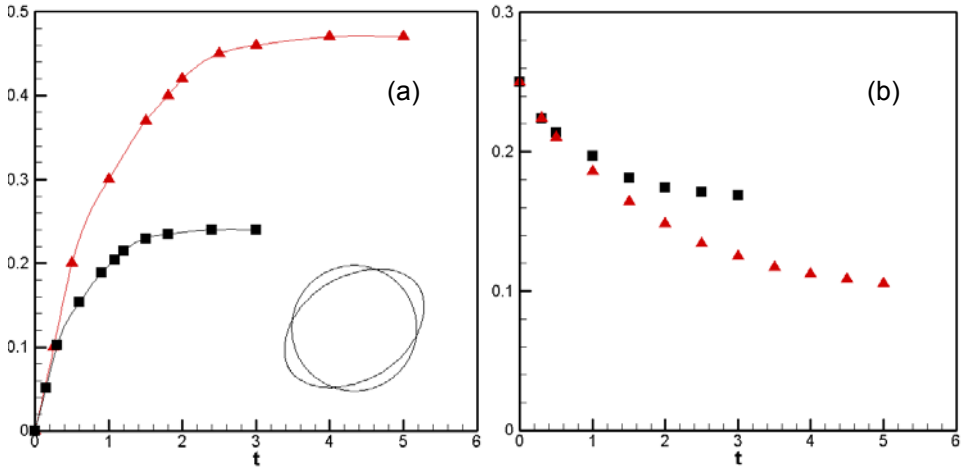

Figure 4.10 (a) Deformation parameter, D as a function of time; (b) droplet angle $\theta^* = 4\theta/\pi$ as a function of time. Red triangles for the case when $\mathrm{Re} = 0.025, Ca = 2, \lambda = 1$; Black rectangles for $\mathrm{Re} = 0.025, Ca = 1, \lambda = 1$.

4.4 3D Oscillating Droplets: Mass and Volume Conservations

A non-spherical liquid droplet with surface force in otherwise stationary ambient fluid can oscillate before it reaches its equilibrium spherical shape finally. In this section, we study an initially ellipsoidal droplet that starts to oscillate because of the large surface force. The droplet's size corresponds to a typical size of the leukocyte roughly 10 μm. From the results you can study the frequency and damping of the droplet's oscillations. Figure 4.11 shows the initial shape of the

droplet, the ratio of the longest axis to the shortest axis is 1.4. The volume (and mass) conservation inside the droplet for an intermediate time computation will be examined.

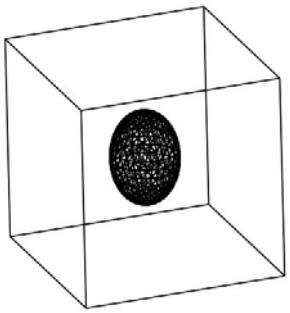

Figure 4.11 The initial shape of the droplets the aspect ratio is 1.4, the kinematic viscosity ratio is about 500, and the surface tension is about 1.8 N/m. No slip boundary condition is used all side boundaries.

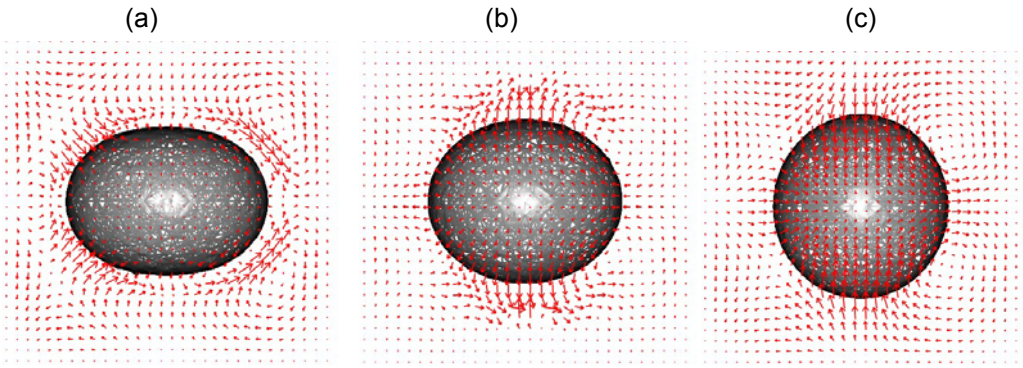

Figure 4.12 Velocity field and the droplet shape: (a) 1e-6 second; (b) 5e-6 second; (c) 1e-5 second.

Figure 4.13 shows the ratio between the two semi-axes of the ellipse as a function of time. You can see that the time scale is very small; the period of the oscillations is about $2 \cdot 10^{-6}$ second.

A critical issue for the interface methods (including front tracking, level set, and volume of fluid) is the mass/volume conservation and the parasite flow. The fundamental reason for that is the approximate implementation of the true physical boundary conditions across the interface with the finite smearing and source terms in the corresponding equations solved in a fixed computational grid. The mass loss and/or spurious current can happen. The former can make a

long time simulation worthless and the later can lead to numerical instabilities especially when the fluid property ratios are high.

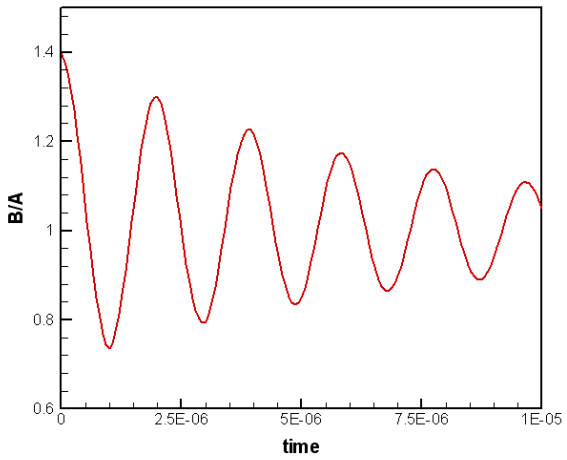

Figure 4.13 Ratio of the elliptic axes as a function of time

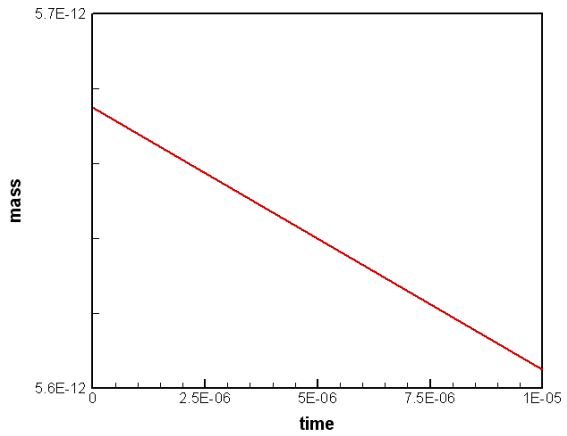

Figure 4.14 Total mass of the droplet as a function of time

We examine the mass conservation. The total volume of the droplet is defined as,

$$M(t) = \int_{\Omega} \rho I(x, y, z, t) dx dy dz \tag{4.4}$$

where I is the index function from the front tracking method (cf. Chapter 3). Because there is no flow across the boundary interface, the volume of the droplet should be conserved. To check the conservation, Figure 4-14 plots the values of volumes as a function of time. The mass loss is less than 1% for this computation to intermediate times. The global computation of the index function

in the front tracking method can have overshoot and undershoot outside the range from 0 to 1. These oscillations often happen at locations close to the interface. We can manually set up cutoffs to cure the overshooting. This aspect is very important in long-time computations where the volume (and mass) loss becomes critical to maintain. We have also tried the local reconstruction of the discretization stencil as pointed out in Popinet and Zaleski (1999) for pressure correction, which conserves mass/volume slightly better. The idea behind this is to take advantage of the fact that the pressure satisfies the Young-Laplace relationship and hence has a jump across the interface. So the regular central difference of the pressure gradient can be corrected accordingly.

4.5 3D Capsule Under Shear Flow

To benchmark the elastic force calculation on the cell membrane, we compute the deformation of 3D capsule, a droplet enclosed with an elastic structure instead of a fluid interface. We repeat the computations in Eggleton and Popel (1998) and compared the results with the boundary integral results as they did. The computational domain is quite similar to what has been sketched in Figure 4.7, but in three dimensions instead. The neo-Hookean membrane model is used in current computations and the grid resolution is 64x64x64. There is no viscosity contrast inside and outside the capsule. The deformation parameter is defined the same way as shown in Figure 4.10.

Two cases are selected for G = 0.1 and G =0.2 where $G = \mu\dot{\gamma}a / Eh$. The time evolution of the deformation parameter is shown in Figure 4.15 (time is normalized with the shear rate). We compare the evolution of the capsule shape using the immersed boundary method coupled with the quadratic form of the strain energy function with that found by Pozrikidis (1995) using the boundary element method using the boundary integral method. They agree pretty well.

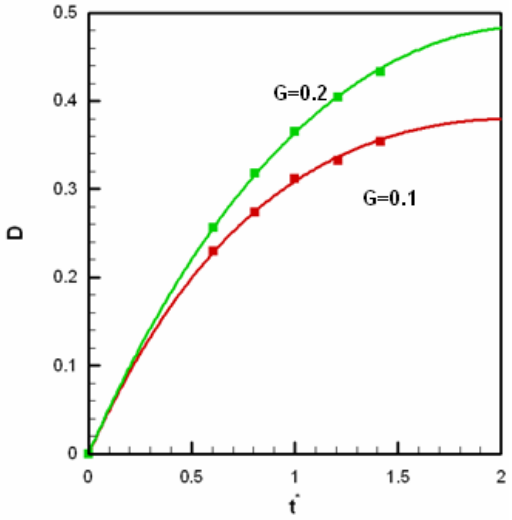

Figure 4.15 Capsule deformation parameter as a function of time (curves: current computational results; symbols: boundary integral results).

Chapter 5

Leukocyte Interactions in Wavy Channels

The endothelial cell layer lining the blood vessel lumens i*n vivo* has irregular topology in contrast with planar microchannels *in vitro* (cf. Figure 1.4, Chapter 1). It is most salient for the bulged endothelial cells in high endothelial postcapillary venules (HEVs), where most of lymphocyte adhesion and transmigration occur (Girard and Springer, 1995). The viscous shear stress and pressure vary along the height of the endothelial cell layer (Satcher et al 1992). The modeling of cellular interaction in complex geometries lacks in current literature. In this chapter, we study the cell hydrodynamic motion, kinetic adhesion, and cellular interactions in wavy geometries, including: leukocyte motions in a model wavy channel (Section 5.1); leukocyte adhesion on a wavy model endothelial cell layer (Section 5.2); and leukocyte-Leukocyte interaction and adhesion in wavy fluid channel (Section 5.3). The leukocyte is modeled as a compound liquid capsule enclosed with elastic membranes. The capsule interior is more viscous than that outside.

5.1 A Single Leukocyte in a Model Wavy 3D Channel

The hydrodynamic motion of a single leukocyte through a flat and wavy blood vessel is studied in this section. The flat vessel has a radius of 10 μm while the wavy vessel has an average radius of 10 μm with the amplitude of the wavy vessel height equal to 3.5 μm (Springer 1995; Davies 1995; Barbee 2002). The leukocyte modeled with a compound capsule has radius of the vessel radius 5 μm. The boundary conditions on immersed boundaries are enforced with the ghost cell method (cf. Chapter 3). The grid resolution is 32 grids per the average vessel radius. The inlet boundary

condition is a parabolic velocity profile with average velocity of 100 μm/sec. We compare the leukocyte trajectory and deformation for a flat vessel and a wavy vessel. The wavy topology was considered for a single red blood cells motion in axisymmetric wavy vessel of microcirculations (Secomb et al 2003). However, the leukocyte motion in a wavy channel lacks at current stage to the author's knowledge.

The results for a flat blood vessel and a wavy blood vessel are shown in Figure 5.1 and Figure 5.2, respectively. The initial position of the leukocyte relative to the valley of wavy surface is examined by putting the leukocyte with a half wavelength shift. The results for this case are summarized in Figure 5.3. In a flat blood vessel, the leukocyte undergoes negligible deformation, while the leukocyte undergoes intermediate to large deformation in a wavy vessel. The trajectories of the leukocytes are plotted in Figure 5.4. Significant differences in both streamwise and spanwise coordinates of the leukocyte mass centers (computed relative to the central axis of the vessel) can be observed. The streamwise coordinate indicates the displacement of the leukocyte while the spanwise coordinate tells how much the leukocyte deforms.

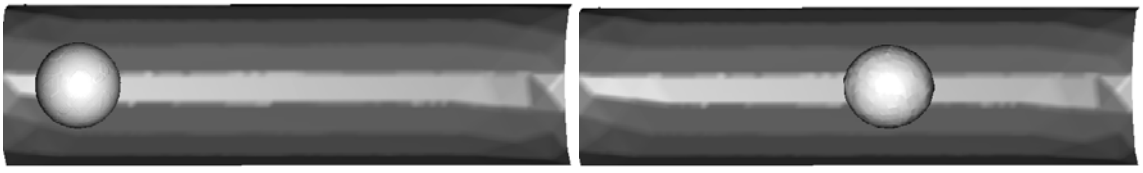

(a) (b)

Figure 5.1 Leukocyte motion along the axis of a flat blood vessel: (a) t = 0; (b) t = 0.3 (sec).

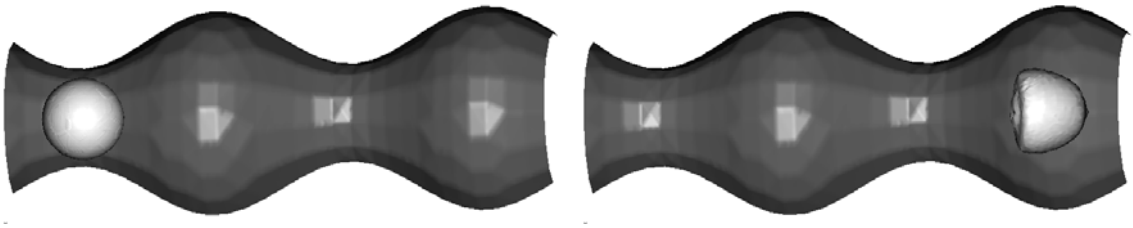

(a) (b)

Figure 5.2 Leukocyte motion along the axis of a wavy blood vessel: (a) t = 0; (b) t = 0.3 (sec).

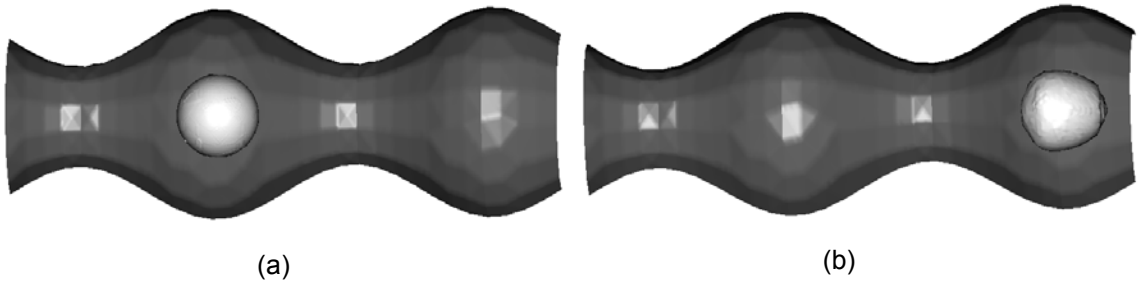

(a) (b)

Figure 5.3 Leukocyte motion along the axis of a wavy blood vessel where the leukocyte starts from the surface valley. (a) t = 0; (b) t = 0.2 (sec).

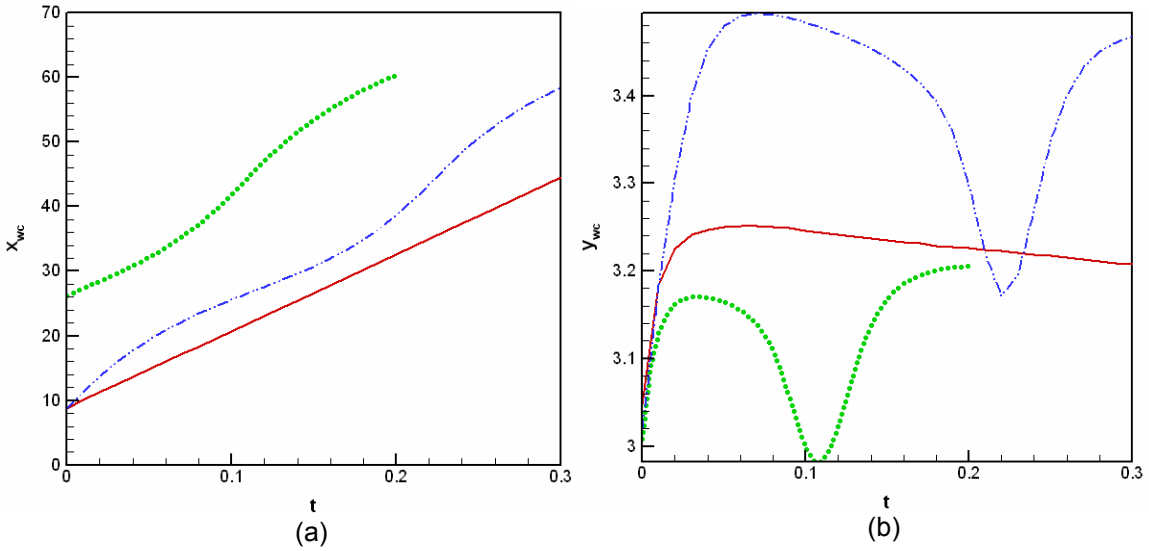

Figure 5.4, (a) the x coordinate (streamwise) of the leukocyte mass center; (b) the y coordinate or effective radius in spanwise direction (radial direction) of the leukocyte. Red/solid, blue/dash-dotted, and green/dotted lines corresponds to Figures 5.1, 5.2 and 5.3 respectively.

The displacement of the leukocyte oscillates with the surface amplitude change of the wavy vessel. The leukocyte moves faster in narrower regions and slower in broader regions. With a fixed inlet velocity the leukocyte moves faster in the wavy channel Figure 5.4(a). The leukocyte is elongated in streamwise direction when leukocyte squeezes through the wave vessel; and relaxed back when it enters into the expansion region. This behavior of leukocyte motion in a wavy vessel can play a role in rheology and resistance of the microcirculations.

5.2 Leukocyte Adhesion on a 2D Wavy Endothelial Cell Layer

The leukocyte collides and adheres with the bulged part of the high endothelial cells in high endothelial venules. The leukocyte adhesion on a 2D dimensional wavy endothelial cell layer is modeled in this section. The leukocyte is modeled with a compound capsule with more viscous cytoplasm and nucleus (see Tables 5.1-3 for lists of parameters). The periodic boundary conditions are applied on the left and right boundaries with a given pressure gradient.

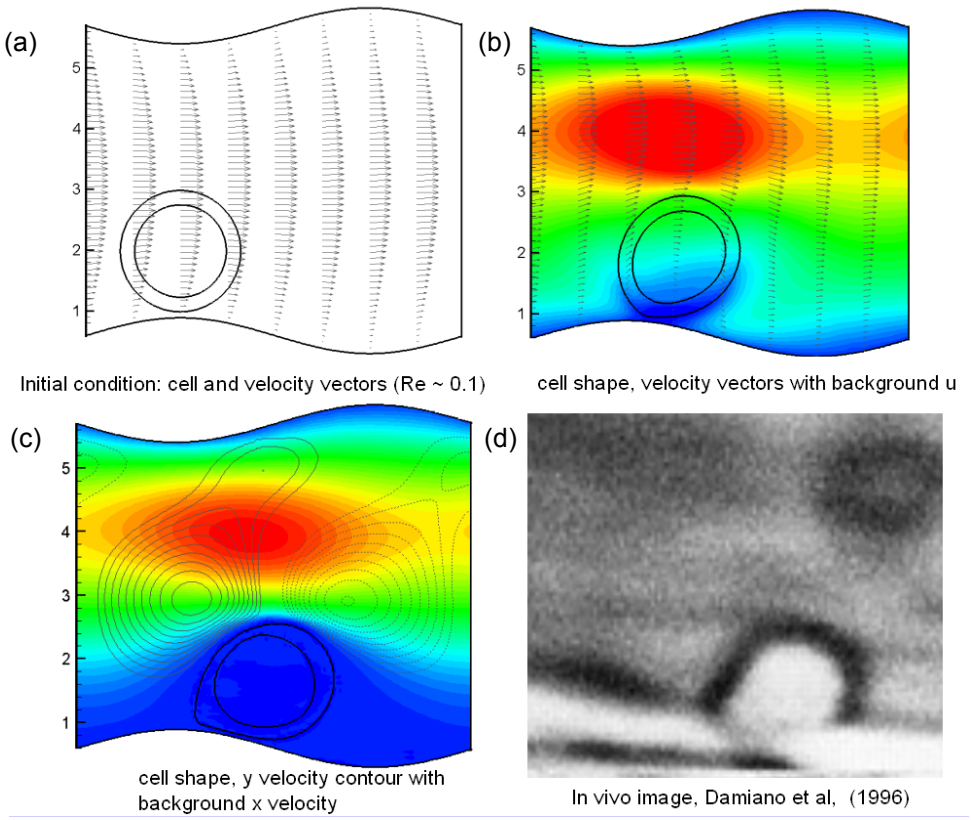

Figure 5.5 Leukocyte adhesion over a 2D model wavy endothelial cell layer: (a) initial cell shape and location with velocity arrow plots; (b) snapshot of the leukocyte, velocity arrow and x-velocity plots; (c) snapshot of the leukocyte, y-velocity contour and x-velocity plots;(d) In vivo leukocyte imaging from Diamino et al. (1996).

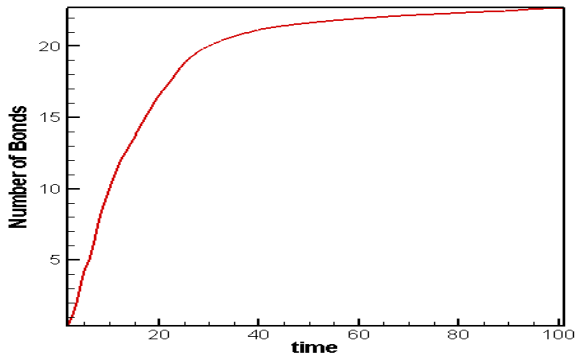

Figure 5.6 Leukocyte-endothelial receptor-ligand bond number as a function of normalized time

The results are summarized in Figures 5.5 and 5.6. The well-known tear-like shape of the leukocyte is observed and juxtaposed with the in vivo image from Damino et al (1996). In Figure 5.5(b), the existence of the more viscous compound capsule significantly changes the flow field in the vessel. The velocity is larger in regions above the leukocyte; and the leukocyte sustains larger shear and torque. The receptor-ligand bonds form between the leukocyte and the wavy endothelial cell layer and the bond number is plotted as a function of normalized time in Figure 5.6. The resistance increases as a result of the leukocyte adhesion and this is important to understanding the rheology of microcirculations.

5.3 Leukocyte-Leukocyte Interaction on a 2D Wavy Endothelial Cell Layer

Leukocyte-leukocyte interaction and adhesion have been shown to be important in secondary leukocyte adhesion (Alon et al 1996; Cocklet and Goldsmith 1997; Eriksson et al 2001; Kadash et al 2004; King and Hammer 2005). These are modeled in this section. Two leukocytes are introduced over a 2D wavy endothelial cell layer. The separation distances between the two leukocytes are half radius and one leukocyte radius in y and x directions, respectively. The configuration is close to that in Kadash et al (2004). Three cases are modeled: no adhesion at all (case I); leukocyte-endothelial adhesion activated but no adhesion between leukocytes themselves (case II); leukocyte-leukocyte and leukocyte-endothelial adhesions (case III). The

case III shows the importance of secondary leukocyte recruitment and leukocyte string formation (Alon et al 1996).

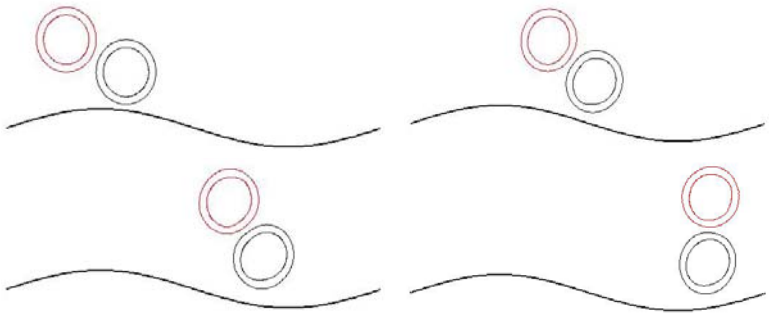

Figure 5.7 Snapshots of leukocyte-leukocyte interaction over a 2D model wavy endothelial cell layer; no kinetic adhesion either between leukocyte and endothelium or between leukocytes

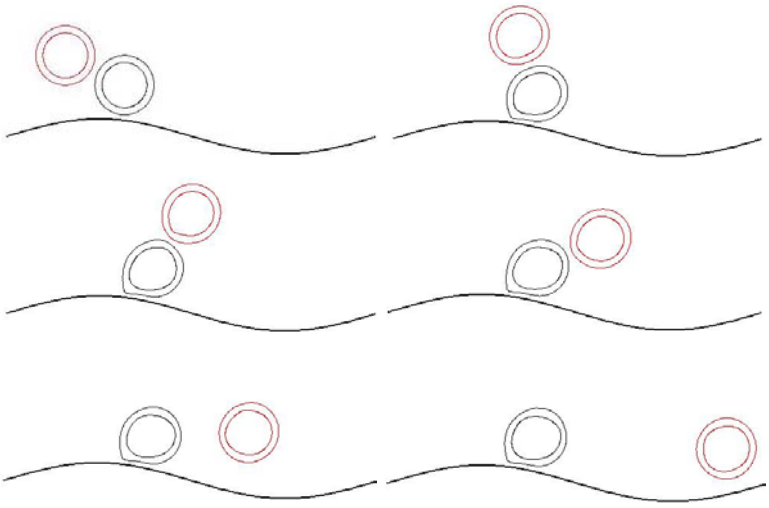

Figure 5.8 Leukocyte-leukocyte interaction and leukocyte-endothelial adhesion over a 2D model wavy endothelial cell layer

Snapshots for the runs of cases I and II are shown in Figures 5.7 and 5.8, respectively. When there is no adhesion at all, the two leukocytes stay together with the top leukocyte pushes the bottom leukocyte towards to the endothelium. This can be shown in Figure 5.9 where the y-

coordinates of the mass center of the bottom leukocyte are compared when with the top leukocyte and without the top leukocyte (a separate run). The bottom leukocyte is significantly pushed towards the endothelial cell layer, or in another word, the existence of the top leukocyte enhances the margination of the bottom leukocyte when they enter the expansion due to the endothelial cell height decrease.

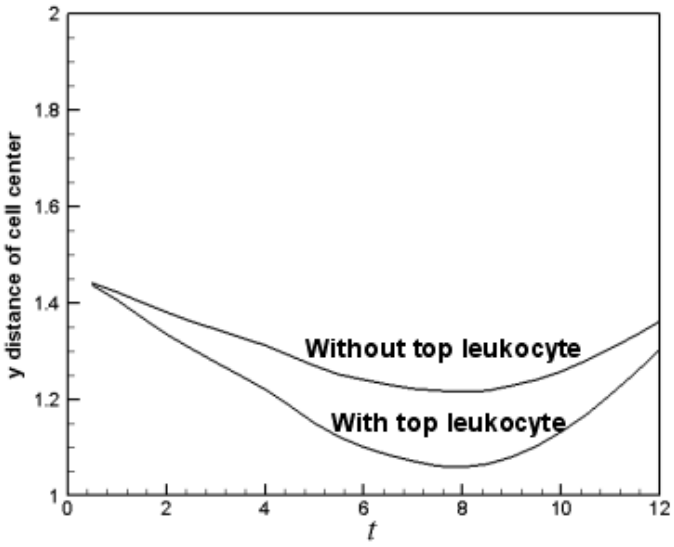

Figure 5.9 The y-coordinates of the bottom leukocyte mass center without and with the top leukocyte (case I).

When the leukocyte-endothelial adhesion activates, the bottom leukocyte adheres to the endothelial cell and slows down significantly. At the same time, the trajectory of the top leukocyte is changed and it also moves much slower. This is shown in Figure 5.10 where the x-coordinates of the bottom leukocyte mass center are plotted as a function of time for cases I and II. This behavior can be relevant to significant resistance increases when leukocyte adheres to endothelium (House and Lipowsky, 1987;Helmke et al. 1997). Please note, the periodic boundary condition is applied and therefore the physical context here are periodic adherent leukocytes.

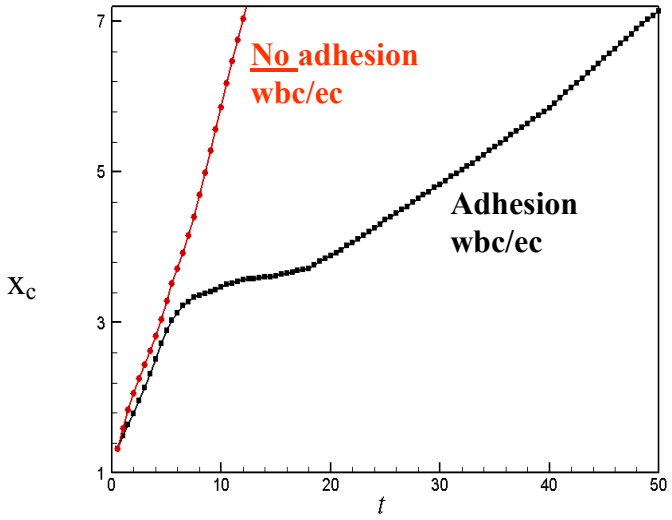

Figure 5.10 Leukocyte trajectories corresponding to Figures 5.7 and 5.8, respectively. The Red line has no leukocyte-endothelial adhesion and the black curve has adhesion between the leukocyte and endothelium.

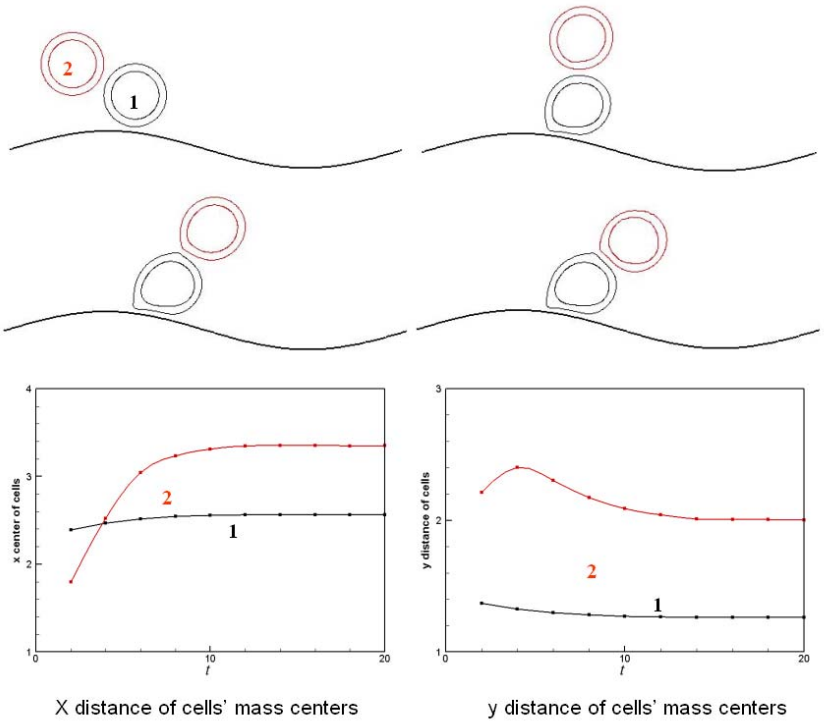

Figure 5.11 Leukocyte-leukocyte interaction, leukocyte-leukocyte adhesion, and leukocyte-endothelial adhesion to a 2D model wavy endothelial cell layer.

The results for case III are summarized in Figure 5.11 where both leukocyte-endothelial and leukocyte-leukocyte adhesions are included. The same adhesion kinetic models are used for both types of adhesions. The bottom leukocyte adheres to the endothelium and the top leukocyte adheres to the bottom leukocyte. When the adhesion between the leukocytes is strong enough, a leukocyte “string” is formed. Otherwise, the top leukocyte can break and detach from the bottom leukocyte. But the adhesion between the leukocytes bring the top leukocyte much closer to the endothelium.

Tube width (D)	8π (μm)
Cell radius (a)	4 (μm)
Plasma viscosity (μ_p)	0.01 dyne-s/cm^2 (1cP)
Cytoplasm viscosity (μ_c)	1 dyne-s/cm^2
Nucleus viscosity (μ_n)	100 dyne-s/cm^2
Plasma density (ρ_p)	1.0 g/cm^3
Cytoplasm density (ρ_c)	1.0 g/cm^3
Nucleus density (ρ_n)	1.0 g/cm^3
Cytoplasm membrane persistent tension	0.12 dyne/cm
Cytoplasm membrane shear modulus	0.14 dyne/cm
Cytoplasm membrane volume modulus	0.01 dyne/cm
Nucleus membrane persistent tension	0.04 dyne/cm
Nucleus membrane shear modulus	N/A
Nucleus membrane volume modulus	2 dyne/cm
WBC surface receptor density	2.0×10^{10} (1/cm^2)
EC surface ligand density	3.75×10^{10} (1/cm^2)
Forward reaction rate constant	1.0×10^{-9} (cm^2/s)
Reverse reaction rate constant	10.0 (1/s)
Unstressed bond length	50.0 (nm)
Static bond elastic constant	0.5 (dyne/cm)
Transient-state bond elastic constant	0.48 (dyne/cm)
$k_B T$	$4.5 \times 10^{-14} erg$ (i.e. $dyn - cm$), $at\ 37^o C$

Table 5.1 Dimensional parameters for leukocyte and adhesion kinetics

Dimensionless parameter	Value	Physical meaning
$\mathrm{Re} = \rho \dot{\gamma} a^2 / \mu_p$	0.0016	Reynolds number
$E_{c,a}^{*} = E_{c,a} / \mu_p \dot{\gamma} a$	25	Cytoplasmic membrane area dilation modulus
$E_{c,s}^{*} = E_{c,s} / \mu_p \dot{\gamma} a$	350	Cytoplasmic membrane shear extension modulus
$E_{n,a}^{*} = E_{n,a} / \mu_p \dot{\gamma} a$	5,000	Nucleus membrane area dilation modulus
$E_{n,s}^{*} = E_{n,s} / \mu_p \dot{\gamma} a$	0	Nucleus membrane shear extension modulus
$f_{E,0}^{*} = f_{E,0} / \mu_p \dot{\gamma} a$	300	Cytoplasm membrane persistent tension
$f_{nE,0}^{*} = f_{nE,0} / \mu_p \dot{\gamma} a$	100	Nucleus membrane persistent tension
$\alpha = \mu_c / \mu_p$	100	Cytoplasm/plasma viscosity ratio
$\beta = \mu_n / \mu_p$	1,000	Nucleus/plasma viscosity ratio

Table 5.2 Macroscopic dimensionless parameters for fluid flow and cell mechanics

Dimensionless parameter	Value	Physical meaning
$C_r = a^2(\sigma - \sigma_{ts})/2k_BT$	3.765×10^4	Coefficient used in reverse reaction rate
$C_f = a^2\sigma_{ts}/2k_BT$	9.04×10^5	Coefficient used in reverse reaction rate
$k_{r0}^* = k_{r0}/\dot{\gamma}$	0.1	Reverse reaction rate
$k_{f0}^* = k_{f0}/a^2\dot{\gamma}$	6.25×10^{-5}	Forward reaction rate
$\sigma^* = \sigma/\mu_p\dot{\gamma}a$	125	Bond elastic constant
$\sigma_{ts}^* = \sigma_{ts}/\mu_p\dot{\gamma}a$	120	Transient-state bond elastic constant
$N_r^* = N_r a^2$	3200	Cell surface receptor density
$N_l^* = N_l a^2$	6000	Substrate ligand density

Table 5.3 Microscopic dimensionless parameters for cell adhesion model

Chapter 6

Cellular Interaction

Through a Model Postcapillary Junction

In the multistep leukocyte adhesion cascade, the leukocytes, circulating in the blood flow abounded with erythrocytes, have to come close enough to the blood vascular wall so that receptor-ligand bonds can form before it gets tethered and rolling along the endothelial cell monolayer lining the blood vessel lumen. The effective length of the receptor-ligand complex is typically less than 1 μm. There are several possible biophysical mechanisms for this leukocyte margination process, including the particulate nature or rheology of the blood flow involving cellular interactions (including erythrocyte-leukocyte interaction and leukocyte-leukocyte interaction), vascular network geometry, irregular topology of the endothelial cell monolayer (particularly for the high endothelial cells in postcapillary venules), and local flow patterns. In this chapter, we investigate these contributing factors. We, for the first time, examine the cellular interactions through a capillary-postcapillary junction bifurcation instead of an ideal planar flow channel or a channel with abrupt and nonrealistic expansion. Our results suggest hematocrit, cellular interactions, and vascular geometry are critical factors that determine the margination and initiation of rolling in postcapillary venules.

Various *in vitro* flow chamber systems have been implemented to simulate *in vivo* leukocyte adhesion and rolling conditions by flowing cell suspensions past surfaces coated with endothelial cells or adhesion molecules (Lawrence and Springer, 1991; Usami et al., 1993; von Andrian et al., 1996; Alon et al 1997; Chen and Springer 1999; Yago et al 2002). These experiments are usually performed with cells suspended in saline or cell culture medium and are

designed to study the effects of shear stress on adhesion between the adhering cells and the surface. However, *in vivo* blood rheology may not be accurately reproduced by these Newtonian solutions due to the particulate nature of blood. Red blood cells (RBCs) not only alter the viscosity of the fluid but also change the spatial distribution and dispersion of leukocytes and other particles in the flow stream, displacing them from the bulk flow toward the blood vascular wall. The rheology of blood is consequently of central importance in lymphocyte-endothelial cell interactions (Goldsmith, 1971; Schmid-Schoenbein et al., 1975; Fung 1993).

This apparent difference between *in vivo* and *in vitro* experiments underscores the importance of hydrodynamic interactions between leukocytes and erythrocytes in postcapillary venules, which have been shown to be the principal mechanism of leukocyte margination at high shear (Schmid-Schonbein et al 1980; Melder et al 1995; Stein et al 1999; Melder et al 2000; Nash et al 2003). As shear stresses increase, the duration of contacts with the endothelium will be shortened, leading to a reduced likelihood of tether formation. However, at the same time collisions with RBCs are likely to become more frequent and more forceful, thus allowing more enhanced exposure of cell body receptors. These two opposing mechanisms may cancel each other out, resulting in an overall automatic braking system for leukocyte adhesion and stable rolling over a wide range of shear stresses (van der Merwe 1999; Chen and Springer, 1999; Lei and Dong 2000; Yago et al 2002).

In most of in vitro leukocyte adhesion studies whether experimental and computational work, planar microfluidic channels are used; experimental work includes Alon et al (1996), Lawrence et al (1997), Chen and Springer (1999), Yago et al (2002), Park et al (2002), Rinker et al (2004) to name a few; computational work includes N'Dri et al (2003), Khismatullin and Truskey (2005), Jadhav et al (2005), Bagchi (2007), Freund (2007) to name a few again. In vivo, the blood vessel has rather complicated topology typically involving bifurcations. In postcapillary venules, in addition, the endothelial wall of high endothelial venues bulges out into the luminal space of postcapillary venules thus increasing the probability of leukocyte–endothelial hydrodynamic interaction or direct collisions (von Andrian 1996).

The capillary-postcapillary junctions are typical examples of bifurcations. The blood flow with cells merges at the junctions where the sophisticated cellular interactions in an otherwise already quite complicated local flow field are involved. It has been shown that leukocytes preferentially roll and adhere in postcapillary venules, and that specific adhesive mechanisms are involved (Ley et al., 1993; Springer 1995). Understanding the cellular interactions is critical to understanding lymphocyte homing and monocyte adhesion in the initial lesion-form stage of atherosclerosis (Ross 1995).

Schmid-Schonbein, Fung and co-workers (1980) are among the first studying the erythrocyte-leukocyte interaction and their role in leukocyte margination towards the blood vascular wall. They studied the cellular interactions within a large-scale flow channel with gradual channel expansion in width using particles to model the erythrocytes and lymphocytes and found smaller particles (as for RBCs) pushed the large particles (as for lymphocytes) towards the channel wall. Based on this, the proposed the erythrocyte-leukocyte interaction could potentially be responsible for the initiation of cell rolling in postcapillary venules and the abundance of leukocyte tethering and adhesion in capillary-postcapillary junctions. Munn and his group studied the phenomena experimentally (Melder et al 2000) and numerically (Sun et al 2003).

However, an abrupt expansion channel model in Sun et al (2003) is used to model the rather complicated postcapillary venules where junctions in form of vascular bifurcations are commonplace. In current work, we go a step further and have analyzed the hydrodynamic interactions of red and white blood cells as they flow from capillaries into a postcapillary venule through the capillary-postcapillary bifurcation. The blood cells are modeled with liquid capsules enclosed with elastic membranes instead of solid particles as modeled in Sun et al (2003). Our results show that capillary-postcapillary junction configuration, RBC distribution in capillaries, and hydrodynamics interactions between cells are critical factors among others determining the margination of leukocytes in postcapillary venules.

6.1 Computational Domain and Parameters

The bifurcations are commonplace rather than rare in microcirculations as shown in Figure 1.4 (cf. Chapter 1). Figure 6.1 shows a model capillary-postcapillary junction bifurcation. This model capillary-postcapillary junction bifurcation in two dimensions has a typical dimension as shown in a sketch shown in Stein et al (1999). The width of the postcapillary venule expansion is 20 μm. The two merging capillaries have widths of 8 μm and 12μm for the top and bottom ones, respectively. To minimize the effects of inflow boundary conditions, we effectively apply an inflow velocity about 100μm per second on both capillary inlets. Pressure boundary condition is used at the outlet. The actual computational domain is a rectangle one with this bifurcation is immersed. The angles between the capillary and the postcapillary are about 30 degrees for both. The computational method is discussed in Chapter 3 and benchmarked in Chapter 4. The resolution is 64 grids for the postcapillary venule width. Leukocyte and erythrocytes will be introduced in later on. To reduce the computational load, we model both leukocytes and erythrocytes as homogenous liquid capsules enclosed with membranes separating more viscous cell interior from extracellular plasma. The leukocyte/plasma has a viscosity ratio of 1000. The leukocyte has a diameter of 8 μm, while the erythrocyte has a diameter of about 5μm instead.

Even without the blood cells, the fluid field is non-trivial for a Cartesian grid method where a structured grid is used. We show the velocity and pressure distribution of the steady state flow field in Figures 6.2a and 6.2b, respectively. The boundary conditions are nearly perfectly implemented and the fluid flow is quite well resolved. The fluid flow are merging from the two capillaries and heading towards the outlet. The Reynolds number is quite small in microcirculations and no flow separation is observed. The same inlet velocities are enforced on capillary inlets, which cause the pressure higher in the top smaller capillary (Figure 6.2b). Please note, the velocity arrows are plotted on slices in x-direction only, not always on cross sections of the bifurcated vessels.

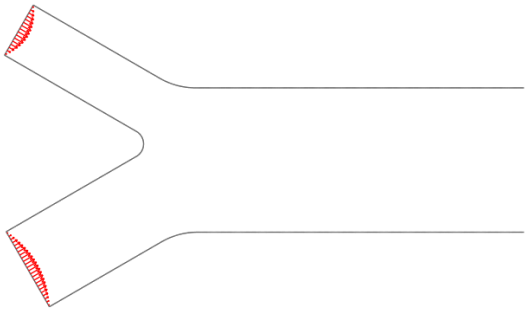

Figure 6.1 A model capillary-postcapillary junction bifurcation (2D), the width of the postcapillary venule expansion is 20 μm, the both merging capillaries have a width of 8 μm and 12μm. The inflow velocities about 100μm per second are effectively specified on the capillary inlets; zero pressure boundary condition used at the outlet. The actual computational domain is a rectangle one with this bifurcation is immersed. The angles between the capillary and the postcapillary are about 30 degrees. Leukocyte and erythrocytes are not shown in this sketch.

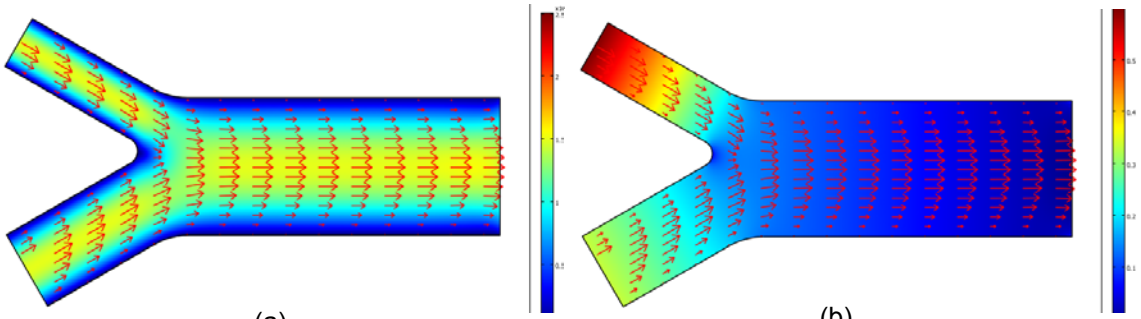

(a) (b)

Figure 6.2 The steady flow field in the bifurcation without any blood cell included: (a) the velocity magnitude; (b) pressure distribution. In both (a) and (b), arrows represent the velocity vectors.

6.2 Case I: Single Leukocyte Motion Through the Bifurcation

We start to introduce blood cells in the capillary and study the cellular interactions through the model capillary-postcapillary junction as shown in Figure 6.1. To examine the cellular interactions in leukocyte margination step by step, we gradually increase the number of cells in both capillaries. In Case I discussed in current section, we introduce a single leukocyte, modeled as a liquid capsule enclosed with elastic membranes, in the bottom capillary and compute the hydrodynamic interaction of leukocyte and the bifurcated blood vessel. The front tracking method

is used to track the cell motion together with the ghost cell method handling the complex geometry as examined in the previous section.

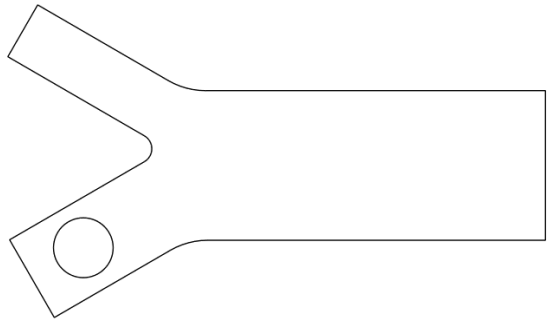

Figure 6.3 A model capillary-postcapillary junction bifurcation (2D) with one leukocyte flowing in from the bottom capillary.

Figure 6.3 shows computational domain and the initial leukocyte (circular object) location. The same boundary conditions used in previous section are applied here (and in following sections) to facilitate comparison later on.

Selected snapshots from the computations are shown in Figure 6.4a-d where the velocity magnitude (color background and legend), velocity arrows, and cell membrane shape (black line) are juxtaposed to show the dynamics of the leukocyte at various time steps. Figure 6.4a shows the cell shape and velocity field shortly after time 0. The velocity field is blunted when the leukocyte is introduced in the bottom capillary due to the higher viscosity of the leukocyte compared with the ambient plasma. The leukocyte gets slightly deformed, mostly at the trailing or upstream portion of it, before it exits the capillary venules and enters the bifurcation (Figure 6.4b). After the leukocyte enters the postcapillary expansion, the leukocyte squeezes the flow from the top capillary. A higher velocity is observed in that region. The leukocyte undergoes a little more deformation but still quite small due to its much higher viscosity. Once the leukocyte leaves the bifurcation region (Figure 6.4d), the leukocyte moves close to the central axis of the postcapillary venule towards the outlet. Once again, the velocity profile is blunted now in the postcapillary venules. And the leukocyte moves slower than plasma without cell presence. We can see this by

comparing the velocity magnitudes between Figure 6.4a and Figure 6.4d. Leukocyte is hardly far away from the blood vascular wall and initial tether even hardly forms.

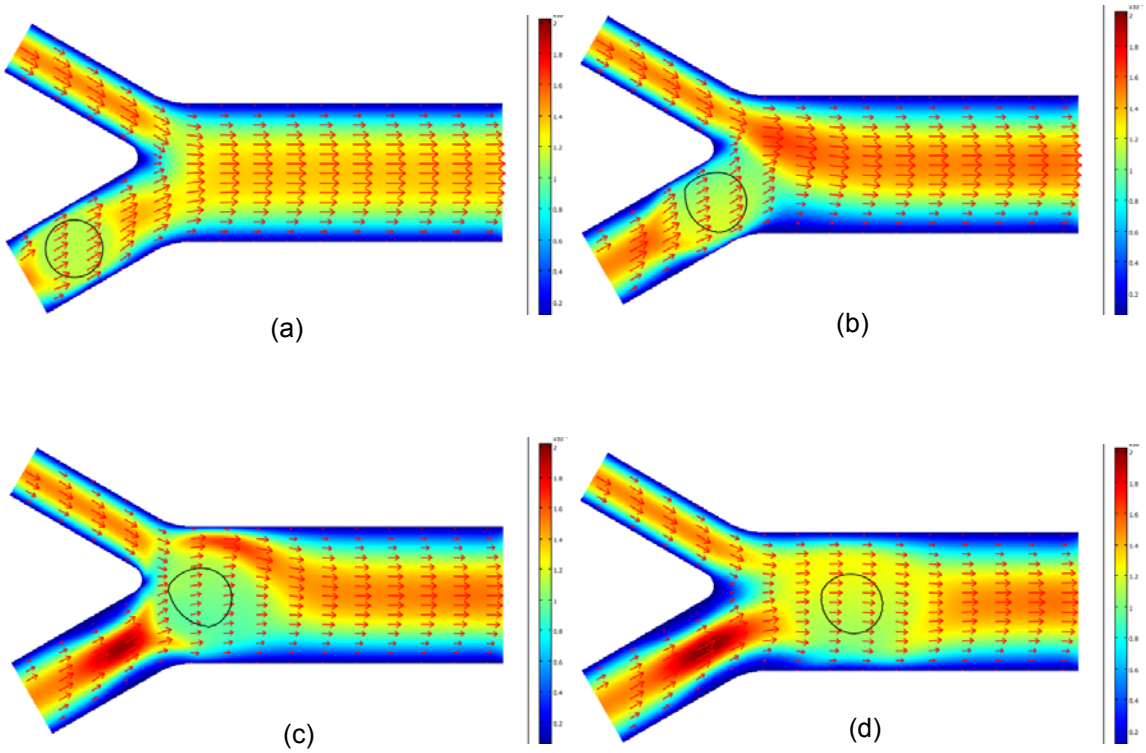

Figure 6.4 Snapshots of a single leukocyte entering the postcapillary venule from the bottom capillary: (a) t = 0; (b) t=0.1; (c) t=0.2; (d) t=0.3.

6.3 Case II: Erythrocyte-Leukocyte Interaction

We assume that the top capillary is cell free or plasma skimmed in case I computed and discussed in previous section. However, more typically, there are cells in both capillaries. In this section, we assume there are two erythrocytes entering from the top capillary as sketched in Figure 6.5. This can have significant impact to the leukocyte trajectory since the cells are expected to interact. We model the multi-cell interactions here and analyze the cell dynamics. However this phenomenon is quite unique for bifurcation and not observable in a model blood vessel expansion simulated by Sun et al (2003). The addition of trailing red blood cells (RBCs)

packed behind a slow-moving leukocyte in capillary circulation will be examined in the later sections.

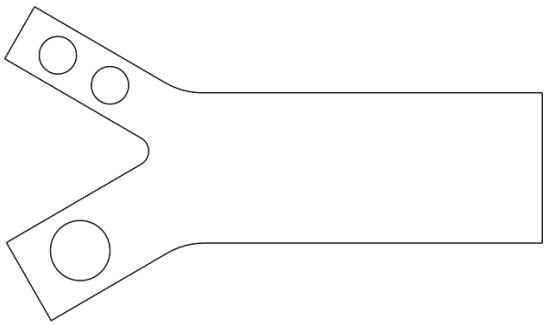

Figure 6.5 A model capillary-postcapillary junction bifurcation (2D) with one leukocyte flowing in from the bottom capillary and two red blood cells entering from the top capillary

Significant difference in the leukocyte motions is observed due to the hydrodynamic interactions between the erythrocyte and leukocytes (Figure 6.9). The snapshots from the computation are shown in Figure 6.6a-d. Figure 6.6a shows the cell shape and velocity field shortly after time 0. The positions of the leukocyte are important in such a model when there are no constant inputs of erythrocytes entering from the capillary as typically happened in vivo. The position is optimized so that the erythrocytes and leukocyte interaction is strong. As the erythrocytes and the leukocyte enter the postcapillary expansion from the top and bottom capillaries respectively, they may collide indirectly or directly and fundamentally change the trajectory of the leukocyte (and erythrocytes). The leukocyte can be seen being pushed closer towards to the bottom vascular wall compared with that when there was no erythrocyte (previous section). As observed in the snapshots in Figure 6.6a-d and more clearly from the corresponding animations (available in internet: www.caip.rutgers.edu/~gaozhu/animations), the erythrocyte-leukocyte interaction effectively applies dynamic forces and torques to each other and leukocyte marginates towards to the endothelial cell layer where receptor can readily form initial bonds to tether and further slow down the leukocytes. As the cell cluster consisting of erythrocytes and leukocyte, enters the postcapillary venule, the more deformable erythrocytes move faster, eventually squeeze though the gap between the leukocyte and endothelial cell layer and pass the leukocyte. Also the more deformable erythrocytes will tend to migrate towards the central axis of

the postcapillary venule, and this can act as another weaker margination mechanism (Freund, 1997).

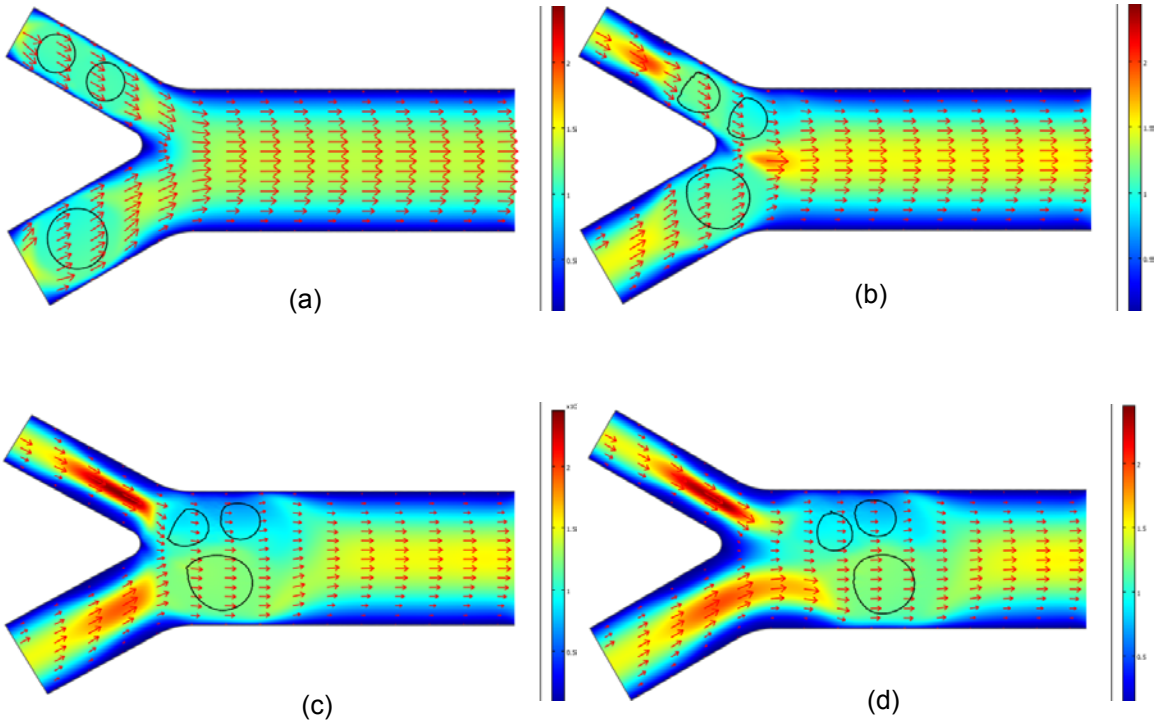

Figure 6.6 Snapshots of a single leukocyte entering the postcapillary venule from the bottom capillary and colliding with two erythrocytes entering the top capillary: (a) t = 0; (b) t=0.1; (c) t=0.2; (d) t=0.3.

6.4 Case III: Erythrocyte-Leukocyte Interaction

We introduce more erythrocytes in the top capillary and test if the hematocrit in the top capillary can affect the leukocyte trajectory and enhance margination further (Figure 6.7).

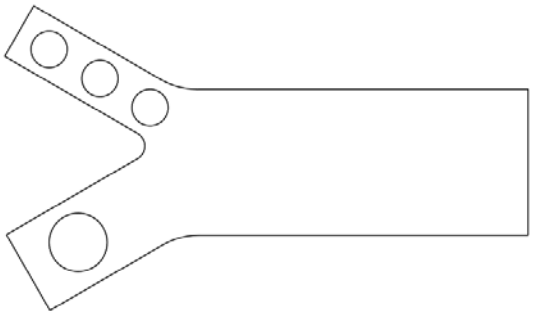

Figure 6.7 A model capillary-postcapillary junction bifurcation (2D) with one leukocyte flowing in from the bottom capillary.

The selected snapshots are summarized in Figure 6.8a-d. No significant change of the leukocyte trajectory is observed. One explanation for this that the first erythrocyte enters much earlier than the leukocyte and most severe hydrodynamics pushing happened before the leukocyte enters the postcapillary expansion. This is captured in Figure 6.8b, where the normalized velocity arrow plot shows that the maximum negative velocity is generated on the further downstream side of the leukocyte. Therefore there may be possible optimal configuration where the leukocyte margination is most salient.

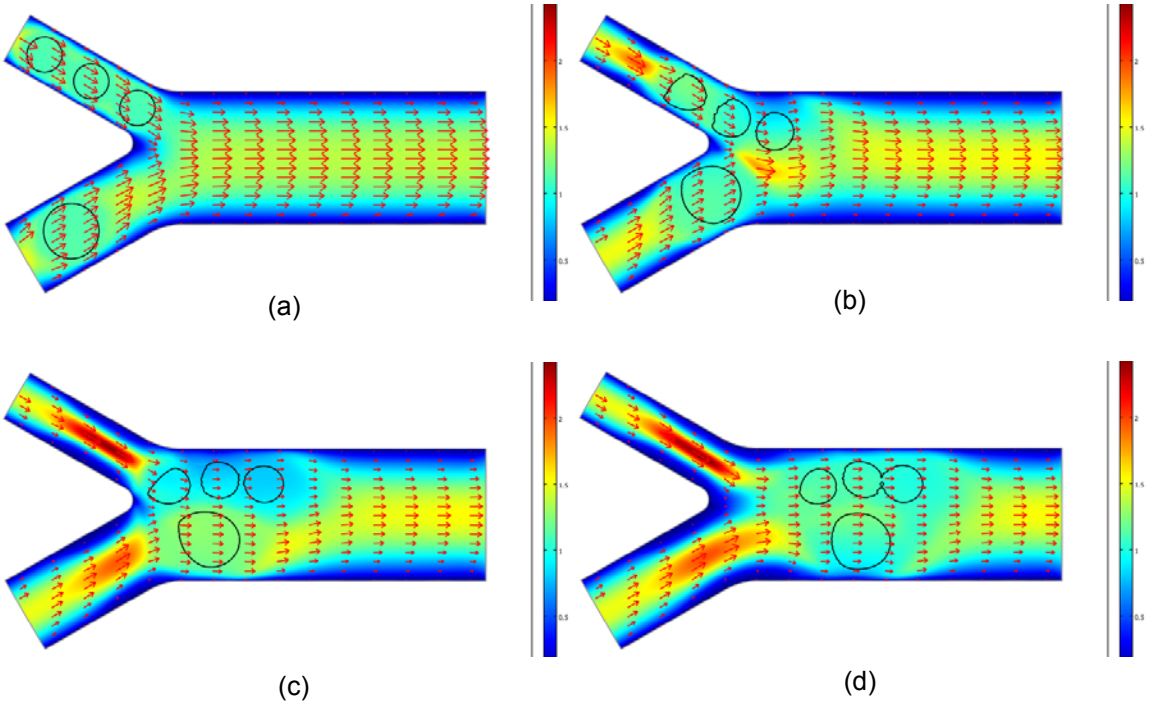

Figure 6.8 Snapshots of a single leukocyte entering the postcapillary venule from the bottom capillary and colliding with three erythrocytes entering the top capillary: (a) t = 0; (b) t=0.1; (c) t=0.2; (d) t=0.3.

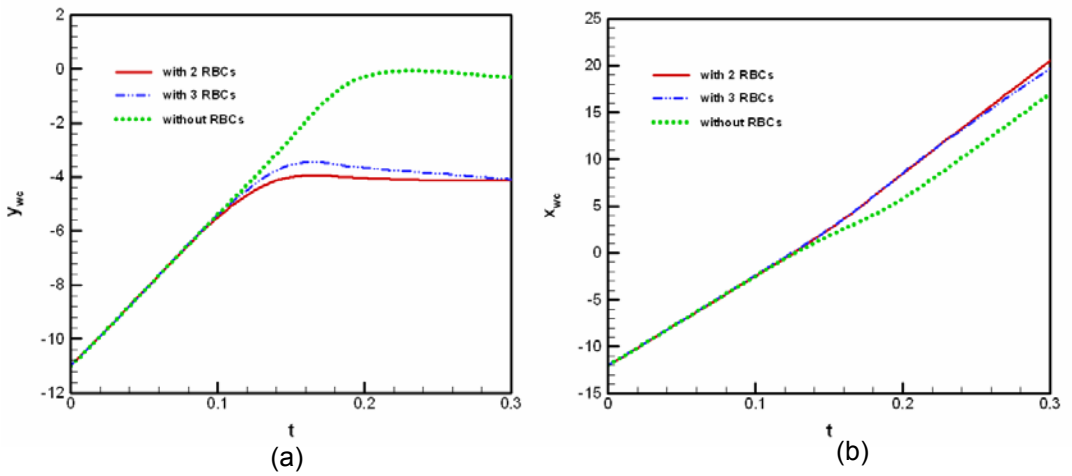

Figure 6.9 Trajectories of the leukocyte motion as a function of time from Cases I (without RBCs), II (with 2 RBCs) and III (with 3 RBCs). The x and y coordinates of the leukocyte mass/volume center are plotted in (a) and (b), respectively.

We compute and plot the trajectories of the leukocyte in Case I, II and III in Figures 6.9a and 6.9b for the x-coordinates of the leukocyte mass or volume center. From Figure 6.9a, we clearly see that the leukocyte has been pushed much closer to the blood vascular wall with erythrocytes entering from the other capillary. The margination is about 4 μm closer to the wall. The leukocyte y trajectories reach plateaus due to the limited number of erythrocytes considered in current work. In vivo, this factor is expected to become more salient with more frequent hydrodynamic interaction and collision between the erythrocytes and leukocytes. The negative slopes indicate the importance of cell-free layer formation due to migration of less deformable erythrocytes towards to the postcapillary venule central axis. The slope for case III is decreasing faster than case II since more erythrocytes are involved in case III, 3 vs. 2. The streamwise trajectories of the leukocyte are also changed due to the presence of erythrocytes. The slope change of the leukocyte without the presence of erythrocytes is due to the local flow pattern close to the bifurcation and the leukocyte oscillates in certain sense. Please note, that the fixed and same velocities are specified on the inlets of the capillaries. Accepting this assumption, we observed that the leukocyte moves faster due to the horizontal pushing of the erythrocytes to it.

6.4 Case IV: Erythrocyte-Leukocyte Interaction

The trailing erythrocytes accumulated behind a slow moving leukocyte have been shown to play a significant role in leukocyte margination in postcapillary venules (Schmid-Schonbein et al 1980; Melder et al 1996; von Andrian 1996). As the leukcotye enters the postcapillary venule with expansion and merging bifurcation (Figure 6.10), the erythrocytes tend to push the leukocytes vertically and horizontally. Vertical pushing leads to enhanced leukocyte migration towards the postcapillary endothelial cells. The mixed vertical and horizontal pushing also can lead larger deformation of the leukocytes contact area with the endothelial cells. Also as the erythrocytes are forced to pass the leukocyte, the pushing can become quite significant.

This has been confirmed in our computations where trailing red blood cells are included Cases IV (this section) and V (next section). The computational configuration for Case V is shown in Figure 6.10, where a single trailing erythrocyte is included. We will show that even a single trailing erythrocyte changes the leukocyte motion significantly. However the observed behavior is quite different from Sun et al (2003), where they are missing two very important factors: 1) erythrocytes entering from other capillaries; 2) deformability of blood cells.

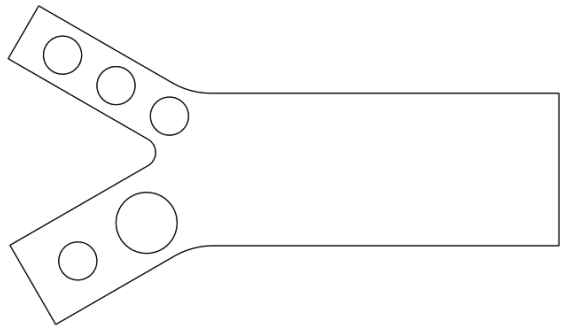

Figure 6.10 A model capillary-postcapillary junction bifurcation (2D): one leukocyte entering from the bottom capillary with a trailing erythrocyte, three erythrocytes entering from the other capillary. This is extension of Case IV.

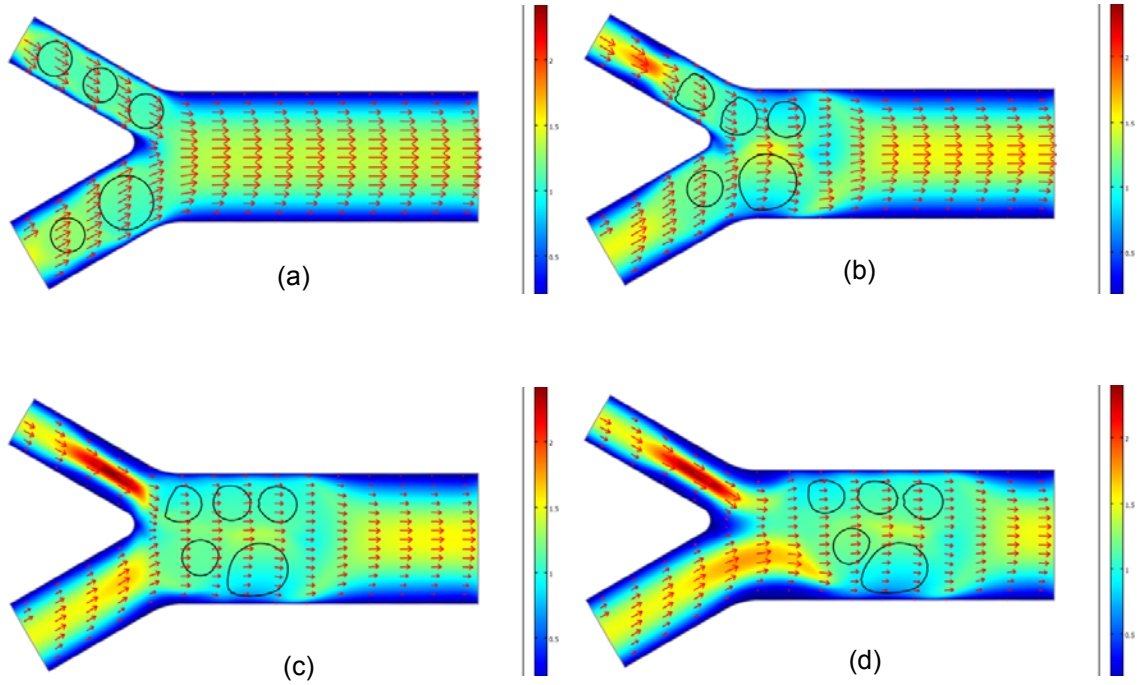

Figure 6.11 Snapshots of one leukocyte entering from the bottom capillary with a trailing erythrocyte, three erythrocytes entering from the other capillary: (a) t = 0; (b) t=0.1; (c) t=0.2; (d) t=0.3.

The results are summarized in Figure 6.11. Compared with case IV where there is a trailing erythrocyte, enhanced leukocyte margination and more salient deformation are observed. The droplet-like shape of the leukocytes allows larger contact area with the endothelial cells and hence more bonds can be formed there. As the trailing erythrocyte and erythrocytes entered originally from the other capillary pass over the deformed leukocyte, the leukocyte is deformed even more. These phenomena can be critical in vivo where the automatic braking or stabilization of the leukocyte tethering, adhesion and rolling are observed (Firrell and Lipowsky 1989; Lei and Dong 2000; Yago et al 2002).. Also with more erythrocytes included, the frequency where the erythrocytes interact with the leukocyte is also enhanced.

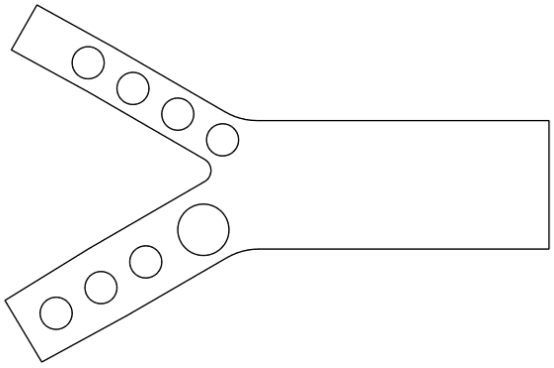

Figure 6.12 A model capillary-postcapillary junction bifurcation (2D): one leukocyte with multiple trailing erythrocytes and ones entering from the other capillary. The capillaries are elongated to be able to add more blood cells compared with previous cases.

6.6 Case V: Erythrocyte-Leukocyte Interaction

More erythrocytes can be readily added to the model to make it even closer to in vivo (Figure 6.12). Similar observations can be made based on the snapshots of the computational results as shown in Figure 6.13.

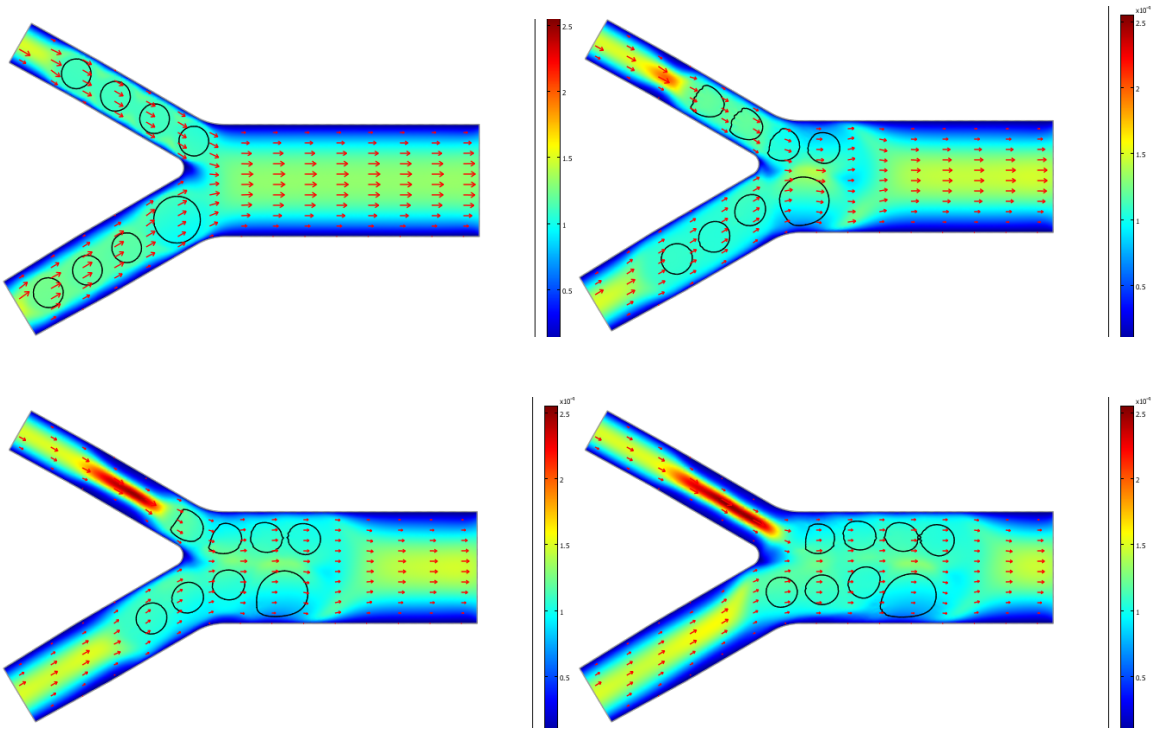

Figure 6.13 Snapshots of one leukocyte entering from the bottom capillary with multiple trailing erythrocytes and multiple erythrocytes entering from the other capillary: (a) t = 0; (b) t=0.1; (c) t=0.2; (d) t=0.3.

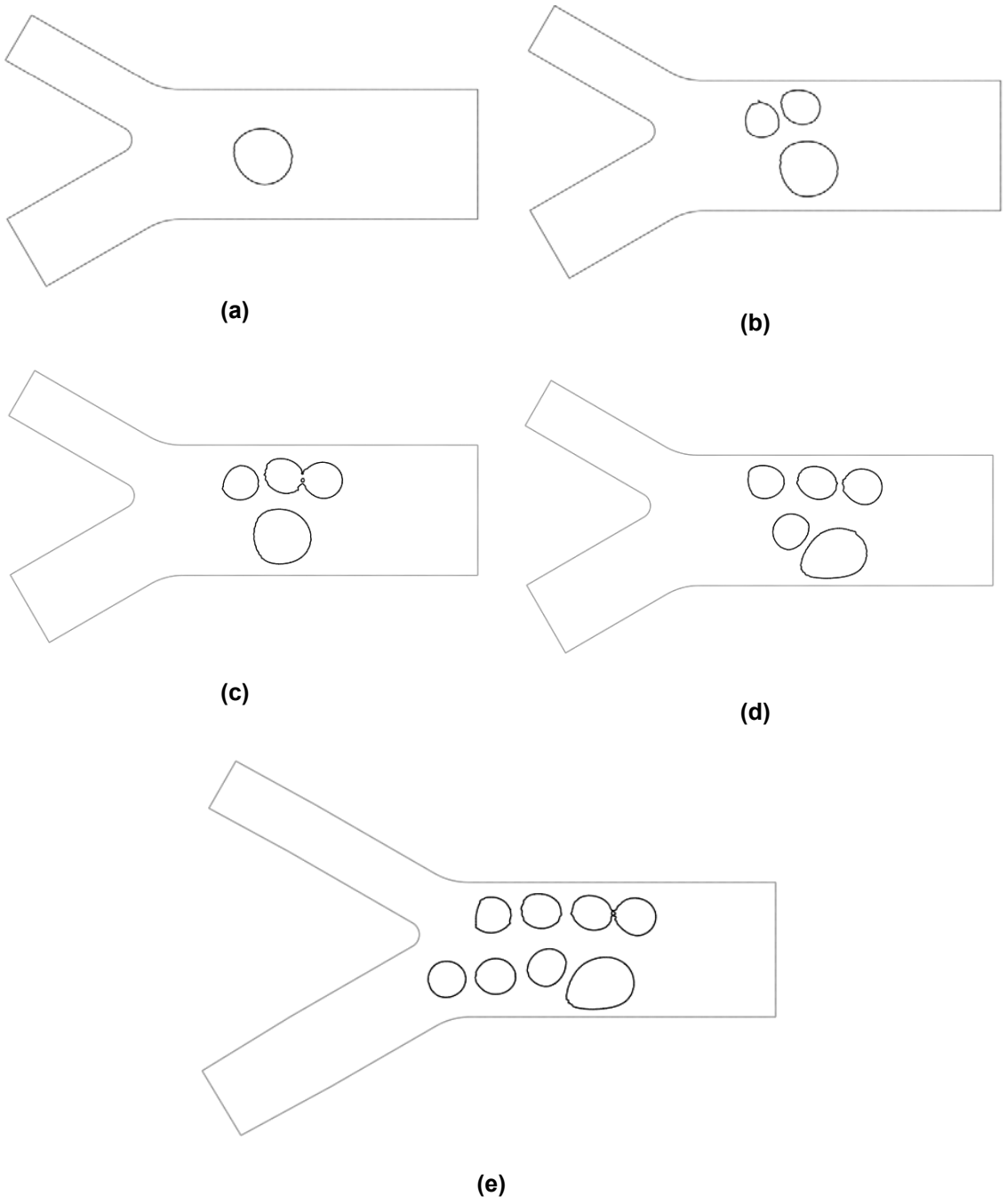

Figure 6.14 Juxtaposition of the cell distribution at the end of the computations (time 0.3 second): (a) case I, (b) case II, (c) case III, (d) case IV, and (e) case V.

We juxtaposed the final time-step snapshots from Cases I, II, III, IV, and V in Figure 6.14. The number of erythrocytes (hematocrit), the initial distribution of the erythrocytes, the vessel geometry play critical roles in leukocyte margination and initial tethering. Cellular interactions and vessel geometry plays a critical role in initiating contact between circulating leukocytes and endothelial ligands under physiologic conditions.

In conclusion, erythrocyte-leukocyte interactions and vascular geometries play critical roles in leukocyte margination and initial tethering to the vascular endothelium,

1). Bifurcation geometry of the capillary-postcapillary venules is first included to compute the cellular interaction and the geometric effects. This has been shown to probably be another contributing factor in enhancing leukocyte margination, initial tethering, adhesion, rolling and final transmigration.

2). RBC-induced fluid mechanical forces and RBC-mediated dispersion, directed predominantly toward the wall, tend to push a leukocyte towards to the blood vascular wall and keep leukocyte in close proximity to the vessel wall.

3). Impact of RBCs on leukocytes may also increase the contact area between the leukocyte and the vessel wall and hence increase the number of receptor-ligand bonds formed for a leukocyte. And the increasing contact area of the leukocyte-endothelium also can serve an automatic braking system for surprisingly stable leukocyte rolling observed in vivo and in vitro with increasing shear stress (Chen and Springer 1999).

4). More deformable RBCs also tend to move toward to the central axis of the blood vessel (Bagchi, 2007 for two dimensional planar channel) and a RBC-free layer forms close to the blood vascular wall. This global movement of the RBCs is another contributing factor to the leukocyte migration as shown in Freund (2007) where a planar channel is modeled. Evidence: In support of this hypothesis is the observation that cell rolling and adhesion occurred in the presence of RBCs, but not in the absence of RBCs at high shear rates (in vivo vs. in vitro).

Chapter 7

Summary and Conclusions

For Part I

The multiphysics phenomena of cellular interaction and adhesion in complex geometries are examined in this work. The code is based on the mixed front tracking and ghost cell methods. The former allows us to model the cells as liquid capsules enclosed elastic membranes; and the later provides the capability to model flow in complex geometries without using a curvilinear grid. The code was benchmarked and validated with carefully selected problems, including flow around a rigid cylinder, flow over a model wavy endothelial cell surface, droplet and capsule in linear shear flow, and oscillating bubble. Excellent results were obtained.

We then applied the code to compute cellular interaction in planar and wavy microvessels. Leukocyte interaction, deformation and adhesion are observed and consistent with experimental results. The possible waviness of a microvessel had mostly been neglected in literature. We observed that significant variation of pressure and shear stress are induced by the waviness of the microvessel, which can become of comparable order with molecular bond force in adhesion.

In the multistep leukocyte adhesion cascade, a leukocytes, circulating in the blood flow abounded with erythrocytes, has to come close enough to the blood vascular wall so that receptor-ligand bonds can form before it gets tethered and rolling along the endothelial cell monolayer lining the blood vessel lumen. The effective length of the receptor-ligand complex is typically less than 1 μm. There are several possible biophysical mechanisms for this leukocyte margination process, including the particulate nature or rheology of the blood flow involving

cellular interactions (including erythrocyte-leukocyte interaction and leukocyte-leukocyte interaction), vascular network geometry, irregular topology of the endothelial cell monolayer (particularly for the high endothelial cells in postcapillary venules), and local flow patterns. In the last part of this work, we investigate these contributing factors. We are the number ones to the author's knowledge who examine the cellular interactions through a capillary-postcapillary junction bifurcation instead of an ideal planar flow channel or a channel with abrupt and nonrealistic expansion. Our results suggest hematocrit, cellular interactions, and vascular geometry are critical factors that determine the margination and initiation of rolling in postcapillary venules:

1). RBC-induced fluid mechanical forces and RBC-mediated dispersion, directed predominantly toward the wall, tend to push a leukocyte towards the blood vascular wall and keep leukocyte in close proximity to the vessel wall.

2). Impact of RBCs on leukocytes may also increase the contact area between the leukocyte and the vessel wall and hence increase the number of receptor-ligand bonds formed for a leukocyte. And the increasing contact area of the leukocyte-endothelium also can serve an automatic braking system for surprisingly stable leukocyte rolling observed in vivo and in vitro with increasing shear stress (Chen and Springer 1999).

3). More deformable RBCs also tend to move toward to the central axis of the blood vessel (Bagchi, 2007 for two dimensional planar channel) and a RBC-free layer forms close to the blood vascular wall. This global movement of the RBCs is another contributing factor to the leukocyte migration as shown in Freund (2007) where a planar channel is modeled. Evidence: In support of this hypothesis is the observation that cell rolling and adhesion occurred in the presence of RBCs, but not in the absence of RBCs at high shear rates (in vivo vs. in vitro).

4). Geometry feature of the capillary-postcapillary venules are fist included computationally to study the geometric effects and the cellular interaction. This has been shown to probably be another contributing factor in leukocyte margination, initial tethering, adhesion, rolling and final transmigration. Also we show some saliently different effects, which would not be able to be observed otherwise.

5). Similarly for leukocyte-leukocyte interaction and adhesion.

In the future, a full 3D dimensional model would need to be built in order to study the 3D effects and compare with experimental observations.

PART II:

VORTEX-ACCELERATED VORTICITY DEPOSITION IN THE RICHTMYER-MESHKOV INSTABILITY

Chapter 8

Introductions, Overview and Numerical Methods

8.1 Introductions and Overview

Fluid mixing motions are fundamental in varieties of stratified interfacial flows. Hydrodynamic instabilities can lead to the complication and tangling of an interface and to the mixing of different materials. Three of the most classical ones are the Kelvin-Helmholtz (KH), Rayleigh-Taylor (RT) and Richtmyer-Meshkov (RM) instabilities. In this work, we focus on the Richtmyer-Meshkov instability where a shock wave (e.g. a power laser) accelerates a stratified fluid interface. It is also called the impulsive Rayleigh-Taylor instability while the classical Rayleigh-Taylor instability refers to the case where the acceleration is a constant such as gravity. However the vortex accelerated vorticity deposition mechanism discovered in current work is universal and applies to all stratified fluid flows. We will give a short introduction and overview of the recent work on the Richtmyer-Meshkov instability. For a full introduction and more complete summary of the most recent advances in the Richtmyer-Meshkov instability, we refer to two most recent excellent reviews by Zabusky (1999) and Brouillette (2002). The former emphasizes the vortex paradigm and discusses different RM configurations and introduces the unifying concept of the vortex projectile up to early-intermediate times. The latter concentrates particularly on the sinusoidally perturbed RM interface, mainly up to early times.

As we all know, the KH instability arises due to a jump in the tangential velocity along the interface, and hence it is also called shear instability. It can exist in both uniform or stratified cases. However, both RT and RM instabilities are due to density stratification subject to acceleration. When the acceleration is constant, it is called RT instability. When the acceleration is in the nature of impulse, it is instead called RM instability. There are close relations between these instabilities. In the latter two cases, vorticity is baroclinically deposited along the interface and forms a shear layer and hence the KH instability comes to play an important role as we may have expected. However more importantly, the coherent vortices will also induce a centripetal acceleration and this acceleration is not necessarily aligned with the density gradient on the fluid interfaces, and therefore the vorticity will continue to be generated baroclinically. At the same time the interface is kept being stretched and the density gradient across the interface keep increasing especially where the mixing is not significant. Naturally this acts as a new baroclinic source without external acceleration but the vortex dynamics of the fluid itself, generates new secondary vorticity, continues to enhance the mixing, and leads to eventual turbulent flow in the mixing region. We will discuss these contributions from current work to the field in detail in Part I of this dissertation.

The heavy investigations of RM instability in the last two decades are closely related to the resurrected research in the inertial confinement fusion (ICF), supersonic combustion, astrophysics, and nuclear weapons. In astrophysics, RM instability has been proposed as the cause of formations of mushroom structures and subsequent mixing in a supernova remnant (Arnett, 2000). In inertial confinement fusion (ICF) the RM instability of the impulsively accelerated shell containing the deuterium-tritium fuel limits the compression of the fuel that is important to achieve the high temperature where the nuclear reaction releases enormous amounts of energy. Thus RM instability represents a significant obstacle to achieving a productive fusion reaction (Lindl, 1995). The inertial confinement fusion has the promise to become one of the next-generation clean and inexhaustible energy resources. The fundamental mechanisms of RM instability have also been considered to be of importance to enhancing mixing in supersonic combustion (Yang et al, 1993). The RM instability is critical in nuclear weapon simulations under

the Advanced Simulation and Computing (ASC) Program, which supports the Department of Energy's National Nuclear Security Administration (NNSA) Defense Programs' shift in emphasis from test-based confidence to simulation-based confidence. Under ASC, computer simulation capabilities are developed to analyze and predict the performance, safety, and reliability of nuclear weapons and to certify their functionality. ASC integrates the work of three Defense programs laboratories (Los Alamos National Laboratory, Lawrence Livermore National Laboratory, and Sandia National Laboratories) and university researchers nationally into a coordinated program administered by NNSA.

A sinusoidal single-mode perturbed planar interface between two fluids of different densities accelerated by a shock wave is always unstable whether the shock is coming from a heavy fluid to a light fluid (slow/fast) or from a light fluid to a heavy fluid (fast/slow). The perturbation amplitude growth is initiated by primary vorticity deposited on the interface baroclinically due to the misalignment of the density gradient across the interface and the pressure gradient across the shock wave. Soon the interface amplitude grows and develops a characteristic "spike-bubble" structure, where the vorticity rolls-up in a "Kelvin-Helmholtz" manner and is concentrated toward the heavy spike region in a "mushroom" head.

The classical single-mode harmonically perturbed interface under impulsive acceleration due to a shock wave was first rigorously studied by Richtmyer (1960). Almost a decade later, the laser tube experiment by Meshkov (1965) confirmed qualitatively the predictions of Richtmyer. This class of instabilities is now named after them. RM instability is closely related to the well-known Rayleigh-Taylor (RT) instability. Taylor was the first to study the growth of small single-mode harmonic perturbations to a flat interface between two fluids of different densities under constant acceleration (gravity) using linear stability theory. Richtmyer (1960) used Taylor's results as the basis for his similar analysis of RM instability in which he modeled the shock interaction with an interface as the impulsive acceleration of two incompressible fluids.

So far, *all* experiments and most numerical simulations studied the dynamics and scaling up to early times, i.e. for a *small* time interval after the primary vorticity deposition phase. A recent study by Zabusky *et al.* (2003a) systematically examined properties to *early-intermediate* times

and disagreed with the application of the amplitude growth rate $\dot{a}$ (the amplitude a is defined as the half distance between the spike and bubble ends) estimates of Zhang and Sohn (1997). The *late time* scaling of $\dot{a}$ for a two-dimensional (2D) single-mode RM interface is still controversial, although reasonable prediction has been provided by the potential theory for Atwood number, defined as $A = (\rho_2 - \rho_1)/(\rho_2 + \rho_1)$ = 1 limit and by a single point vortex model for the *A* = 0 limit. Note, none of these approximations of late time dynamics includes the new phenomena presented in this thesis and the agreement, if any, is fortuitous. This part of the thesis and other relevant work in this direction has been published in four papers in series in Journal of Fluid Mechanics (2003a), Physics of Fluids (2003b), Physics of Fluids (2004), and Physics of Fluids (2006).

In his pioneering work on the linear analysis of the Richtmyer-Meshkov instability, Richtmyer (1960) modeled the impulsive acceleration as a delta function pulse, substituted it for the constant gravity acceleration in Taylor's formulation for Rayleigh-Taylor instability, and obtained an approximate formula for the perturbation or amplitude growth rate in the incompressible limit as

$$\dot{a}_{imp} = k a_0^* A^* \Delta U, \tag{8.1}$$

where ΔU is the post-shock interface velocity, k is wavenumber, a_0^* is the post-shock perturbation amplitude, and $A^* = (\rho_2^* - \rho_1^{**})/(\rho_2^* + \rho_1^{**})$ is the post-shock Atwood number (the planar shock wave moves from ambient fluid ρ_1 to transmitted fluid ρ_2, and ρ_2^* is the density in the transmitted fluid after the transmitted shock has passed, and ρ_1^{**} is the density in the ambient fluid after the reflected shock wave has moved upstream). This is the well-known Richtmyer's impulsive model for the case of a reflected shock only, which was derived in a small part of his seminal paper. Zhang and Sohn (1997) introduced the first systematic procedure for a nonlinear solution of the 2D incompressible Euler equations by calculating four terms in Taylor

series in times. To improve the temporal range of validity, they introduced a Pade resummation technique which presumed a late time behavior for $\dot{a}$ which vanishes. Zhang and Sohn (1997) agreed with Sadot *et al.* that $\dot{a}$ approaches zero "asymptotically" for a single-mode RM 2D configuration for all $A < 1$. Zabusky *et al*. (2003a) computed 11 terms in the series and showed that the Pade approximation was ad-hoc. Their solutions agreed well with numerical simulations until the multivalue time, t_M, at which the initially single-valued interface curve first becomes *multivalued*. In all their comparisons, higher-order [*n, n*] Pade approximant give better agreement with simulations than [*0, 2*] or [*0, 1*] of Zhang and Sohn (1997) although there seems to be no best *n* available. We discuss the subtleties of defining t_M for realistic simulations with a *small-but-finite* interfacial transition layer later on.

However, our simulations to late-intermediate times discussed in chapter 9 show that $\dot{a}$ approaches a *constant* which increases with varying $A^* \leq 0.9$. This arises in part because of the *new* phenomenon of *vortex accelerated vorticity deposition* (VAVD), as quantified here, where vorticity of both signs (depending on the density gradient) appears in close proximity within the interfacial domains, namely a vortex bilayer. It rollup into a *"complex"* vortex dipole or "vortex projectile", which accounts for the constant amplitude growth rate at late-intermediate times. This 'secondary' vorticity deposition has contributed to the growths of the negative and positive circulations, the integrated vorticity, and also the total circulation growth. The total circulation growth is distinctive from the simple shear layer, where the circulation is constant all the time. The secondary vorticity has become dominant before or around the multivalue time of the interface. In this work, we also present a new simple diagnostic formula, involving a pressure difference, for determining the rate–of-change of total circulation, $\dot{\Gamma}_D$, within a bounding domain D. The formula is derived analytically and verified computationally. We show that for intermediate times (up to t/tM < 8.0), $\dot{\Gamma}_D / (\Gamma_{shock} / t_M)$, has several consistent behaviors and scaling laws depending on A*. Here Γ_{shock}, is the circulation deposited by the initial shock.

This VAVD is also present in a 2D stratified mixing layer (Reinard et al 2000, Soteriou and Ghoneim 1995, Staquet 1995) and also in long-time stratified incompressible vortex sheet simulations with surface tension of Hou *et al*. (1997). This is a universal phenomenon in stratified or inhomogeneous flows and will be crucial in geophysics and astrophysics where stratification is ubiquitous.

8.2 Computation method and parameters

8.2.1 Interface Transition Layer (ITL) and Extraction/Tracking

A. Introduction of ITL

In two-dimensional (2D) inviscid Euler simulations for ideal gas dynamics, the RM interface has often been modeled as a thin contact discontinuity layer (CDL), two or three computational zone wide. The CDL acquires primary vorticity after the passage of the shock wave. An analysis of a 2D incompressible inviscid Raleigh-Taylor (RT) configuration (Baker et al, 1993) shows a vortex sheet becomes singular in a finite time. This ill-posed behavior is further numerically examined by Samtaney and Pullin (1996) for a compressible RM configuration and they found small-scale secondary rollups appear on the interface at times which decrease as the finite-difference resolution increases (CDL thickness decreases as the size of the cell decreases), or alternatively, the maximum value of the vorticity increases. Comparisons of simulations of the 2D RM problem among several codes show poor agreement when concern for the resolution of the CDL is not carefully controlled (Holmes et al., 1999).

In preliminary work with a 2D contour dynamics (Pullin, 1992) simulation of an incompressible homogeneous density thin vortex layer (Dritschel, private communication), we observed similar rapidly growing small-scale roll-ups of the layer *before* the large-scale single mode first is observed to become multi-valued. Here these rollups are associated with the most unstable mode which is most likely excited by small-scale numerical perturbations.

Since the simulations in this paper are to model the experiment of Jacobs and Krivets (2001), named JK01 from now on, namely no small-scale roll-ups prior to the "*multivalue time* ", t_M , as discussed below, we use a *small-but-finite* thickness interfacial transition layer (ITL) corresponding to a physically diffuse interface. This procedure initially regularizes the vortex sheet. The layer thickness should be sufficiently thin to model the physical diffusion occurring during the experimental set-up, e.g. as described by Jones and Jacobs (1997), and sufficiently thick so that no secondary structures arise prior to the multivalue time of the interface, e.g Jacobs and Krivets (2001).

B. Numerical determination of the medial axis of the ITL

We apply two systematic techniques to extract the evolving complex interface and the spike and bubble ends. First, the zero crossings of the Laplacian of the density ($\nabla^2\rho = 0$) are used to extract the entire interface (Samtaney and Zabusky 2000). A linear interpolation procedure is used to identify where the zone edges intersect the zero contour of the Laplacian of density. Edges in the low density-gradient ($|\nabla\rho|<|\nabla\rho|_{threshold}$) region are excluded. The density gradient threshold $|\nabla\rho|_{threshold}$ is set to 10% of the maximum, i.e. $|\nabla\rho|_{threshold} = 10\%|\nabla\rho|_{max}$. A sample of such a curve at t/t_M = 3.46 is in Figure 8.1, and the simulation will be described fully below. It shows important characteristic length scales used for comparison with experiment: neck width W_{neck}, spanwise expansion W_{span} and streamwise elongation W_{stream}. The algorithm successfully captures all large-scale curvatures, e.g the smooth spike and bubble regions, and intermediate scale rollups. However, the small-scale rollups lead to discontinuous fragments, a subject under investigation.

A different algorithm using the passively advected Lagrangian particles is applied. The Lagrangian particles are distributed along the initial interface curve in 2D where $\rho = (\rho_1 + \rho_2)/2$. Two well known issues with the Lagrangian particle tracing is the clustering when the particles get too close each other and leak where the two particles are getting too far away from each other.

As the initial interface keeps being stretched, particles might be clustered in the roll up regions while at the same time the particles will be enough to resolve the interface segment where the interface stretches most in the bubble regions for example. To overcome these issues, the Lagrangian particles are being added or deleted dynamically as following:

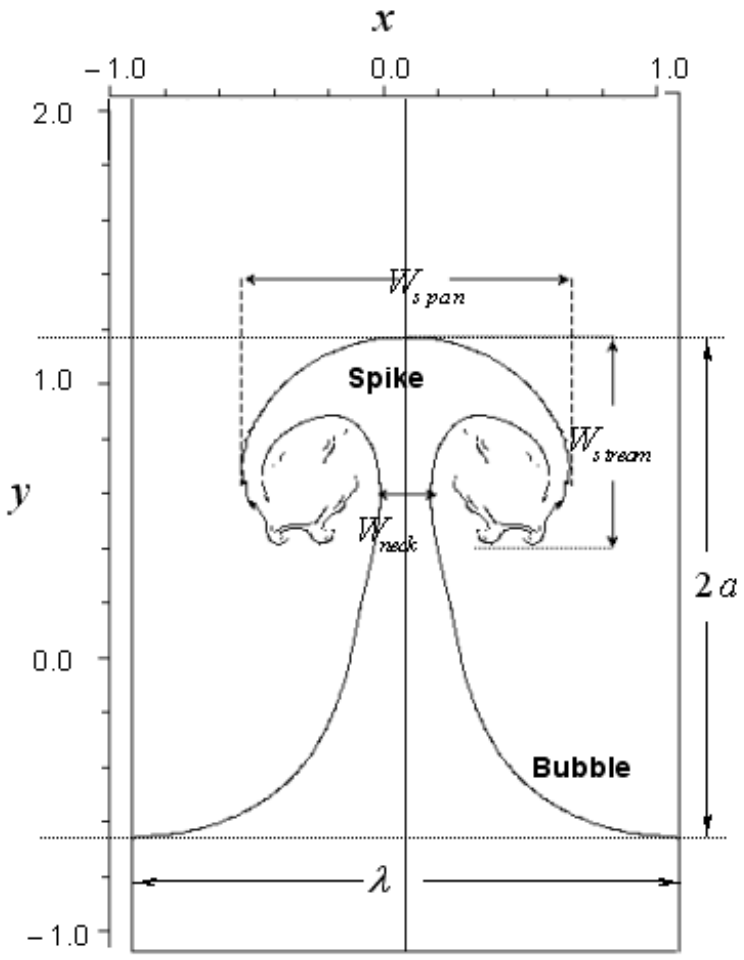

Figure 8.1 Extracted interfaces ($\nabla^2 \rho = 0$ in high gradient regions) for $A^* = 0.635$ at t/t_M = 3.46. W_{span}, W_{stream} and W_{neck} are spike spanwise width, streamwise width and neck width, respectively.

1. The first step in this algorithm is the advection of the marker particles. A simple bilinear interpolation is used to find the marker velocity.

2. The marker particles are then advected in a Lagrangian manner using a straightforward second order Runge-Kutta scheme
3. As the interface evolves, the markers drift along the interface following tangential velocities, and more markers may be needed if the interface is stretched by the flow. We then need to redistribute the markers in order to ensure an homogeneous distribution of points along the interface. This is done at each time step using the interpolating curve (x(s), y(s)). As s is an approximation of the arc length, if a redistribution length l is chosen, the new number of markers is Nnew_sN:l and the points are redistributed as (xinew, yinew)_(x(il), y(il)). l is usually chosen as h, which yields an average number of 4 markers per computational cell.

Figure 8.2 shows the juxtaposition of the extracted and tracked interfaces. The Lagrangian tracking can capture the dynamics change of the interface better however the extraction can capture more features but is hard to tune the threshold sometimes.

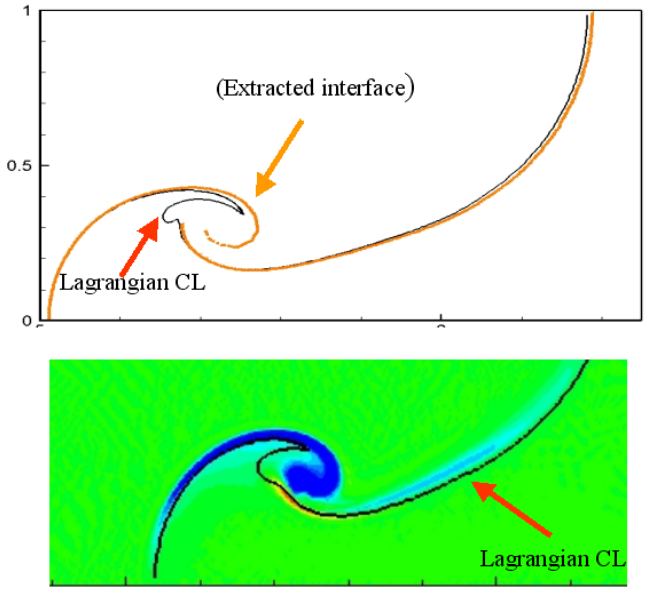

Figure 8.2 Extracted interfaces ($\nabla^2 \rho = 0$ in high gradient regions) for $A^* = 0.635$ and the tracked interface with the Lagrangian markers.

C. The multivalue time t_M

The use for scaling of the multivalue time t_M when the interface first becomes multivalued was heuristically suggested in Zabusky *et al.* (2003) who used it for careful comparisons among different Atwood number evolutions to early-intermediate times with an incompressible contour-advective semi-Lagrangian (CASL) code where the interfacial curve is tracked (Dritschel and Ambaum, 1997).

For an initial diffuse ITL, such a curve is the *extracted* medial axis of the ITL and is defined by using the algorithms above. As for spatial convergence, if the initial resolution of the ITL is sufficient (larger than 30 grid zones) the extracted medial axis is within one grid zone, as the resolution increases from 360 zones to 540 zones per wavelength. For temporal convergence, t_M varies within one percent.

8.2.2 Equations, Numerical Method, and Parameters

A. Euler Equations

Two-dimensional compressible single-mode Richtmyer-Meshkov interfaces with an interfacial transition layer (ITL) at different Atwood numbers are investigated. The evolution of the fluid motions are governed by the 2D Euler equations

$$\begin{bmatrix} \rho \\ \rho u \\ \rho \mathrm{v} \\ E \end{bmatrix}_t + \begin{bmatrix} \rho u \\ \rho u^2 + p \\ \rho u \mathrm{v} \\ u(E+p) \end{bmatrix}_x + \begin{bmatrix} \rho \mathrm{v} \\ \rho u \mathrm{v} \\ \rho \mathrm{v}^2 + p \\ \mathrm{v}(E+p) \end{bmatrix}_y = 0, \tag{8.2}$$

where ρ is density, u is the component of velocity in spanwise (x) direction, v is the velocity component in streamwise (y) direction, $E = \rho e + \rho(u^2 + v^2)/2$ is total energy per unit volume, e is the internal energy per unit mass. Pressure is derived from equation of state as $p = (\gamma - 1)\rho e$. Boundary conditions are reflective in x directions ($\mathbf{u} \cdot \mathbf{n} = 0$), and zero-gradient in- or out-flow in y directions (Figure 8.3). In the codes, the ghost cells are used to enforce the reflective and zero-gradient boundary conditions.

The Euler equations do not take into the viscosity of the fluids. But in the initial and intermediate times, this is a reasonable assumption. During the strong mixing spiral vortex core regions, the numerical viscosity plays an equivalent role as the physical viscosity as in the MILES approach (Porter et al, 1994) to dissipate the energy.

B. Piece-wise Parabolic Method (PPM)

We solve numerically the Euler equations using piece-wise parabolic method (PPM) of Colella and Woodward (1984). The PPM scheme represents a substantial advance in classical first-order Godunov schemes. It is second order accurate close to discontinuity and otherwise fourth order accurate. It has been widely used in compressible Richtmyer-Meshkov instability and subsequent turbulence mixing studies, for example Department of Energy Flash Center and Lawrence Livermore National Laboratory. Numerical diffusivity and dispersion are the serious issues either in evaluating the numerical mixing and “turbulent” behavior in our current study or for tracking the instead sharp interfaces. Therefore, it is worth analyzing the mass and vorticity diffusivities in PPM schemes.

It is hard to analyze the full nonlinear systems. But some lights may be shed on these effects by investigating the differential approximation or local error analysis for the linear advection equations (following the notation and work of Colella and Woodward),

$$\frac{\partial a}{\partial t} + u\frac{\partial a}{\partial \xi} = 0 \tag{8.3}$$

$$a(\xi,0) = a_0(\xi)$$

This equation can be regarded as a model for the contact discontinuity in gas dynamics. For simplicity, we assume $u > 0$ and consider the scheme for uniform Eulerian grids. For completeness, we present the derivation of the PPM advection schemes in detail and perform the numerical diffusivity analysis to the end.

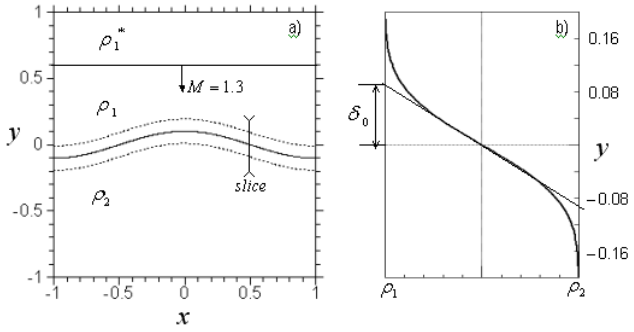

Figure 8.3 (a) Sketch of the shock/diffuse interface interaction, (b) (slice) error function profile of the initial transition layer with maximum slope thickness $2\delta_0$.

Let $\xi_{j+1/2}$ be the boundary between the j th and the $j+1$ st zones on the computational grid. Given a_j^n the zone average solution at t_n, we want to calculate a_j^{n+1} the zone average solution at t_{n+1},

$$a_j^n = \frac{1}{\Delta x}\int_{\xi_{j-1/2}}^{\xi_{j+1/2}} a(\xi)d\xi \tag{8.4}$$

where $a(\xi)$ is the interpolation function in the reconstruction step which was piecewise constant equal to a_j^n in the first-order original Godunov scheme. PPM advocates the use of piecewise parabola $a(\xi)$ whose zone-average is still equal to given a_j^n. For higher-order polynomial interpolation function like this, oscillations may appear near the discontinuity. One requirement

people usually placed on a numerical method is that it should be monotonicity preserving (van Leer 1979). $a(\xi)$ is constrained so that no new extrema appear in the interpolation function which do not already appear in the a_j^n's.

We can get the analytical solution to Eq. (1.1) with given data function $a(\xi)$,

$$a(\xi, t^n + \Delta t) = a(\xi - u\Delta t) \tag{8.5}$$

where the time Δt satisfies the CFL condition $c = u\Delta t / \Delta\xi \le 1$. Then we integrate this solution over each zone to obtain a_j^{n+1} ,

$$a_j^{n+1} = \frac{1}{\Delta\xi}\int_{\xi_{j-1/2}}^{\xi_{j+1/2}} a(\xi - u\Delta t)d\xi \tag{8.6}$$

The uniqueness of the PPM linear advection scheme is the choice and construction of the interpolation piecewise continuous parabola $a(\xi)$ in each zone,

$$a(\xi) = a_{L,j} + x(\Delta a_j + a_{6,j}(1 - x)) \tag{8.7}$$

where

$$x = \frac{\xi - \xi_{j-1/2}}{\Delta\xi} \; for \; \xi_{j-1/2} \le \xi \le \xi_{j+1/2},$$

$$\Delta a_j = a_{R,j} - a_{L,j}, \qquad a_{6,j} = 6(a_j^n - \frac{1}{2}(a_{L,j} + a_{R,j})) \tag{8.8}$$

$$a_{L,j} = \lim_{\xi \to \xi_{j-1/2}} a(\xi), \;\; a_{R,j} = \lim_{\xi \to \xi_{j+1/2}} a(\xi)$$

In smooth parts of the solution away from extrema, $a_{R,j} = a_{L,j+1} = a_{j+1/2}$. The calculation of $a_{j+1/2}$ is as following. Given zone average data a_j^n, we calculate the values of the indefinite integral $A(\xi) = \int^{\xi} a(\xi', t^n)d\xi'$ at zone edges:

$$A(\xi_{j+1/2}) = A_{j+1/2} = \sum_{k \le j} a_k^n \Delta\xi_k \tag{8.9}$$

We interpolate the quartic polynomial through the points $(A_{j+k+1/2}, \xi_{j+k+1/2}),\ k = 0, \pm 1, \pm 2$ and differentiate it to obtain $a_{j+1/2} = dA/d\xi\,|_{\xi_{j+1/2}}$. For uniform grids here, we have

$$a_{j+1/2} = \frac{7}{12}(a_j^n + a_{j+1}^n) - \frac{1}{12}(a_{j+2}^n + a_{j-1}^n) \tag{8.10}$$

Substituting these back to the analytical solution, we arrive

$$\begin{aligned} a_j^{n+1} &= \frac{1}{\Delta x}\int_{\xi_{j-1/2}}^{\xi_{j+1/2}} a(x - u\Delta t)dx \\ &= a_j^n + u\frac{\Delta t}{\Delta\xi}(f^a_{j-1/2,L}(u\Delta t) - f^a_{j+1/2,L}(u\Delta t)\,) \end{aligned} \tag{8.11}$$

Where the flux term

$$f^a_{j+1/2,L}(u\Delta t) = \frac{1}{u\Delta t}\int_{\xi_{j+1/2}-u\Delta t}^{\xi_{j+1/2}} a(\xi)d\xi \tag{8.12}$$

There is no explicit limiter used in PPM advection scheme. The monotonicity constraint is enforced by detecting these regions where the zone average value a is a local spatial extrema and resetting the value of a at either edges of the grid zone. It is hard to give the expression including this complex resetting given in Colella and Woodwad's paper (1984). However, away from these regions, we can obtain the local truncation error for the scheme,

$$\begin{aligned} L(\xi,t) &= (a_j^{n+1} - a_j^n) - c(f^a_{j-1/2,L}(u\Delta t) - f^a_{j+1/2,L}(u\Delta t)\,) \\ &= (a_j^{n+1} - a_j^n) - c\{a_{R,j-1} - \frac{c}{2}[\Delta a_{j-1} - (1-\frac{2c}{3})a_{6,j-1}]\} + c\{a_{R,j} - \frac{c}{2}[\Delta a_j - (1-\frac{2c}{3})a_{6,j}]\} \\ &= (a_j^{n+1} - a_j^n) - c(a_{j-1/2} - a_{j+1/2}) + \frac{c^2}{2}[(a_{R,j-1} - a_{L,j-1}) - (a_{R,j} - a_{L,j})] - \frac{c^2}{2}(1-\frac{2c}{3})(a_{6,j-1} - a_{6,j}) \\ &= (a_j^{n+1} - a_j^n) - c(a_{j-1/2} - a_{j+1/2}) + \frac{c^2}{2}[(a_{j-1/2} - a_{j-3/2}) - (a_{j+1/2} - a_{j-1/2})] \\ &\quad - \frac{c^2}{2}(1-\frac{2c}{3})[6(a_{j-1}^n - \frac{1}{2}(a_{j-3/2} + a_{j-1/2}) - 6(a_j^n - \frac{1}{2}(a_{j-1/2} + a_{j+1/2})] \\ &= \frac{c^2}{2}(\Delta\xi)^3(1-\frac{2c}{3})\,a_{\xi\xi\xi\xi} + \frac{c^2}{24}(\Delta\xi)^4(c^2+2c-5)\,a_{\xi\xi\xi\xi\xi} \end{aligned} \tag{8.13}$$

where $c = u\Delta t / \Delta\xi$ is the courant number. The third-order term causes the numerical dispersion, while the numerical diffusion arises from the fourth-order term. Though, monotonicity constraint may reduce the order of numerical scheme in the high-gradient region along the interface we used. This analysis is consistent with the numerical spreading rate scaling of a contact discontinuity layer width in PPM simulations, less than $t^{1/3}$ as in (Zabusky et al. 2003). Although mass diffusivity and viscosity (i.e. vorticity diffusivity) are both time-dependent, they should be approximately the same order. That is, the Schmidt number is the order of unity.

The extension of the algorithm to multi-dimension is applied using second-order Strang's operator splitting method.

There are very complex dissipation mechanisms in PPM: (1) flatten the interpolation profiles in the neighborhood of shocks where low amplitude post-shock oscillations may appear; (2) add an explicit diffusive flux to the numerical fluxes when flattering is not effective. Readers are referred to the original paper of Colella and Woodward. In short summary, the PPM dissipation consists of three parts: (1) complicated high-order truncation error terms; (2) nonlinear dissipation provided by the monotonicity constraint of van Leer, and (3) additional dissipation in the algorithm carefully added. This dissipation will be shown to play the same role as the subgrid model in large-eddy simulations in our mixing study in the following chapters.

For Godunov method and general hyperbolic conservation laws, we referred to Leveque (1992); for PPM algorithm, we turned to Colella and Woodward (1994).

To make tractable our long-time numerical simulations, we make a Galilean transformation of the fluid motion by adding the analytical one-dimensional shock-induced interface translation velocity so that the interface will stay in the reasonable-size computation domain. We have validated both analytically and numerically that the dynamics of fluid motions are Galilean invariant.

There are many effects that contribute to the dynamics in the time interval under study. We have chosen to focus on: the post-shock Atwood number A^*, post-shock perturbation

amplitude a_0^*, and ITL thickness δ_0. *A** is the most important dimensionless scaling parameter and we used the values from JK01 experiment. δ_0 and a_0^* are also obtained from JK01.

For computational simplicity and accuracy we use γ = 1.4 for both gases. We believe that the size of the ITL and the effect of resolution and order of accuracy are more important parameters than the small difference in gamma. There are many other important secondary parameters and the only way to resolve their impact is to perform a closely coupled experimental computational study, something we look forward to in the future.

C. Interface transition layer (ITL) and parameters

The functional form of the ITL used is motivated by molecular diffusion and we use the error function profile,

$$\rho = \frac{\rho_1 + \rho_2}{2}(1 + A erf(\sqrt{\pi} y / 2\delta_0)), \tag{8.14}$$

where ρ_2 is density of the bottom fluid, ρ_1 density of the preshock top fluid, $A = (\rho_2 - \rho_1)/(\rho_2 + \rho_1)$ is the preshock Atwood number, and $2\delta_0 = (\rho_2 - \rho_1)/(\partial\rho/\partial y)_{\max}$ the maximum slope interface thickness as shown in Figure 8.3(b). Note, as δ_0 approaches zero, the ITL becomes a contact discontinuity. We don't think the precise shape of these smooth profiles has much effect on the subsequent development of the instability because of the ITL compression by the shock.

As shown in Table 9.1, to facilitate comparison with the JK01 experiment, we use JK01 parameters to set up run 2, including Mach number *M*, post-shock Atwood number *A**, ITL thickness δ_0 and post-shock amplitude a_0^*. For scaling, we also do the simulations with other two Atwood numbers, A^* = 0.2 and 0.9, and keep all other *pre-shock* parameters fixed, e.g. the pre-shock amplitude a_0. All simulations are run up to t_{End} ~ $12\,t_M$. We normalize the time by t_M. In

Table 9.1, t_P is the time when amplitude growth rate $\dot{a}$ reaches the peak and starts to decay. It is used to divide the time interval for $\dot{a}$ scaling below.

Chapter 9

Vortex-Accelerated Vorticity Deposition: Verifications, Vortex Physics, and Amplitude Growth Rate

In the chapter, we study the vortex-accelerated secondary baroclinic vorticity deposition (VAVD) at late-intermediate times, and dynamics of sinusoidal single-mode Richtmyer–Meshkov interfaces in two dimensions. Euler simulations using a piecewise parabolic method are conducted for three post-shock Atwood numbers (A*), 0.2, 0.635, and 0.9, with Mach number (M) of 1.3. We initialize the sinusoidal interface with a slightly ‘‘diffuse’’ or small-but-finite thickness interfacial transition layer to facilitate comparison with experiment and avoid ill-posed phenomena associated with evolutions of an inviscid vortex sheet. The thickness of the interface is chosen so that there are no secondary structures along the interface prior to the multivalue time t_M, which is defined as the time when the extracted medial axis of an interfacial layer first becomes multivalued. For an interval of $11t_M$ beyond t_M, the simulations reveal nearly monotonic strong growth of both positive and negative baroclinic circulation in a vortex bilayer pattern inside the complex roll-up region. The circulations grow and secondary baroclinic circulation dominates at intermediate times, especially for higher A*. This vorticity deposition is due to misalignment of density gradient across the interface and vortex-centripetal acceleration ~secondary baroclinic!, and enhanced by the intensification of interfacial density gradient arising from the vortex-induced strain. Our simulation results for A*50.635 agree with the recent air–sulfur hexafluoride (SF6) experiment of Jacobs and Krivets (2001), including several large-scale features of the evolving mushroom structure: The usual interface spike-bubble amplitude growth rate $\dot{a}$ and the dimensions of the spike roll-up cavity. VAVD plays an important role in the intermediate time

dynamics of the interfaces. Our amplitude growth rate disagrees with the $O(t^{-1})$ result of Sadot et al. Instead, it approaches a constant which increases with A*(<0.9). An adjusting periodic single point vortex model which uses the calculated net circulation magnitude and its location, gives excellent results for the amplitude growth rates to late-intermediate times at low Atwood numbers (A* =0.2,0.635). The evolution of enstrophy, vorticity skewness, and flatness are quantified for the entire run duration, and one-dimensional averaged kinetic-energy spectra are presented at several times.

The VAVD, a self-driven process, is the fundamental mechanism how the interface forms complex spiral mushroom structures that eventually lead to turbulent mixing. This part of work is published in the Physics of Fluids (Peng et al, 2003b).

9.1 Validations and Verifications

In this section, we use an interface transition layer (ITL) as shown in Figure 8.3 in chapter 8 to model the Jacobs and Krivets 2001 (JK01) air/SF_6 experiment and emphasize juxtaposition of numerical simulation and experimental results including large and intermediate scale structures, small-scale sensitivity, and amplitude growth $a(t)$. This serves the validation and verification purpose. In Sec. 9.2 offers the discussion of the importance and physics of vortex accelerated vorticity deposition (VAVD) and density gradient intensification process; in Sec 9.3 the VAVD process' impact on the amplitude growth rate is examined.

We use a post-shock Atwood number A^* = 0.635 corresponding to a density ratio of 4.52 (run #2) as shown in Table 9.1. Note, this density ratio reduction from normal SF_6/air results from the presence of acetone which is added to the ambient air to enhance the PLIF visualization, as discussed in JK01. The ITL thickness to wavelength ratio is less than 10% initially and becomes even smaller after the shock hits the interface. The precise density ratio and ITL thickness for the experiment depends on the time duration for preparing the initial state and the diffusion coefficients of acetone and air in SF_6. Furthermore, the PLIF images visualize a nonlinear combination of density and temperature. Care must be exercised when comparing juxtaposed

images of PLIF and density, and code validation studies must take these phenomena into account, especially when complex roll-ups occur.

	A^*	M_s	a_0 / λ	a_0^* / λ	δ_0 / a_0^*	t_P / t_M	t_{End} / t_M
*run*1	0.2	1.3	0.04	0.031	1.152	0.2	12
*run*2	0.635	1.3	0.04	0.0368	1.152	0.19	12
*run*3	0.9	1.3	0.04	0.038	1.152	0.39	11.8
*JK*01	0.635	1.3	/	0.0368	1.152	/	5.12

Table 9.1 Parameters for the shock diffuse sinusoidal interface. Here A^* is the post-shock Atwood number, M_s Mach number, λ wavelength, a_0 preshock amplitude, a_0^* postshock amplitude, δ_0 half maximum slope interface thickness, t_P is the time when the amplitude growth rate reaches the peak value, t_M is the time when the interface first becomes multi-valued, and t_{End} is the end time of numerical simulations. Numerical resolution in all runs is 360 (λ) $\times$ 2520.

The evolution of the single-mode interface, from both simulation and experiment, is juxtaposed in Figure 9.1. In Figures 9.1(a)-(g), the left columns are the simulation density images, and the right columns are the PLIF images. Note for the PLIF images, only the right two thirds of the shock tube is shown. The heavy SF_6 and light air are shown as dark and light, respectively. At t / t_M = 0.035, just after the shock passage, the ITL thickness has been greatly reduced and primary vorticity is baroclinically deposited on it. Vorticity is localized and the interface forms the well-known mushroom structure at t / t_M = 1.96. As the ITL continues to roll up, the mushroom structure expands in spanwise direction and is elongated in streamwise direction. Secondary rollups are observed inside the main mushroom spirals and there is qualitative agreement between simulation and experiment. This roll-up mechanism causes the transfer of energy from large-scale structures to smaller and smaller scale structures and enhances the mixing. This secondary instability is caused by VAVD, as discussed below in Sec. 9.2.

Extracted amplitude growth $a(t)$ of density is compared with PLIF measurements in Figure 9.2. The amplitude is corrected by the post-shock amplitude a_0^* and normalized by wave number k. Note, each PLIF measurement is obtained from a PLIF image of a different experiment. The simulation is of much longer duration than the experiment. The simulation amplitudes are smaller than those from PLIF during the last one third of the experimental period when the data becomes noisier. Especially, a rather rapid growth of amplitude is observed for the PLIF images from Figure 9.1(f) to 9.1(g): $k(a-a_0^*)$ increases by 0.43 from Figure 9.1 (e) to 9.1 (f) within the interval, $\Delta t / t_M = 0.87$; and by 0.48 from Figure 9.1 (f) to 9.1 (g) within the interval, $\Delta t / t_M = 0.79$. That is, the amplitude grows faster in the latter period. This behavior is inconsistent with the well-known decaying trend of the amplitude growth rate. It is probably due to 3D or boundary effects as observed in the experiment.

9.2 VAVD and Density Gradient Intensification

In this section we observe and quantify the rapid growth of positive and negative circulation on the ITL after the first roll-up, $t \sim 2t_M$. We show that this leads to a *constant* amplitude growth rate at late-intermediate times which increases with A^*, as discussed in chapter 10. Furthermore, these large circulations represent close-lying VBL's and are believed to be the mechanism triggering a secondary instability and enhanced turbulent mixing.

The evolution of the vorticity in our Euler simulations is governed by,

$$\frac{\partial \omega}{\partial t} + \mathbf{u} \bullet \nabla \omega = \omega(\nabla \bullet \mathbf{u}) + \frac{1}{\rho^2} \nabla \rho \times \nabla p. \qquad (9.1)$$

We focus on the effect of the baroclinic vorticity term, $\nabla p \times \nabla \rho$. In Figure 9.3, we compare our density (A^* = 0.635 in Figure 9.2) and vorticity evolutions. In the latter, the dark and bright colors are for negative and positive vorticity, respectively. We discuss only the right half of our

symmetric images, where the primary shock deposited negative vorticity. Here, as in previous work (Peng et al 2003a), we use a “diagnostic box” for extracting circulation. In Figure 9.3 this corresponds to a rectangular domain with vertical edges and horizontal edges through the spike and bubble tips.

In Figure 9.4 we present the primary and secondary circulations into intermediate times. Figure 9.5 has excellent agreement of circulations with analytical calculations of Samtaney and Zabusky (1994). The circulation value for comparison is obtained by integrating the y-integrated vorticity just after shock passage. The result in Figure 9.5 implies that circulation model of Samtaney and Zabusky (1994) is valid for the shock small-but-finite thickness ITL interactions as well.

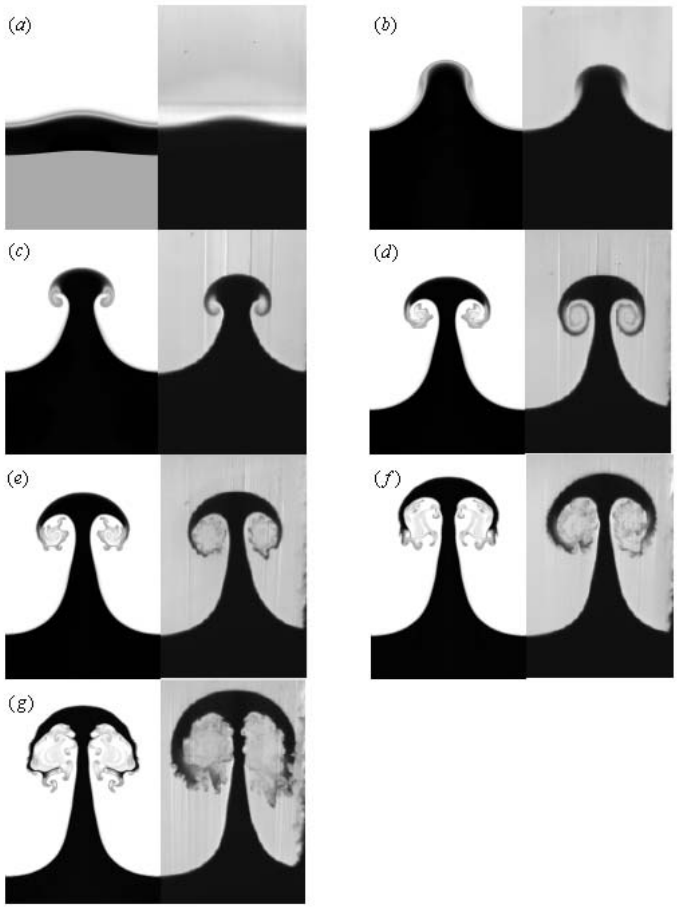

Figure 9.1 Density images (left) from numerical simulations (A^*=0.635) juxtaposed with those of Jacob & Krivets’ PLIF experimental visualization (right) at normalized times t / t_M : (a) 0.035, (b) 1.0, (c) 1.96, (d) 3.02, (e) 3.46, (f) 4.33, and (g) 5.12

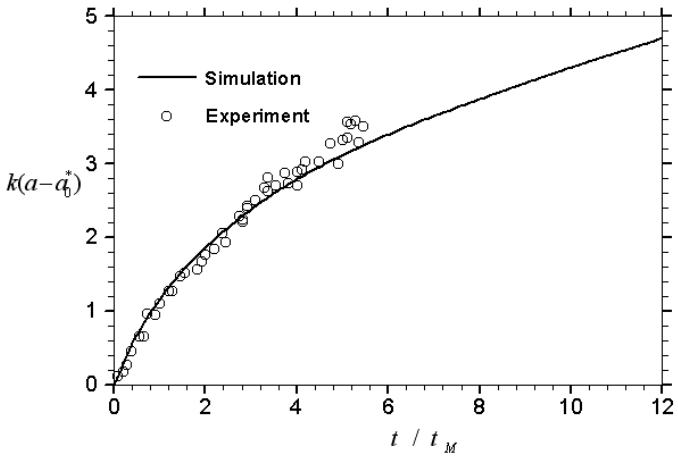

Figure 9.2 Comparison of dimensionless extracted perturbation amplitude growth from current simulation $A^* = 0.635$ with experimental PLIF amplitude measurements of Jacobs and Krivets (2001).

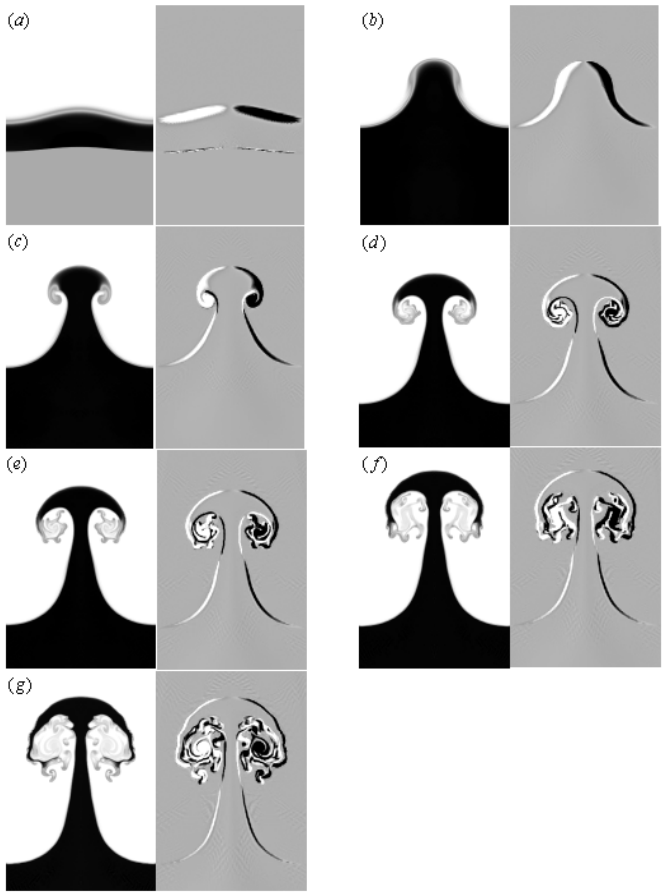

Figure 9.3 Vorticity and density juxtaposition from numerical simulations at normalized times t / t_M : (a) 0.035, (b) 1.0, (c) 1.96, (d) 3.02, (e) 3.46, (f) 4.33, and (g) 5.12.

Soon after the shock passage, the fluid motion becomes nearly incompressible as demonstrated by Kotelnikov *et al* (2000), and Meiron and Meloon (1997). The evolution of the vorticity in Eq. (9.1) is governed the misalignment of the gradient of pressure or acceleration and gradient of density, $\nabla p \times \nabla \rho \sim -d\mathbf{u}/dt \times \nabla \rho$. The only acceleration available is *centripetal* and towards the core center and arises from the large-scale rotation of the coherent vortices, which are the rollups formed from the advection and compression of the deposited primary vorticity. The direction of density gradient depends on the evolution of the rolled-up ITL. We call this mechanism a *vortex-accelerated secondary baroclinic vorticity deposition* (VAVD) and illustrate it qualitatively in Figure 9.6 for our air/SF_6 simulations just after the formation of the first rollup.

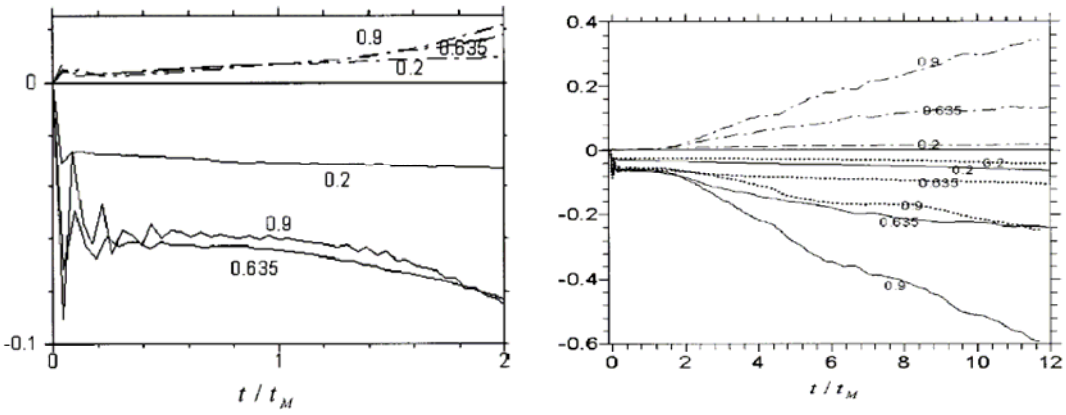

Figure 9.4 Positive, negative and total circulation inside a diagnostic box enclosing the mixing zones: dash-dotted lines for positive circulations, solid lines for negative circulation, and dotted line for total circulations. The corresponding post-shock Atwood numbers are labeled on the lines. (a, left) primary circulations; (b, right) primary and secondary circulations.

The arrangement of the density gradient field shows that opposite-signed vorticity is generated to the left and right of the core, at the neck and outermost point, respectively. That is, the positive secondary vorticity generated first cancels the primary negative vorticity there and forms a vortex bilayer together with the outer-point enhanced negative vortex layer. These opposite sign vorticities are advected into the vortex core as the fluid is entrained there, and

greatly enhance the mixing. This mechanism reminds us of the mixing enhancement resulting from reshock of an interface, where opposite sign vorticity are generated by the oppositely-directed acceleration (Kotelnikov et al. 2000). A similar sketch arises when considering slow/fast Richtmyer-Meshkov environments.

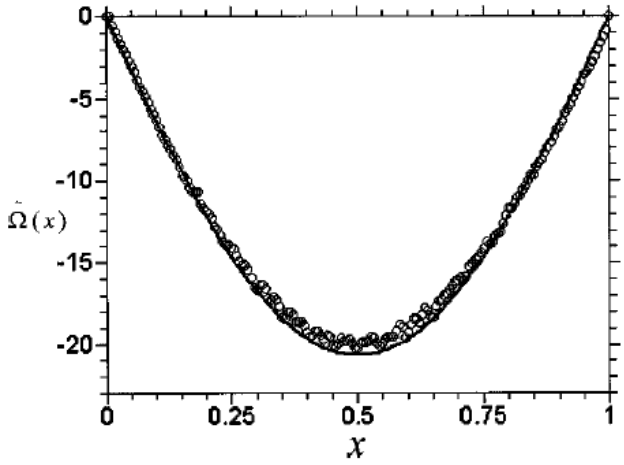

Figure 9.5 Distribution of the y-integrated vorticity $\tilde{\Omega}(x) = \int_D \omega(x, y)dy$ for the A* = 0.635 interface just after the shock passes the ITL. The solid line is the analytical result given by Samtaney and Zabusky (1994). The circle symbols are the simulation data corresponding to $\tilde{\Omega}(x)$.

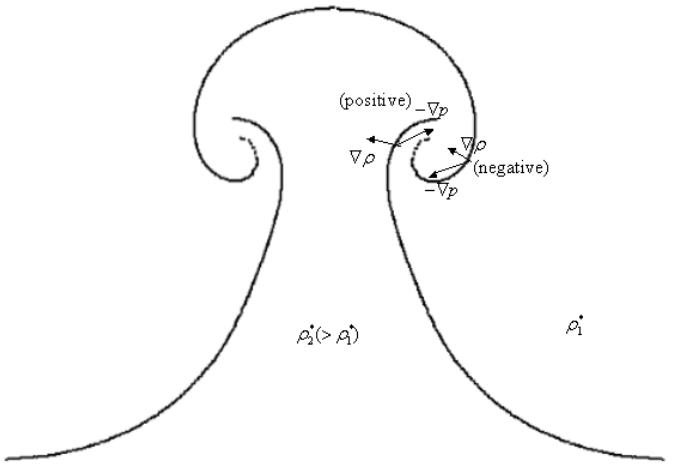

Figure 9.6 Illustration of the vortex-accelerated baroclinic secondary vorticity deposition for the fast/slow RM interface instability. The background curve is the extracted interface (using zero crossing of Laplacian density algorithm) at t / t_M = 1.96 for $A^* = 0.635$.

We have discussed the direction of density gradient and corresponding signs of vorticity and now we discuss the important aspect of growth of the density gradient magnitude, $|\nabla\rho|$, as induced by the *strain* from the "complex" mushroom vortex dipole or VP. Soteriou and Ghoniem (1995), while presenting their incompressible Lagrangian transport-element method, discussed the increase of $|\nabla\rho|$. For our compressible environment, the evolution equation is

$$\begin{aligned}\frac{d\nabla\rho}{dt} &= -\rho\nabla(\nabla\bullet\mathbf{u}) - \nabla\rho(\nabla\bullet\mathbf{u}) - (\nabla\rho\bullet\nabla)\mathbf{u} - \nabla\rho\times(\nabla\times\mathbf{u}) \\ &= -\rho\nabla(\nabla\bullet\mathbf{u}) - \nabla\rho(\nabla\bullet\mathbf{u}) - \nabla\rho\bullet(\nabla\mathbf{u})_s, \end{aligned} \tag{9.2}$$

where $(\nabla\mathbf{u})_s$ is the symmetric part of the velocity gradient tensor. However, as we explained above, after shock passage the fluid becomes nearly incompressible and Eq. (9.2) reduces to

$$\frac{d\nabla\rho}{dt} = -\nabla\rho\bullet(\nabla\mathbf{u})_s, \tag{9.3}$$

also obtained by Soteriou and Ghoniem. Another view is to consider the material line d**l** and the evolution of $(|\nabla\rho|/|\mathrm{d}\mathbf{l}|)$, where $\nabla\rho\bullet\mathrm{d}\mathbf{l}=0$. The evolution of d**l** is governed by $d(\mathrm{d}\mathbf{l})/dt = \mathrm{d}\mathbf{l}\bullet\nabla\mathbf{u}$ and we obtain

$$\frac{d}{dt}\left(\frac{|\nabla\rho|}{|\mathrm{d}\mathbf{l}|}\right) = 0, \tag{9.4}$$

where we have used $\mathbf{t}\bullet\nabla\mathbf{u}\bullet\mathbf{t} = -\mathbf{n}\bullet\nabla\mathbf{u}\bullet\mathbf{n}$ for incompressible flows and **t** and **n** are the tangential and normal unit vectors to the material line d**l**. Eq. (9.4) indicates that if |d**l**| is increased so is the density gradient magnitude, a phenomenon present in our simulations as shown in Figure 9.7. Here histograms of the magnitude of the normalized density gradient, $|\nabla\rho|/|\nabla\rho|_{0,\max}$, are shown inside the diagnostic box and $|\nabla\rho|_{0,\max}$ stands for the preshock initial maximum magnitude of the gradient of density. Initially, the highest density gradient magnitude $|\nabla\rho|_{\max}$

of the ITL moves toward that provided by the grid resolution. Then, as the length of the medial axis of the ITL grows, so does the corresponding number of points at $|\nabla\rho|/|\nabla\rho|_{0,\max}=1.0$, and the number is proportional to $(|\nabla\rho|/|\nabla\rho|_{0,\max})^{-q}$, where the exponent q is about 1.0 for the times beyond t_M. We also observe at t/t_M = 12.0, the curve has a break and we are uncertain if that is real or a numerical artifact. Therefore, density gradient intensification enhances the VAVD. However, the saturation of the $|\nabla\rho|_{\max}$ will cause the slowing of the growth of the total circulation and its eventual saturation.

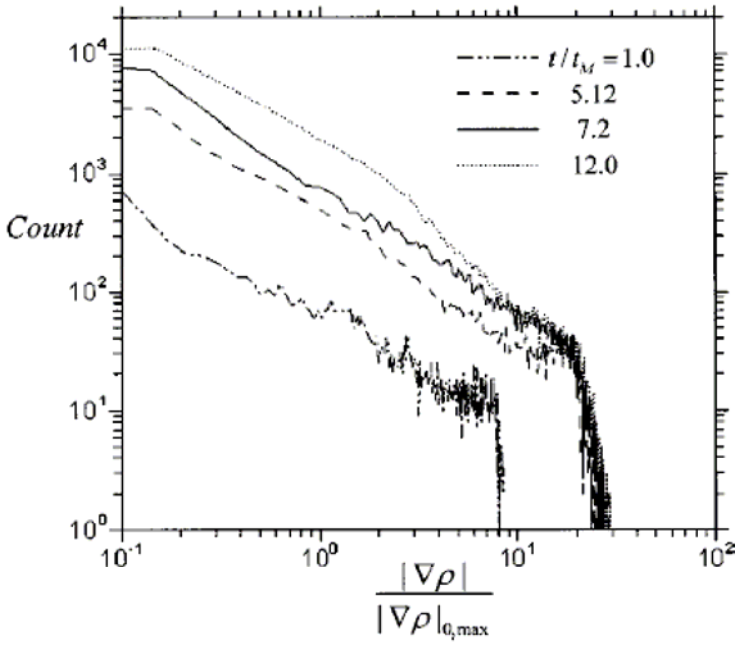

Figure 9.7 Density gradient magnitude (normalized by the preshock initial maximum density gradient magnitude) distribution for $A^*=0.635$ at times t/t_M = 1.0, 5.12, 7.2 and 12.

One comment about the smoothness of the neck region as manifest in the density and vorticity in Figures. 9.3 (a) –(e). Although $|\nabla\rho|$ is intensified and results in a reduced ITL thickness, we believe that the stretching environment stabilizes the interface (Dritschel et al, 1991) until it is impacted directly by the rolled up small-scale secondary structures seen in Figures. 9.3(f) and (g).

The VAVD process and VBL formation are also observed in other stratified or inhomogeneous flows. In 2D stratified mixing *layers* simulations, Soteriou and Ghoniem (1995), Staquet (1995), and Reinaud *et al.* (2000) separately reported local vorticity deposition and a rapid growth of positive and negative circulation. Note, Staquet studied the secondary instability from the vortex point view. Hou *et al.* reported a rapid secondary vorticity deposition in their stratified incompressible vortex sheet interface simulation with surface tension.

9.3 Amplitude Growth Rate

The amplitude growth rate $\dot{a}(t)$ for a single-mode 2D Richtmyer-Meshkov interface is usually scaled to vary as a power law of the time after the shock passage,

$$\dot{a}(t) \propto t^{-p}. \tag{9.5}$$

As briefly reviewed in Sec. I, the scaling exponent p is still controversial. Two recent experiments for a single-mode air/SF_6 interface by Prasad *et al* (2000) and JK01 provide data up to intermediate times. Our numerical simulations (Zabusky *et al. 2003a*) to early-intermediate times obtained p = 0.683 which agreed very well with Prasad *et al.* experimental data fitting range, $0.67 \le p \le 0.74$. These exponents are obviously smaller than the p =1 law of Sadot *et al* (1998). JK01 juxtaposed their amplitude measurements with two nonlinear theories, Zhang and Sohn (1997)and Sadot *et al (1998)*. JK01 found better agreement with the smaller exponent p =1 of the latter than p =2 for A^* = 0.635 given by Zhang and Sohn (1997). However, our data, which are excellent agreement with experimental data, as presented in Figure 9.1, give p <1 in this time interval.

Beyond this time the *VAVD* phenomena greatly modify the behavior of the mixing zone as shown at $t/t_M = 7.2$ and $t/t_M = 12$ (the end of our simulations) in Figure 9.8. In a true experiment, viscous, 3D and boundary effects will begin to play roles. Thus, the pre-turbulent and

mixing details in Figure 9.8 of vortex interactions, merger, and VP formation are only heuristic. This indicates some of the reasons why our single line vortex model, presented below, yields poor results beyond the intermediate time. For scaling, we also did Richtmyer-Meshkov interface simulations with A^* = 0.2 and 0.9. We present the simulation amplitude $a(t)$ and its growth rate $\dot{a}(t)$ in Figures. 9.9 (a) and (b), respectively. The amplitude growth rate $\dot{a}$ in Figure 9.9(b) shows the well-known phenomena of rapid growth to a maximum for t/t_M << 1, followed by a power law decay for a time range that depends on Atwood number and finally a saturation at a near-constant value, a result not previously known, although conjectured by Zabusky (1999) (see Sec. 6.2 there). Note that for t/t_M < 1, the curves are not nested and the A^* = 0.9 curve saturates at a lower magnitude than the A^*=0.635 curve. This results from the behavior of the total circulation at early time as shown in Figure 9.4 and discussed above. Similarly, beyond t/t_M =2, the $\dot{a}$ curves are again nested, but the A^* = 0.9 curve takes longer to reach a near-constant value.

We now digress briefly to explain the confusion in exponents presented in the literature and discussed briefly above, viz. they depend on the range of the data that were fitted as well as the quality of the experiment at these times. In Figures 9.10 a-c, we present our $\dot{a}$ for A^* = 0.2, 0.635 and 0.9, respectively. Here three power fittings and the result from an adjusting single point vortex model are compared with the simulation.

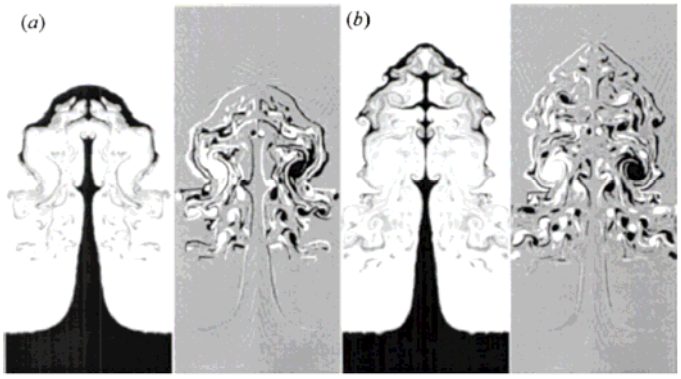

Figure 9.8 Density (left) and vorticity (right) from A^* = 0.635 simulation at t/t_M = 7.2(a) and 12(b)

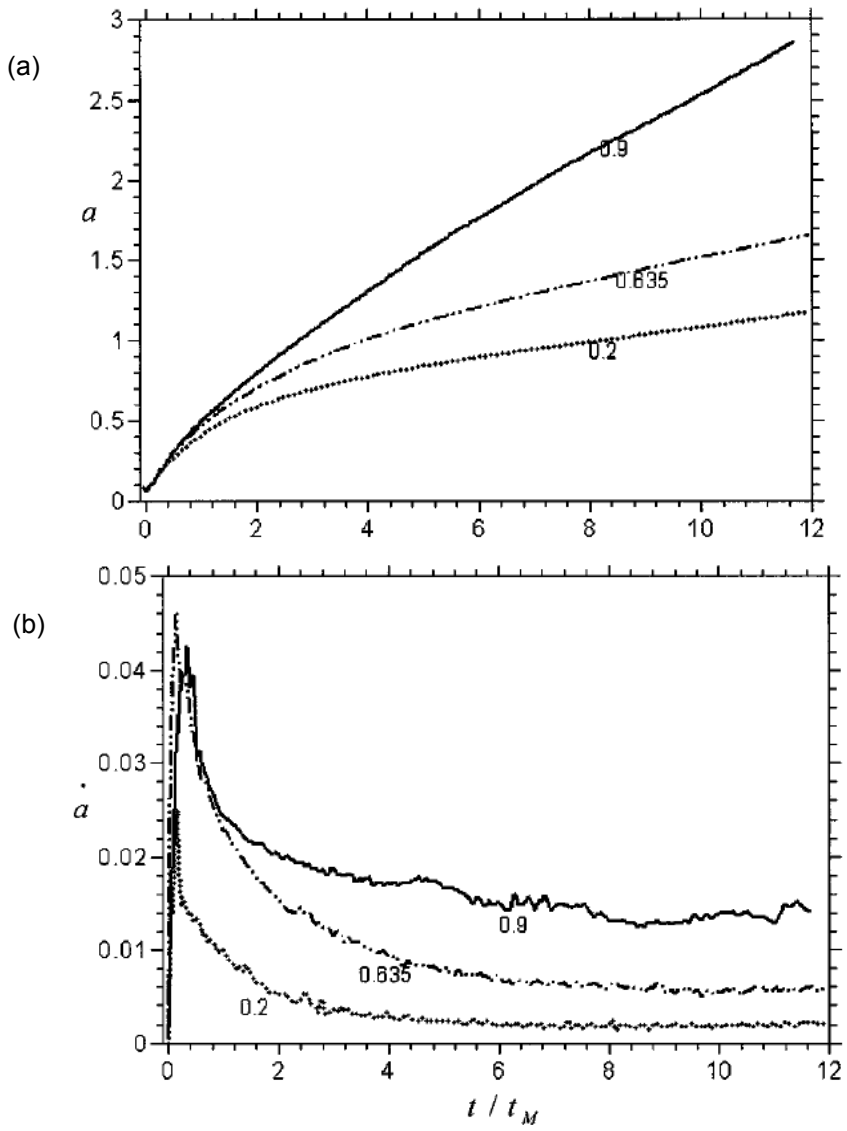

Figure 9.9 (a) Juxtaposition of the amplitude evolution $a\,(t)$ for A* = 0.2, 0.635 and 0.9; (b) Juxtaposition of the amplitude growth rates for A* = 0.2, 0.635 and 0.9.

(a)

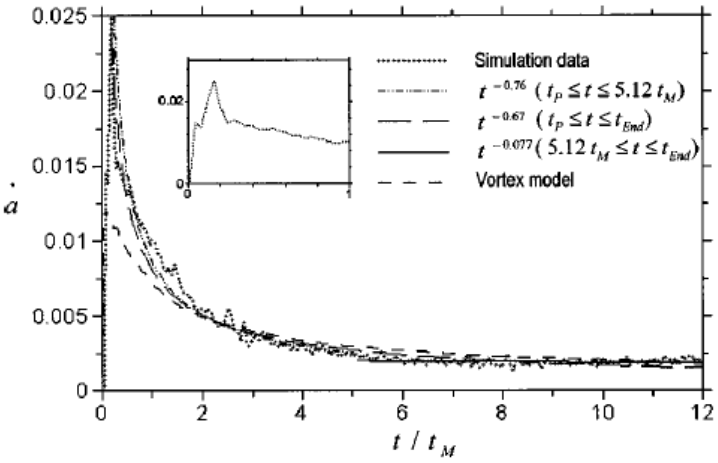

(b)

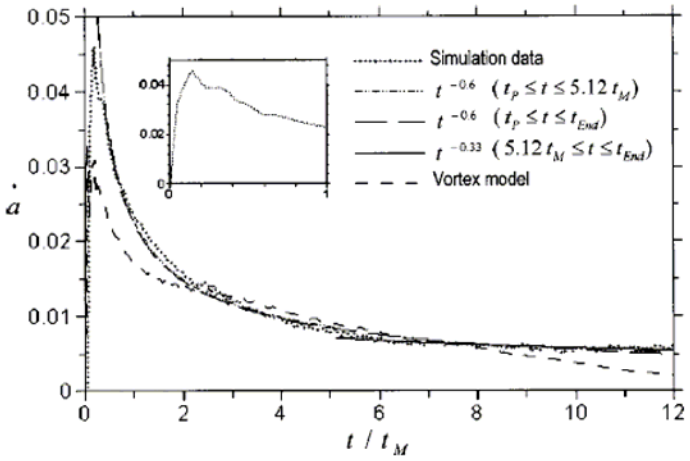

(c)

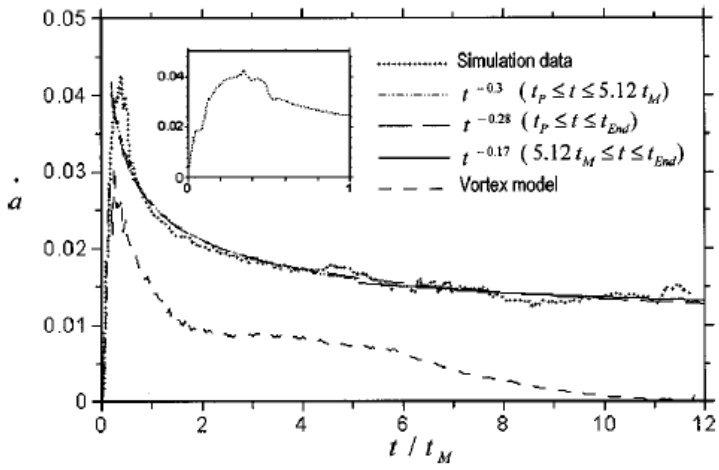

Figure 9.10 Amplitude growth rate $\dot{a}$ from the $A^* = 0.2$ (a), $A^* = 0.635$ (b) $A^* = 0.9$ (c) simulation, adjusting periodic single point vortex model and three power fittings in three ranges: $t_P \le t \le 5.12\,t_M$, $t_P \le t \le t_{End}$ and $5.12\,t_M < t \le t_{End}$.

We identify several critical times: t_P when the $\dot{a}$ reaches the initial peak, t_M the multivalue time discussed in chapter 8, $5.12t_M$ around which most simulations and experiments end, and t_{End} ~ $12\,t_M$ the end time of our simulations. The corresponding intervals are $0 \le t \le t_P$, $t_P \le t \le 5.12t_M$ and $5.12t_M \le t \le t_{End}$, where the first stage is a compressible phase and approximately described by linear theory. Consider A^* = 0.2 in Figure 9.10a, and the ranges $t_P \le t \le 5.12t_M$, $t_P \le t \le t_{End}$, $5.12t_M \le t \le t_{End}$. The exponents are p_1 = 0.76, p_2 =0 .67 and p_3 = 0.077, respectively. They decrease monotonically because $\dot{a}$ is saturating to a near-constant value as shown by the fitting $\dot{a} \sim 0.0021 + 2.1\times10^{-6}(t - 5.12t_M)^{-1}$. The very small coefficient of the second term indicates that the late-intermediate time $\dot{a}$ approaches a constant. Similar results are obtained in Figures 9.10 b-c.

A model using a single point dipole-vortex in a periodic domain has been suggested to describe aspects of the RM $\dot{a}$ after shock passage, e.g. Zabusky *et al.* (1995) and Jacobs and Sheeley (1996). The former suggested a partially adjusting circulation model up to intermediate times and the latter used a fixed circulation model for a similar time interval. In Figures. 9.10 a-c, we include graphs of $\dot{a}$ from a more complete adjusting periodic point vortex model (as described in Appendix B of Peng, Zhang, Zabusky 2003),

$$\dot{a}_{vortex} = -\frac{k\Gamma \sin kx_c}{4\pi}\left(\frac{1}{\cosh(kd_s) - \cos kx_c} + \frac{1}{\cosh(kd_b) + \cos kx_c}\right). \qquad (9.6)$$

where Γ is the time-varying net circulation, x_c is the x coordinate of the centroid of vorticity field of the right half of the spike-bubble mushroom and illustrated in Figure 9.12 (with an inset sketch of the vortex mushroom), d_s and d_b are obtained from the y coordinate of the centroid of vorticity field and the location of the evolving spike and bubble tips.

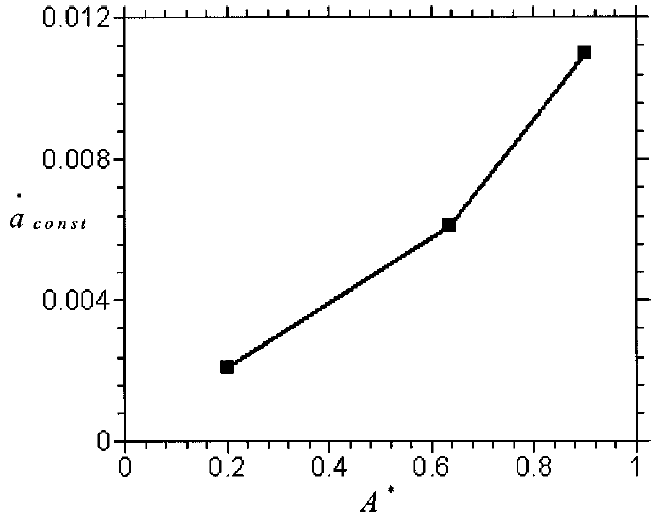

Figure 9.11 Scaling of the constant amplitude growth rate $\dot{a}_{const.}$ with post-shock Atwood number A*.

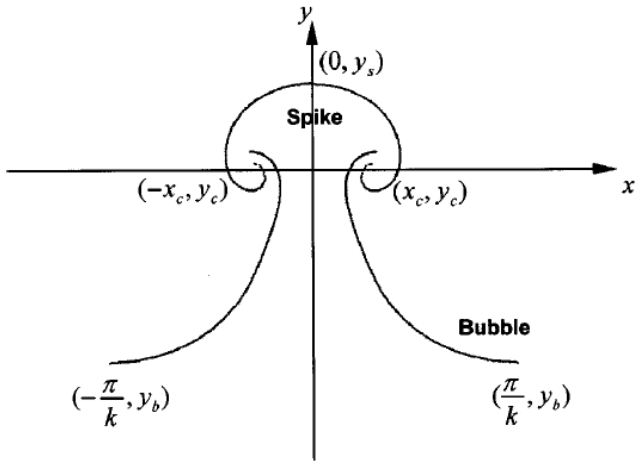

Figure 9.12. The evolution of the x-coordinate of the vorticity field centroid for A^* = 0.2, 0.635 and 0.9. Inset: sketch of the spike-bubble mushroom vortex.

For A^* = 0.2, the vortex model gives very good results for $2 \leq t/t_M \leq 12$ because of the compact rolled up simulation result. The lower limit of the interval arises because the vorticity

must localize before the model becomes adequate. For A^* = 0.635, we have the same lower limit and an upper limit of t/t_M = 8, because of the formation of a complex VP.

For A^* = 0.9, the model results differ from the simulation because of the spreading of the circulation over a large amplitude and the location of the centroid near to the y-axis. Thus we conclude that the point vortex model is inadequate for larger Atwood numbers. Actually, for finite Reynolds numbers and beyond intermediate times and for large Atwood numbers and Mach numbers the modeling of vortex accelerated flows by one or more point vortices is a relatively untouched subject!

The approach to a constant $\dot{a}_{const.}$ is the result of the formation of a complex vortex projectile with increasing *net* circulation due to the vortex accelerated vorticity deposition (VAVD), at and beyond late-intermediate times, as shown in Figure 9.4. We also note that final net circulations and $\dot{a}_{const.}$ scale monotonically with A^*. Figure 9.11 shows $\dot{a}_{const.}$ scaling with A^*. The continued linear growth of circulation for A^* = 0.9 (see Figure 9.4) cause a larger increment in $\dot{a}_{const.}$ than between A^* = 0.2 and 0.635. These curious phenomena at large A^* require a careful study and should be done as A^* approaches 1.0 and include higher Mach numbers.

9.4. Numerical Dissipation and Transition to Turbulence

A. Numerical dissipation

As we can see in Figures. 9.3 and 9.8, both heavy and light gases are entrained into the complex roll-up regions and mixed there. Although our Euler solver has no physical viscosity, the PPM algorithm does include small-scale numerical dissipation. This dissipation consists of three parts: (1) complicated high-order truncation error terms; (2) nonlinear dissipation provided by the monotonicity constraint of van Leer (1979), and (3) additional “flattening” dissipation included in the original paper by Colella and Woodward (1984). Note that there are very small-scale “chaotic” effects which cause complex flows within vortex cores at late times for the simple

2D roll–up of dipolar sheets (Krasny and Nitsche 2002). Also Youngs (1991) and others have shown that this dissipation may play the same role as a subgrid scale model in large-eddy simulations.

The effective viscosity for the PPM code that we used was found to be very small. Their long-time 2D curtain simulations showed enstrophy growth, saturation and finally decay. Our results are for a shorter times so that the enstrophy in all cases grows and saturates.

B. Enstrophy, flatness, and skewness factors

In Figures. 9.13 a-b, we show moments of vorticity related to turbulent behavior $<\omega^2>,<\omega^3>$ and $<\omega^4>$, where the first is the enstrophy (without ½) and the others are skewness and flatness. The skewness and flatness factors are defined as

$$s(t)=\frac{<\omega^3>}{<\omega^2>^{3/2}},\quad f(t)=\frac{<\omega^4>}{<\omega^2>^2}. \tag{9.7}$$

Figure 9.13a shows a sharp increase of enstrophy due to primary vorticity deposition for higher Atwood numbers. A very long plateau of enstrophy is observed for all Atwood numbers, which implies that the baroclinic forcing is strong enough to overcome the enstrophy dissipation even at the end of our simulations. However, when the fluid becomes more turbulent, dissipation will eventually dominate the secondary baroclinic forcing.

In Figure 9.13b, we plot the *normalized* skewness and flatness factors for A^* = 0.635 and 0.9. Both factors increase rapidly to a maximum in the pre-turbulent epoch and then decrease as a near power law to near stationary values. Realistically, all these moments depend critically on three dimensional and true viscous effects and we do not trust our solutions at the largest times.

C. Spectral analysis

The late-intermediate time stage of the RM instability is characterized by a large range of scales spanning from the size of the domain to the mesh size. We present spectra analysis on the flow. As we know, the flow is anisotropic and inhomogeneous especially in the direction of the incident planar shock. Fourier transformation can't be applied in this streamwise direction. Instead, we consider the one-dimensional averaged transversal kinetic energy spectrum of $\Xi(x,y,t)=\sqrt{\rho}\ \mathrm{v}$ suggested by Lesieur *et al.* (1988),

$$E_1(k_x,t)=\frac{1}{2d}\int_{-L}^{L}|\hat{\Xi}(k_x,y,t)|^2 dy, \tag{9.8}$$

where $\hat{\Xi}(k_x,y,t)$ is the longitudinal Fourier transform of $\Xi(x,y,t)=\sqrt{\rho}\ \mathrm{v}$ at a given y,

$$\hat{\Xi}(k_x,y,t)=\frac{1}{\lambda}\int_0^{\lambda}\sqrt{\rho}\mathrm{v}(x,y,t)\exp(-ik_x x)dx \tag{9.9}$$

There $2L=d_s+d_b$ is the width of the diagnostic box surrounding the mixing zone at the end time of the simulations. The inertial range spectrum $k_x^{-\alpha}$ of this spectrum will give the same exponent as $k^{-\alpha}$ $(k=\sqrt{k_x^2+k_y^2})$ of the total kinetic energy spectrum for a two-dimensional homogeneous isotropic turbulence.

Figure 9.14 shows the one-dimensional averaged transversal kinetic energy spectrum $E_1(k_x)$ at three times t/t_M = 1, 9 and 12 with the k_x^{-3} cascade conjectured by Kraichnan (1967) for 2D homogeneous turbulence. The high wave number spectrum tail is governed by numerical dissipation. The late-intermediate time stage of the 2D flows is still dominated by the large to intermediate scale coherent vortex structures.

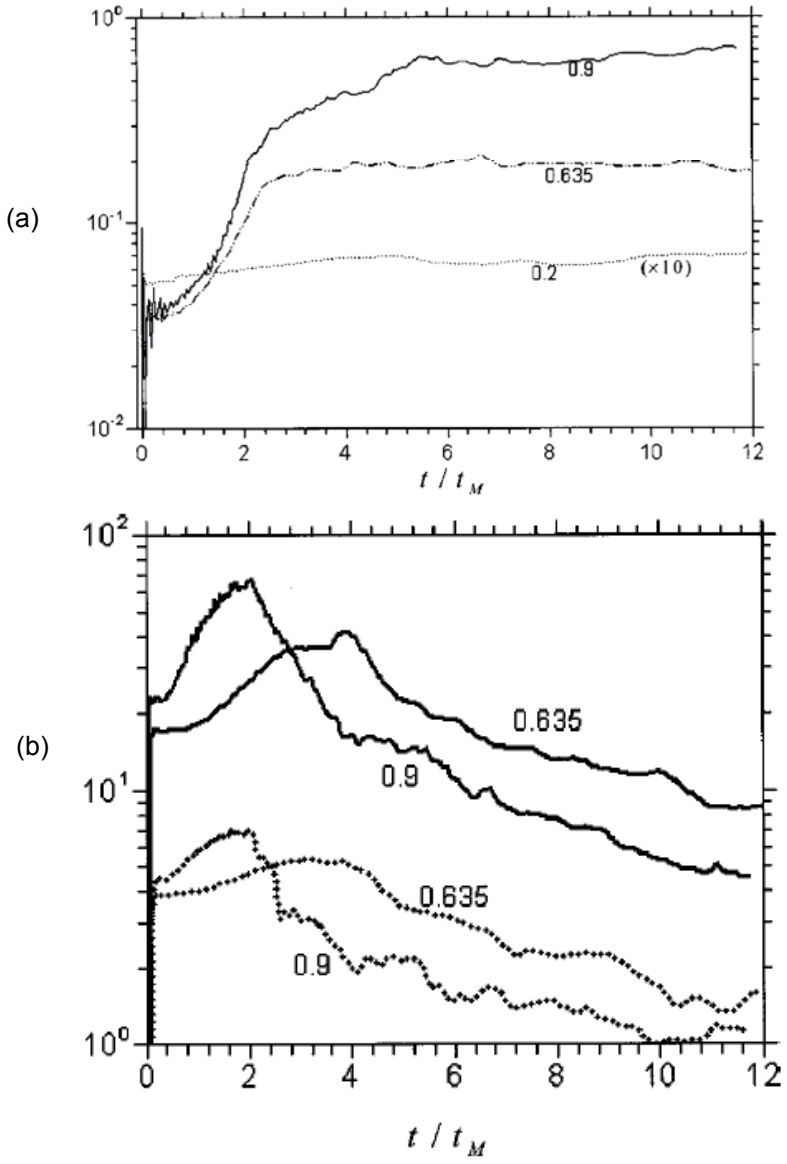

Figure 9.13 (a) Enstrophy inside the diagnostic box enclosing the mixing zones $\iint_D \omega^2 dxdy$: solid lines for $A^* = 0.9$, dash-2doted lines for $A^* = 0.635$, and dotted line for $A^* = 0.2$ (multiplied by 10 as indicated). The corresponding post-shock Atwood numbers are labeled on the lines; (b) Evolution of vorticity flatness and skewness factors for A^* = 0.635 and 0.9. Dotted lines are $-<\omega^3>/<\omega^2>^{3/2}$, and solid lines are $<\omega^4>/<\omega^2>^2$.

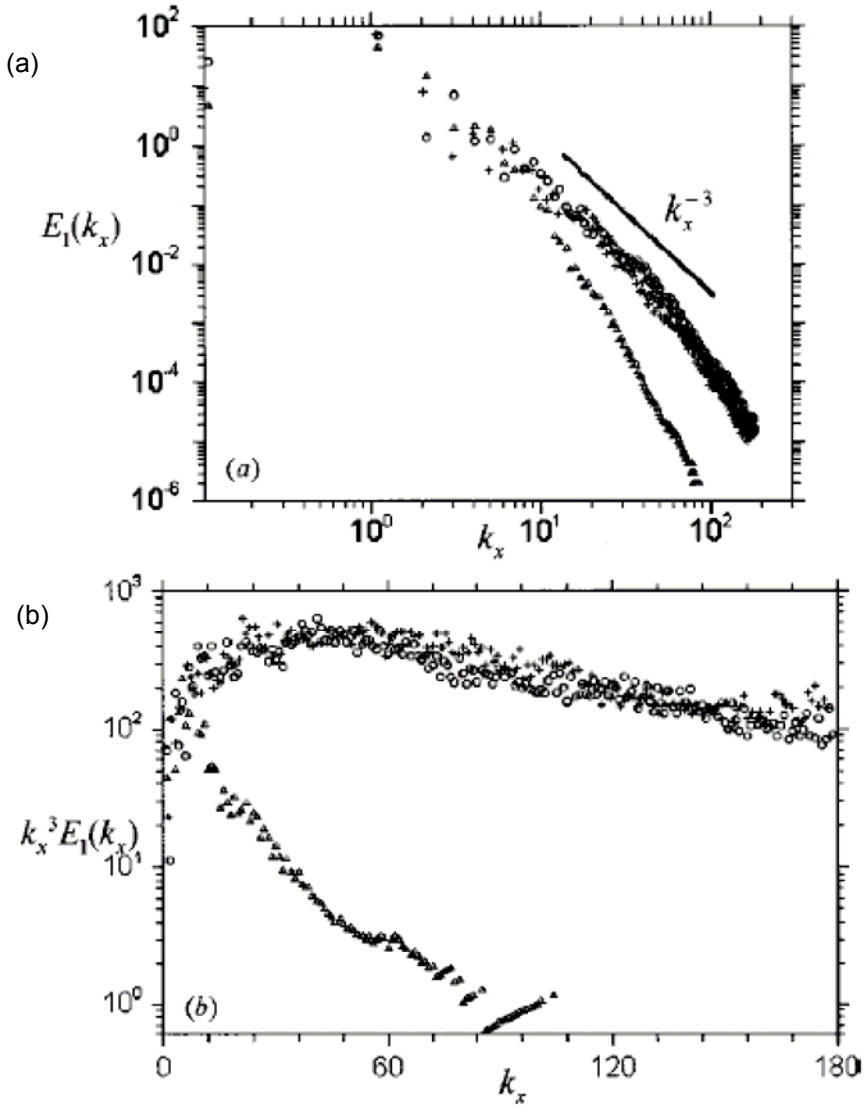

Figure 9.14 One-dimensional averaged transversal kinetic energy spectrum for *A** = 0.635 case at t/t_M = 1.27("ΔΔΔΔ"), 12.1("+++") and 16.5 ("○○○○") with k_x^{-3} spectrum shown as the solid line; (b) corresponding compensated spectrum.

Chapter 10

Circulation Rate of Change

In this chapter, we derive and validate a new diagnostic formula for determining the rate-of-change of total circulation, $\dot{\Gamma}_D$, within specified accelerated RM interfacial domains. With an initially finite-width interfacial transition layer (ITL), M=1.3 and various post-shock Atwood numbers, $0.2 \le A^* \le 0.75$, we show that for intermediate times ($4 < t/t_M < 8$), $\dot{\Gamma}_D / (\Gamma_{shock} / t_M)$, has several consistent behaviors and scaling laws depending on A*. Here Γ_{shock}, is the circulation deposited by the initial shock (which agrees with Γ_{SZ}) and t_M is the time at which the single mode interface becomes multivalued. $\dot{\Gamma}_D$, a highly informative macroscopic variable, provides essential signatures and quantifiers that may be used for understanding and modeling accelerated inhomogeneous flows through intermediate times.

Figure 10.1(b) shows the variation of three normalized circulations (integrated vorticities): positive, negative and total ($\Gamma = \Gamma_- + \Gamma_+$) within the bounding rectangle of Figure 10.1(a), essentially *between the spike* (crest) *and bubble* (trough) extremes. The very-early time normalized *negative* circulation, $\Gamma_- / |\Gamma_{\text{shock}}|$ ~ -1 is deposited by the incoming shock and corresponds mainly to the dominant vorticity adjacent to the mid-contour (as seen in Figure 10.1a). This circulation is in close agreement with that, obtained from the Samtaney-Zabusky formula (1994), Γ_{SZ}, as discussed above. There are also early-time, (e.g., $0 < t/t_M < 1.5$) small-magnitude *positive* and negative vorticities, (not visible on Figure 10.1a) that are generated by the curved transmitted and reflected *shocks* which propagate downstream and upstream, respectively, from the interface and whose curvature arises from the interaction of the incoming

planar shock with the sinusoidally perturbed interface. The Mach number and finite local curvature of these shocks determines the magnitude and sign of the vorticity deposited in the domain behind these shocks, as described recently by Kevlahan (1997) and Wouchuk (2001). For t/t_M > 2.0, the vortex-accelerated vorticity deposition causes both $\Gamma_+ / |\Gamma_{shock}|$ and $\Gamma_- / |\Gamma_{shock}|$ to vary nearly linearly in time and the rate of change of the latter is *larger* than that of the former, so there is small net growth of $|\Gamma / \Gamma_{shock}|$, as will be examined critically below. Also we see the small but rapid "dip" of $\Gamma_- / |\Gamma_{shock}|$ at $t_d / t_M \approx 2.5$, an important signature, to be discussed below.

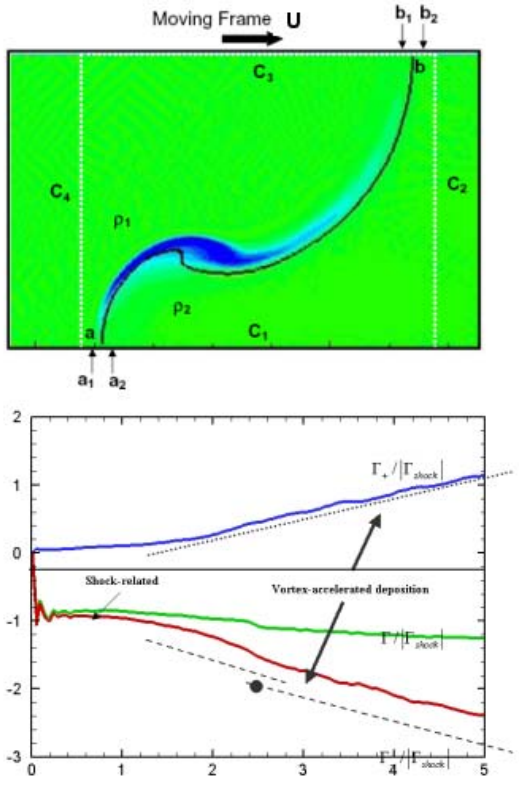

Figure 10.1 (a) Vorticity field with extracted mid-contour interface (solid) at 1.5tM from a numerical simulation for M = 1.3, A*= 0.635. A typical bounding box (dashed lines) for the analytical CCW integration domain is shown. The solid line is the evolved and multivalued "mid-contour" which intersects the upper and lower sides of a bounding rectangle at *a* and *b*, respectively which is between the ends of the transition layer at *a1-a2* and *b1-b2*, respectively. (b) Normalized circulations versus time for M= 1.3 and A*= 0.635. Positive, $\Gamma_+/|\Gamma shock|$, negative, $\Gamma_-/|\Gamma shock|$, and total, $\Gamma/|\Gamma shock|$.

10.1 Derivation of an Approximate Continuum Representation

The governing equation for vorticity evolution of an inviscid three dimensional (3D) compressible fluid is obtained by taking curl of the Euler's momentum equations

$$\partial_t \omega = \nabla \times (\mathrm{u} \times \omega) - \nabla(\rho^{-1}) \times \nabla p \,. \tag{10.1}$$

For Rayleigh-Taylor, the spatially invariant acceleration term does not appear explicitly, but it is present in the pressure gradient which can be obtained from the momentum equation. In a two-dimensional (2D) Cartesian system, $\mathrm{u} = u\mathrm{e}_x + v\mathrm{e}_y$, $\omega = \omega\,\mathrm{e}_z = (-\partial_y u + \partial_x v)\,\mathrm{e}_z$, and $\Gamma_D = \iint_D \omega \, dxdy$. In the present paper, we suppress the domain indicator D because we will integrate the scalar equation for vorticity over a fixed area rectangular domain which bounds the spike and bubble, (e.g. as shown in Figure 10.1a) and obtain

$$\dot{\Gamma} = -\oint_C d\mathrm{s} \cdot (\mathrm{u} \times \omega \mathrm{e}_z) - \oint_C d\mathrm{s} \times (p \nabla(\rho^{-1})) \tag{10.2}$$

Here, we have converted the domain integral to counter-clockwise integration along the straight sides C_i of the bounding rectangle C.

We now make assumptions to obtain a simple approximation formula and then validate by comparing with integrated vorticities obtained from the simulations. For the present work, we omit small vorticity effects, which however become important at Mach numbers > 1.5 as discussed by Wouchuk (2001) and Yang et al (1994) for the very-early or linear time regime. We know, from previous analytical and numerical work in the low M range, that the dominant shock-accelerated vorticity is deposited within the interfacial transition layer (ITL), i.e. remote from the sides C_i. Furthermore, the vorticity is zero at the spike and bubble extrema points, at y=0 and y= λ/2, respectively, because the angle is zero between the normal of the incoming planar shock and the normal to the interface at these points. Hence, if there is no vorticity on the sides of the bounding box, we may omit the first term on the right of (10.2) and obtain

$$\dot{\Gamma} \approx -\int_{a1}^{a2} p(d\rho/\rho^2) - \int_{b1}^{b2} p(d\rho/\rho^2), \tag{10.3}$$

where $\approx$ indicates that we have neglected the small curvature-induced vorticities as well as assumed that the dominant density change occurs only over the small intercepts of the ITL, a_1a_2 and b_1b_2. That is, the contribution from density perturbations associated with small acoustic waves may be neglected.

10.2 Approximations to Obtain Discrete Representations

To minimize the effect of physical and numerical fluctuations, we have found it useful to use temporally averaged pressures and vorticities (designated with a tilde) and obtained from

$$\tilde{f}_{i,j}(t_n) = \sum_{t_m=-t_M/6}^{t_m=+t_M/6} f_{i,j}(t_m)\Phi(t_n;t_m) \tag{10.4}$$

where $\Phi(t_n;t_m) = T^{-1}[1+\cos(2\pi(t_n-t_m)/T)]$, $-(T/2) \le t_m \le (T/2)$, and $T = t_M/3$.

Hence, the quantified circulation rates-of-change, $\dot{\Gamma}^{*}$ *and* $\dot{\Gamma}^{\#}$ are approximated as

$$\dot{\Gamma}^{*} \equiv \frac{\tilde{p}_a(t_n) - \tilde{p}_b(t_n)}{(\rho_2-\rho_1)/\rho_2\rho_1} \tag{10.5}$$

and

$$\dot{\Gamma}^{\#}(t_n) \equiv \sum_{D}^{2} h[\frac{(\tilde{\omega}_{i,j}(t_{n+1}) - \tilde{\omega}_{i,j}(t_{n-1})]}{2\delta t}] \ . \tag{10.6}$$

The former follows from Eq. (10.3) by assuming a density discontinuity at the mid-contour intersections with the horizontal sides of the bounding rectangle, between a_1a_2 *for* $\tilde{p}_a(t)$ and between b_1b_2 *for* $\tilde{p}_b(t)$. The latter approximates the time-derivative of circulation by using: an area-weighted sum; over a temporal central-difference operation; that is applied to the temporally

averaged vorticity. The vorticity is computed by applying a spatial central-difference operation to the velocities. The discretization intervals are $h = 1/180$ and $\delta t = 0.6(\delta t)_c$ for $A^* < 0.3$; and $\delta t = (\delta t)_c$ for $A^* > 0.3$, where $(\delta t)_c = h / C_s = 1/180$. Note, these equations should be more accurate for an incompressible medium where shocks and acoustic waves and their density fluctuations are absent.

10.3 Validating the Approximations

We now validate the applicability of Eq. 10.5 by comparing with Eq. 10.6. The initial ITL of 26 grid zones is compressed by the shock, and after the shock has passed its thickness is somewhat reduced to 17, for A* = 0.2, 0.3 and 16 for A* = 0.5, 0.635 and 0.75. Figure 10.2 shows the variation with A* of some of the temporal and circulation quantities: (a) t_p / t_c, time to reach the first maximum of the normalized amplitude growth-rate, $\dot{a}(t) / C_s$, where C_s is the speed of sound in the incoming medium. This time is, approximately, the transition time between very-early-time and early-time or linear and nonlinear regimes. (The time t_c is related to the time of passage of the shock over some initial length scale and we take it as $t_c = a(0) / MC_s =$ 0.0615 (b) $\dot{a}(t_p) / C_s$, which increases nearly linearly with A*, except for A*=0.2; (c) t_M / t_C, the normalized multivalued time, a monotonically decreasing quantity, except for A*=0.02; (d) $|\Gamma_{shock} / t_M|$ (used for normalization) is compared with $|\Gamma_{SZ}/t_M|$). (Recall, Γ_{shock} is the measured circulation deposited by the shock in our simulations and Γ_{SZ} is the Samtaney-Zabusky analytically derived circulation). The outlier behavior for some of the A*=0.2 results has yet to be investigated.

The curves in Figure 10.3, the essential contribution of this chapter, show excellent agreement through early-intermediate times. They are, Eq. 10.5 (dashed/red) and Eq. .10.6 (solid/blue), both normalized by Γ_{shock} / t_M. For A* = 0.2 and 0.3, the curves vary about the same negative slopes (dashed lines) in $4.5 < t/t_M < 8.0$. For A* = 0.5, 0.635 and 0.75, the curves contain a sharp dip at times t_d that increases with A*. The net *normalized* circulation rate of

change prior to the dip time increases with A* and approaches near constant values of 0.04, 0.05 and 0.07 (in c, d and e), respectively.

This dip phenomenon arises from the increase in density gradient from interface stretching and thinning, mostly at the outermost edges of the “mushroom”, as discussed in Peng *et al.* (2003b). It is possible that the low A* cases will also exhibit a dip and approach to a near-constant value at longer times, but this awaits a study with a more realistic model with viscosity and interfacial diffusivity, as discussed below.

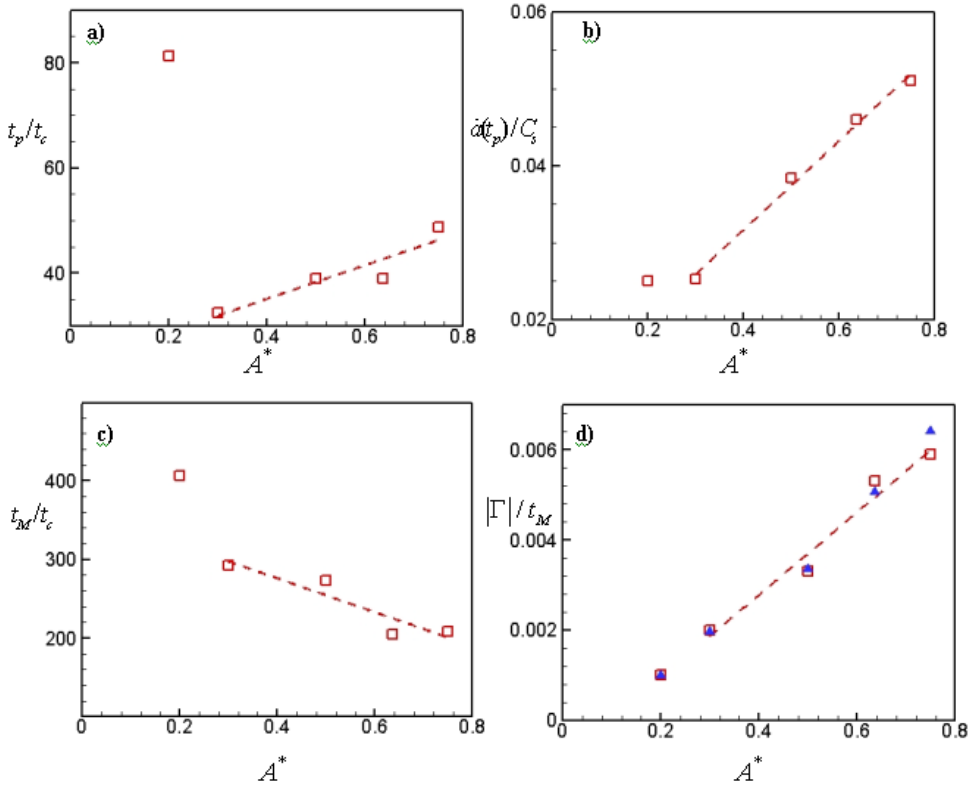

Figure 10.2 Ancillary quantities versus A*:(a) tp / tc, time to reach the first maximum of the normalized amplitude growth rate, $\dot{a}(t)/C_s$, where Cs is the speed of sound in the incoming medium. This time is the transition between linear and nonlinear regimes and is nearly constant, except for A*=0.2. (The normalization tc, is the time for the shock to cross the ITL); (b) $\dot{a}(t_p)/C_s$, which increases nearly linearly with A*, except for A*=0.2; (c) t_M / t_C, the normalized multivalued time, a monotonically decreasing quantity (decreasing by a factor of 2); (d) Primary circulation divided by tM : $|\Gamma_{shock} / t_M|$ from numerical simulations, hollow squares and $|\Gamma_{SZ}/t_M|$, triangles. (Recall, Γ_{shock} is the measured circulation deposited by the shock in our simulations and Γ_{SZ} is the Samtaney-Zabusky analytically derived circulation.)

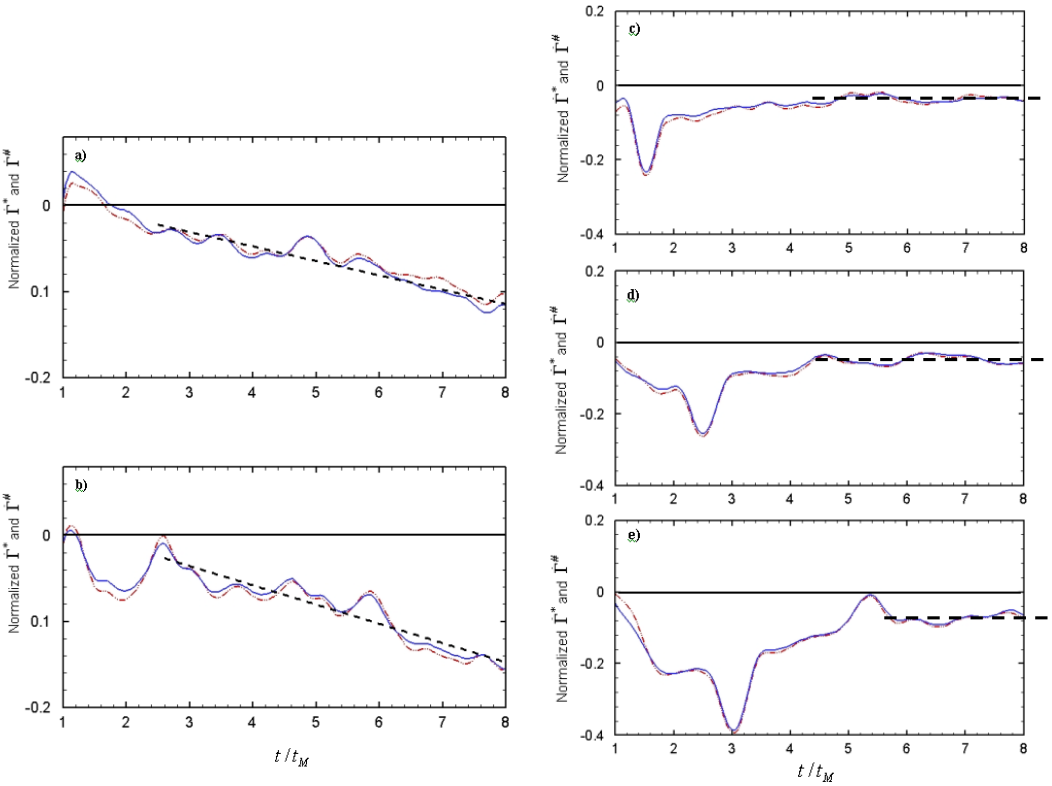

FIG 10.3 Normalized vorticity rate of change $\dot{\Gamma}^*$ (dashed and red) and $\dot{\Gamma}^{\#}$ (solid and blue) as given by approximate formulas Eq. 4 and Eq. 5, respectively, for M = 1.3, A* = 0.2, 0.3, 0.5, 0.635, and 0.75. The normalization is with respect to $|\Gamma_{shock} / t_M|$. Note the scale differences from Figs 10.3a-b with Figs 10.3 c-e.

10.4 Comparisons, Caveats and Future Directions

A. Comparison of Vorticity Fields

In Figures 10.4 a-b, we show the vorticity field in half the domain for A* = 0.635 (at $(t_d / t_M) = 2.5$) and A* = 0.75 (at $(t_d / t_M) = 3.0$)), respectively. These times, where the circulation growth rate has a sharp consistent dip, as shown in Figures 10.3c, d and e are nearly at the beginning of the *intermediate time* phase. Here, positive and negative are red/yellow and blue, respectively. Some significant observations are:

1. For A*= 0.635, the interface has increased significantly in length by rolling up into a complex core. A line at about 34 deg to the horizontal and through the central rolled-up domain will cut at *six* locations the interface and its associated close-lying vorticity layers (from left-to-right: *yellow (innermost); blue; yellow;* center-blue; *blue; (isolated), red, blue (outermost))*. The alternating signs, red/yellow and blue are evidence of the VAVD process at high-gradient interfaces where the slope is *decreasing* and *increasing*, respectively.
2. For A*= 0.75, the roll-up domain has become more complex and has begun to interact with the neck and inner edges _red-yellow_ of the mushroom cap and is well advanced toward a 2D baroclinic-turbulent state. Note, that the blue vorticity layer at the lower edge has already rolled up clockwise into smaller compact localized structures which are continuing the VAVD process and are generating new positive domains and forming “vortex projectiles.”

B. Assumptions and their modification

The derivation of Eqs. 10.5 and 10.6, involves many physical, procedural, and numerical assumptions. They’re remarkable agreement in Figure 10.3 undoubtedly arises from cancellations and we consider these equations as leading order terms in an asymptotical expansion. In particular, more realistic formulas must include the media viscosities and the interfacial surface tension and diffusivity. These augmentations will allow us to understand properly how the interfacial transition layer (ITL) becomes thinner and longer as it experiences gradient enhancement. At later times, following “baroclinic” roll-up, the regions will become turbulent. Also, one must consider the initial fluctuation spectra of the fluid in the ITL. The smaller length scales will be greatly modified by diffusive and viscous physical effects in the mass conservation and momentum equations, respectively. We must also: consider the use of a properly smoothed instantaneous extracted interface rather than the evolving midcontour; reconsider the choice of the location of the two points at which the averaged pressures are

evaluated in Eq. 10.5; vary appropriately the discrete resolution and numerical order of accuracy of the spatial and temporal differencing and temporal filtering operations.

Following the discussion above, one must understand the significant differences in the small versus large A* evolutionary behaviors by scrutinizing these regions with more cases to determine the vortex-baroclinic processes involved. Similarly, larger Mach numbers, greater than 2.0, should be considered to examine the effects of the important bulk vorticity that is remote from the interface and is left behind by the receding curved reflected and transmitted shocks. The generalization of these formulas to axisymmetry should be straightforward. To appreciate the turbulent nature of the evolving complex cores and their interaction, one should seek formulas for the evolution of separate positive and negative circulation rates of change and their corresponding enstrophies.

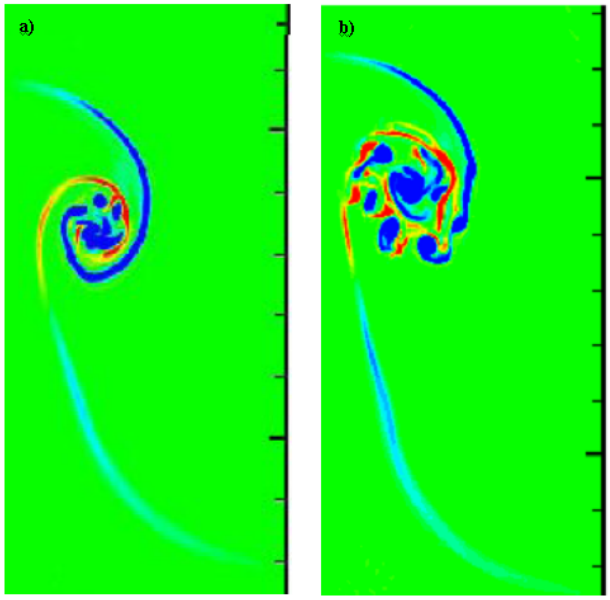

Figure 10.4 Vorticity field in half the domain at td, the time where the circulation growth rate has a sharp consistent dip for (a) A* = 0.635 and (b) A* = 0.75. Blue is negative and red is positive.

Chapter 11

Summary and Conclusions

For Part II

The main purpose of Part II of this dissertation is the *v*ortex-*a*ccelerated *v*orticity *d*eposition (VAVD) and long-time dynamics of two-dimensional single-mode Richtmyer-Meshkov interfaces. We include a small-but–finite interfacial transition layer (ITL) to make the problem well posed and thus are able to study the late-intermediate time flow behaviors. We develop algorithms to extract the medial axis of the ITL. We obtain quantitative agreements and correct trends when compared with the Jacobs and Krivets experiment. This includes amplitude growth, large and intermediate scaled structures, e.g. complex mushroom rollup scales. The experiment is affected by 3D symmetry breaking perturbations, wall and viscous effects. These account for the scatter of the data at early-intermediate times and may also cause an amplitude growth rate larger than that simulated.

Opposite-signed secondary vorticity is deposited by the VAVD on the neck of the mushroom, close to the spike region and is rolled into a VBL that is very unstable and produces small-scale structures within the rollups. Furthermore, the VAVD process is enhanced by the stretching of the interface or density gradient intensification across the interface. The physical effects of secondary vorticity on the mixing zone dynamics are further analyzed by calculating the amplitude growth rate $\dot{a}$. The power-law exponent p in the t^{-p} is sensitive to the time interval over which the simulation data is fitted. The exponent p is very small if the data fitted is only for late-intermediate times. In fact, our data shows that $\dot{a}$ approaches a near-constant value at late-

intermediate times. We also introduce an *adjusting* periodic single point vortex model which gives excellent results for $\dot{a}$ at low Atwood numbers. We quantify the turbulent aspects from early to intermediate times with several measures including: the one-dimensional averaged transversal kinetic energy spectrum that gives spectral exponent -3; and enstrophy and normalized skewness and flatness. Note, secondary baroclinic vorticity deposition provides a long-time forcing to the turbulent epoch.

The vortex-accelerated vorticity deposition process examined and the new quantification procedures, the circulation rate of change, comprise a vortex paradigm for examining the effect of specific initial conditions on the evolution of RM and RT interfaces through intermediate times. This approach applies also to axisymmetric evolutions and can be generalized to other (accelerated) inhomogeneous flows, for example shock-cylinder (Zhang et al 2004). To appreciate the turbulent nature of the evolving complex cores and their interaction, one should seek formulas for the evolution of separate positive and negative circulation rates of change and their corresponding enstrophies.

In the future, it is desirable to couple more closely such Richtmyer-Meshkov experiments and 3D Navier-Stokes simulations. They should be studied in the high Atwood and Mach number domains because we have identified strange effects at high Atwood numbers where density fluctuations and vorticity (remote from the interface that is left behind by the propagating curved reflected and transmitted shocks) can be important.

References

Part I:

K. B. Abbitt and G. B. Nash, Rheological properties of the blood influencing selectin-mediated adhesion of flowing leukocytes, Am J Physiol Heart Circ Physiol 285: H229–H240 (2003).

M. Abkarian, C. Lartigue, A. Viallat, Tank treading and unbinding of deformable vesicles in shear flow: Determination of the lift force, Physical Rev Letts 88 (6), 068103 (2002).

B. Alberts, A. Johnson, J. Lewis, M. Raff, K. Roberts, and P. Walter, Molecular Biology of the Cell, 4th ed. Garland, New York, (2002).

R. Alon, S. Chen, K.D. Puri, E.B. Finger, and T.A. Springer, The kinetics of L-selectin tethers and the mechanics of selectin-mediated rolling, J. Cell Biol. 138, 1169 (1997).

R. Alon, R. Fuhlbrigge, E.B. Finger, and T. Springer, Interaction through L-selectin between Leukocyte and adherent leukocytes nucleate rolling adhesions on selectins and VCAM-1 in shear flows, J. Cell Biol. 135, 849 (1996).

R. Alon, D.A. Hammer, and T.A. Springer, Lifetime of the P-selectin-carbohydrate bond and its respose to tensile force in hydrodynamic flow, Nature 374, 539 (1995).

P. Bagchi, Mesoscale Simulation of Blood Flow in Small Vessels Biophys. J. 92, 1858 (2007).

K.A. Barbee, Role of subcellular shear-stress distributions in endothelial cell mechanotransduction, Annals Biomed. Eng. 30, 472 (2002).

K.A. Barbee, P. Davies, R. Lal, Shear stress-induced reorganization of the surface topography of living endothelial cells imaged by atomic force microscopy, Circ Res. 74(1), 163 (1994).

G.I. Bell, Models for the specific adhesion of cells to cells, Science 200, 618 (1978).

G.I. Bell, M. Dembo, and P. Bongrand, Competition between non-specific repulsion and specific bonding, Biophys. J. 45, 1051 (1984).

S.A. Berger and L.-D. Jou, Flows in stenotic vessels, Annu. Rev. Fluid Mech. 32, 347 (2000).

P. Bongrand, Ligand-receptor interactions, Rep. Prog. Phys. 62, 921 (1999).

R.E. Bruehl, T. A. Springer, and D. F. Bainton. 1996. Quantitation of L-selectin distribution on human leukocyte microvilli by immunogold labeling and electron microscopy. J. Histochem. Cytochem. 44:835– 844.

E. C. Butcher, “Leukocyte-endothelial cell recognition: Three or more steps to specificity and diversity,” Cell 67, 1033 (1991).

E. C. Butcher and L. J. Picker, Lymphocyte homing and homeostasis, Science 272, 60 (1996).

K.-C. Chang, D.F.J. Tees, and D.A. Hammer, The state diagram for cell adhesion under flow: leukocyte rolling and firm adhesion. Proc. Natl. Acad. Sci. U.S.A. 97, 11262 (2000).

J. M. Charrier, S. Shrivastava, and R. Wu, ‘‘Free and constrained inflation of elastic membranes in relation to thermoforming non-axisymmetric problems,’’ J. Strain Anal. 24, 55 (1989)

S. Chen and T.A. Springer, An automatic braking system that stabilizes leukocyte rolling by an increase in selectin bond number with shear, J. Cell Biol. 144,185 (1999).

S. Chien, Shear dependence of effective cell volume as a determinant of blood viscosity, Science 168(934), 977 (1970).

H. Choi and P. Moin, Effects of the computational time step on numerical solutions of turbulent flow, J. Comput. Phys 113, 1 (1994).

E.R. Damiano, J. Westheider, A. Tozeren, and K. Ley, Variation in the velocity, deformation, and adhesion energy density of leukocyts rolling within venules, Circ. Res. 79, 1122 (1996).

M. Dembo, D.C. Torney, K. Saxman, and D.A. Hammer, The reaction-limited kinetics of membrane-to-surface adhesion and detachment. Proc. R. Soc. Lond. B. Biol. Sci. 234, 55 (1988).

C. Dong, J. Cao, E. J. Struble, and H. H. Lipowsky. 1999. Mechanics of leukocyte deformation and adhesion to endothelium in shear flow. Ann. Biomed. Eng. 27:298–312.

Dong, C., and X. X. Lei. 2000. Biomechanics of cell rolling: shear flow, cell-surface adhesion, and cell deformability. J. Biomech. 33:35–43.

C. Dong and R. Skalak, Leukocyte deformability: finite element modeling of large viscoelastic deformation, J. Theor. Boil. 158, 173 (1992).

C. Dong, R. Skalak, and K.-L. P. Sung, Cytoplasmic rheology of passive neutrophils. Biorheology 28: 557 (1991).

C. Dong, R. Skalak, K.-L. P. Sung, G. W. Schmid-Schönbein, and S. Chien, “Passive deformation analysis of human leukocytes,” J. Biomech. Eng. 110, 27 (1988).

C. Eggleton and A. Popel, Large deformation of red blood cell ghosts in a simple shear flow, Phys. Fluids 10(8), 1834 (1998).

Ehrhardt C, Kneuer C, Bakowsky U, Selectins - an emerging target for drug delivery ADVANCED DRUG DELIVERY REVIEWS 56 (4): 527-549 MAR 3 2004

Eniola AO, Rodgers SD, Hammer DA, Characterization of biodegradable drug delivery vehicles with the adhesive properties of leukocytes, BIOMATERIALS 23 (10): 2167-2177 MAY 2002

E.E. Eriksson, X. Xie, J. Werr, P. thoren, and L. Lindbom, Importance of primary capture and L-selectin-dependent secondary capture in leukocyte accumulation in inflammation and atherosclerosis in vivo, J. Exp. Med. 194, 205 (2001).

E. Evans, Detailed mechanics of membrane-membrane adhesion and separation I Continuum of molecular cross-bridges, Biophys. J. 48, 175–183 (1985).

E. Evans, Physical actions in biological adhesion, Handbooks of Biophysics (edited by R. Lipowski and E. Sackman), Elsevier, Amsterdam (1993).

E. Evans and K. Ritchie, Dynamic strength of molecular adhesion bonds, Biophys. J. 72, 1541 (1997).

E. Evans and B. Kukan, Passive material behavior of granulocytes based on large deformation and recovery after deformations tests, Blood 64, 1028–1035 (1984).

E. Evans and R. Skalak, Mechanics and Thermodynamics of Biomembranes, CRC Press, Boca Raton, FL (1979).

E. Evans and Yeung, Apparent viscosity and cortical tension of blood granulocytes by micropipet aspiration, Biophys. J. 56, 151–160 (1989).

E. A. Fadlun, R. Verzicco, P. Orlandi, and J. Mohd-Yusof, Combined immersed-boundary finite-difference methods for three-dimensional complex flow simulations, J. Comput. Phys. 161, 35 (2000).

R. Fahraeus and T. Lindqvist, The viscosity of the blood in narrow capillary tubes, Am J. Physiol. 96, 562 (1931).

J.H. Ferziger and M. Peric, Computational Methods for Fluid Dynamics, third ed., Springer Verlag, Berlin, Heidelberg (2001)

J.C. Firrel and H.H. Lipowsky, Leukocyte margination and deformation in mesenteric venules of rat, Am. J. Physiol. Heart Circ Physiol. 256, H1667 (1989).

P.S. Frenette, Sickle cell vasoocclusion:heterotypic, multicellular aggregations driven by leukocyte adhesion, Microcirculation 11, 167 (2004).

J.B. Freund, Leukocyte margination in a model microvessel, Phys. Fluids 19, 023301 (2007).

Y.C. Fung, Mechanical properties of living tissues, Springer-Verleg (1993).

Y.C. Fung and S.Q. Liu, Elementary mechanics of the endothelium of blood vessels, J. Biomech. Eng. 115, 1 (1993).

Y.C. Fung and P. Tong, Theory of the sphering of red blood cells, Biophys. J. 8, 175 (1968).

P. Gaehtgens, C. Duhrssen and K.H. Albrecht, Motion, deformation, and interaction of blood cells and plasma during flow through narrow capillary tubes, Blood Cells 6(4), 799 (1980).

J.-P. Girard and T.A. Springer, High endothelial venules (HEVs): specialized endothelium for lymphocyte migration, Immunology Today 16, 449 (1995).

Goldman, A. J., R. G. Cox, and H. Brenner., Slow viscous motion of a sphere parallel to a plane wall. 2. Couette flow. Chem. Eng. Sci. 22, 653 (1967).

D. Goldstein, R. Handler, and L. Sirovich, Modeling a no-slip flow boundary with an external force field, J. Comput. Phys. 105, 354 (1993).

D.A. Hammer and S.M. Apte, Simulation of cell rolling and adhesion on surfaces in shear flow: general results and analysis of selectin-mediated neutrophil adhesion, Biophys. J. 62, 35 (1992).

D.A. Hammer and D. A. Lauffenburger, dynamical model for receptor-mediated cell adhesion to surfaces. Biophys. J. 52, 45 (1987).

D.A. Hammer and Mr. Tirrell, Biological adhesion at interfaces, Annu. Rev. Mater. Sci. 26, 651–691 (1996).

W. Helfrich, Elastic properties of lipid bilayers: theory and possible experiments, Z Naturforsch 28(11), 693 (1973).

B.P. Helmke, S.N. Bremner, B.W. Zweifach, R. Skalak, and G.W. Schmid-Schonbein, Mechanisms for increased blood flow resistance due to leukocytes, , Am. J. Physiol. Heart Circ Physiol. 264, H2884 (1997).

C. A. St. Hill, S. R. Alexander, and B. Walcheck, Indirect capture augments leukocyte accumulation on P-selectin in flowing whole blood, Journal of Leukocyte Biology Volume 73, 464-471 (2003)

R.M. Hochmuth, H.P. Ting-Beall, B.B. Beaty, D. Needham, and R. Tran-Son-Tay, Vcosity of passive human neutrophils undergoing small deformations, Biophys J. 64(5), 1596 (1993).

S.D. House and H.H. Lipowsky, Leukocyte-edothelium adhesion: microhemodynamics in mesentery of the rate, Microvasc. Res. 34, 363 (1987).

G. Iaccarino and R. Verzicco, Immersed boundary technique for turbulent flow simulations, Appl. Mech. Rev. 56 (2003) 331–347.

D.E. Ingber, Tensegrity I. Cell structure and hierarchical systems biology, J Cell Sci.116, 1157 (2003).

S. Jadhav, C.D. Eggleton, and K. Konstantopoulos, A 3-D computational model predicts that cell deformation affects selectin-mediated leukocyte rolling, Biophys. J. 88, 96 (2005).

K.E. Kadash, M.B. Lawrence, and S.L. Diamond, Neutrophil string formation: hydrodynamic thresholding and cellular deformation during cell collisions, Biophys. J. 86, 4030 (2004).

R.D. Kamm, Cellular fluid mechanics, Annu. Rev. Fluid Mech. 34, 211 (2002).

G.S. Kansas, Selectins and their ligands: current concepts and controversies, Blood 88, 3259 (1996).

V. Kantsler and V. Steinberg, Orientation and dynamics of a vesicle in tank-treading motion in shear flow, Phys. Rev. Letts 95 (25), 258101 (2005).

V. Kantsler, E. Segre and V. Steinberg , Vesicle dynamics in time-dependent elongation flow: wrinkling instability, Phys Rev Lett. 99(17), 178102 (2007).

D.B. Khismatullin and G. Truskey, Three-dimensional numerical simulation of receptor-mediated leukocyte adhesion to surfaces: Effects of cell deformability and viscoelasticity, Phys. Fluids 17, 031505 (2004).

J. Kim and P. Moin, Application of a fractional-step method to incompressible Navier–Stokes equations, J. Comput. Phys. 59, 308 (1985).

M. King and D. Hammer, Multiparticle adhesive dynamics: hydrodynamic recruitment of rolling leukocyte, Proc. Natl. Acad. Sci. USA 98, 14919 (2001).

D. N. Ku, Blood flow in arteries, Annu. Rev. Fluid Mech. 29, 399 (1997).

M. Kraus, W. Wintz, U. Seifert, and R. Lipowsky, Fluid vesicles in shear flow, Phys. Rev. Lett. 77, 3685 (1996).

M. Lai and C.S. Peskin, An immersed boundary method with formal second-order accuracy and reduced numerical viscosity, J. Comput. Phys. 160 (2000) 705–719.

D. A. Lauffenburger and J. J. Linderman. 1993. Receptors: Models for Binding, Trafficking, and Signaling. Oxford University Press, New York.

M. B. Lawrence and T. A. Springer, Leukocytes roll on a selectin at physiologic flow rates: Distinction from and prerequisite for adhesion through integrins, Cell 65, 859 (1991).

M. B. Lawrence, G. S. Kansas, E. J. Kunkel, and K. Ley, Threshold levels of fluid shear promote leukocyte adhesion through selectins sCD62L,P,Ed, J. Cell Biol. 136, 717 (1997).

L. Lee and R. J. Leveque, An immersed interface mthod for incompressible Navier-Stokes equations, SIAM J. Sci. Comput. 25, 832-856 (2003).

K. Ley, T.F. Tedder, and G.S. Kansas, L-selectin can mediate leukocyte rolling in untreated mesenteric venules in vivo independent of E- or P-selectin, Blood 82(5), 1632 (1993).

J. Li, Y.Y Renardy, and M. Renardy, A numerical study of periodic disturbances on two-layer Couette flow, Phys. Fluids 10(12), 3056 (1998).

C.T. Lim, E.H. Zhou, S.T. Quek, Mechanical models for living cells—a review, Journal of Biomechanics 39, 195–216 (2006).

A.L.F. Lima E. Silva, A. Silveira-Neto, and J.J.R. Damasceno, Numerical simulation of two-dimensional flows over a circular cylinder using the immersed boundary method, J. Comput. Phys. 189, 351 (2003).

A. J. Lusis, “Atherosclerosis,” Nature 407, 233 (2000).

S. Majumdar, G. Iaccarino, P. Durbin, RANS solvers with adaptive structured boundary non-conforming grids, in: Annual Research Briefs, NASA Ames Research Center/Stanford University Center for Turbulence Research, Stanford, CA, 353 (2001).

B. T. Marshall, M. Long, J. W. Piper, T. Yago, R. P. McEver, and C. Zhu, “Direct observation of catch bonds involving cell-adhesion molecules,” Nature London 423, 190 (2003).

R. P. McEver, Selectins: lectins that initiate cell adhesion under flow, Curr Opin Cell Biol. 14(5), 581 (2002).

R.J. Melder, J. Yuan, L.L. Munn, and R.K. Jain, Erythrocytes enhance lymphocyte rolling and arrest in vivo, Microvas. Res. 59, 316 (2000).

R. Mittal and G. Iaccarino, Immersed boundary method, Annual Review Fluid Mech. 37, 239 (2005).

J. Mohd-Yusof, Combined Immersed-Boundary/B-Spline Methods for Simulations of Flow in Complex Geometries, Annual Research Briefs (Center for Turbulence Research, NASA Ames and Stanford University, 1997), p. 317.

Y. Morinishi, T.S. Lund, O.V. Vasilyev, and P. Moin, Fully conservative higher order finite difference schemes for incompressible flow, J. Comput. Phys 143, 90 (1998)

N.A. N'Dri, W. Shyy, and R. Tran-Son-Tay, Computational modeling of cell adhesion and movement using a continuum-kinetics approach, Biophys. J. 85, 2273 (2003).

D. Needham and R.M. Huchmuth, A sensitive measure of surface stress in the resting neutrophil. Biophys J. 61(6), 1664 (1992)

E. Y. H. Park, M. J. Smith, E. S. Stropp, K. R. Snapp, J. A. DiVetro, W. F. Walker, D. W. Schmidtke, S. L. Diamond, and M. B. Lawrence, "Comparison of PSGL-1 microbead and neutrophil rolling: Microvillus elongation stabilizes P-selectin bond clusters," Biophys. J. 82, 1835 (2002).

C.S. Peskin, Flow patterns around heart valves: a numerical method, J. Comput. Phys. 10, 252 (1972).

C. Pozrikidis, Effect of membrane bending stiffness on the deformation of capsules in simple shear flow. J. Fluid Mech. 440, 269 (2001).

W. H. Press, S. A. Teukolsky, W. T. Vetterling, and B. P. Flannery, Numerical Recipe in Fortran 90 (2nd Edition), Cambridge University Press (1996).

A.R. Pries, T.W. Secomb, and P. Gaehtgens, Biophysical aspects of blood flow in the microvasculature, Cardiovas. Res. 32, 654 (1996).

A.R. Pries, T.W. Secomb, and P. Gaehtgens, The endothelial surface layer, Pflugers Arch. 440(5):653 (2000).

S. Popinet and S. Zaleski, A front tracking algorithm for accurate representation of surface tension, Int. J. Numer. Meth. Fluids 30, 775 (1999).
S. D. Rosen, Ligands for L-selectin: Homing, Inflammation, and Beyond, Annu. Rev. Immunol. 22, 129 (2004).

R. Ross, Atherosclerosis --- an inflammatory disease, New England J. Med 340, 115 (1999).

E. M. Saiki and S. Biringen, Numerical simulation of a cylinder in uniform flow: Application of a virtual boundary method, J. Comput. Phys. 123, 450 (1996).

R. L. Satcher, S.R. Bussolari, M.A. Gimbrone, and C.F. Dewey, The distribution of fluid forces on model arterial endothelium using computational fluid dynamics, J. Biomech. Eng. 114, 309 (1992).

R. L. Satcher and C. F. Dewey Jr., Theoretical estimates of mechanical properties of the endothelial cell cytoskeleton, Biophys. J. 71, 109 (1996).

R. Scardovelli and S. Zaleski, "Direct numerical simulation of free surface and interfacial flow," Annu. Rev. Fluid Mech. 31, 567 (1999).

G.W. Schmid-Schonbein, S. Usami, R. Skalak, and S. Chien, The interaction of leukocyte and erythrocytes in capillary and postcapillary vessels, Microvasc. Res. 19, 45 (1980).

G.W. Schmid-Schonbein, Y.Y. Shih and S. Chien, Morphometry of human leukocytes, Blood 56, 866 (1980).

T.W. Secomb, Mechanics of blood flow in the microcirculation, Symp Soc Exp Biol. 49, 305 (1995).

T.W. Secomb, R. Hsu, and A.R. Pries, Blood flow and red blood cell deformation in nonuniform capillaries: Effects of the endothelial surface layer, Microvasc. Res. 9, 189 (2002).

T.W. Secomb, M.A. Konerding, C.A. West, M. Su, A.J. Young, and S.J. Mentzer, Microangiectasias: structural regulators of lymphocyte transmigration, Proc. Natl. Acad. Sci. USA 100, 7231 (2003).

A. W. Segal, How neutrophils kill microbes, Annu. Rev Immunology 23, 197 (2005).

U. Seifert, Hydrodynamics lift on bound vesicle, Phys. Rev. Lett. 83, 876 (1999).

J.Y. Shao, H.P. Ting-Bell, and R.M. Hochmuth, Static and dynamic lengths of neutrophil microvilli, Proc. Natl. Acad. Sci. USA 95, 6797 (1998).

S. Shrivastava and J. Tang, ‘‘Large deformation finite element analysis of non-linear viscoelastic membranes with reference to thermoforming,’’ J. Strain Anal. 28, 31 (1993)

W. Shyy, M. Francois, H.S. Udaykumar, N. N’dri, and R. Tran-Son-Tay, Moving boundaries in micro-scale biofluid dynamics, Appl. Mech. Rev. 54, 405 (2001).

S.J. Singer and G. L. Nicholson, The fluid mosaic model of the structure of cell membranes Science 175, 720 (1972)

R. Skalak, A. Tözeren, P. R. Zarda, and S. Chien, “Strain energy function of red blood cell membranes,” Biophys. J. 13, 245 (1973)

R. Skalak, S.R. Keller, T.W. Secomb, Mechanics of blood flow, J Biomech Eng. 103(2), 102 (1981).

M. L. Smith, D. S. Long, E. R. Damiano, and K. Ley , Near-wall micro-PIV reveals a hydrodynamically relevant endothelial surface layer in venules in vivo, Biophys. J. 85, 637 (2003).

T.A. Springer, Adhesion receptors of the immune system, Nature 346, 425 (1990).

T.A. Springer, Traffic signals for lymphocyte recirculation and leukocyte emigration: the multistep paradigm, Cell 76, 301 (1994).

J. M. Squire, M. Chew, G. Nneji, C. Neal, J. Barry, and C.C. Michel, Quasi-periodic substructure in the microvessel endothelial glycocalyx: a possible explanation for molecular filtering?, J. Struct. Biol. 136, 239 (2001).

J.V. Stein, G. Cheng, B.M. Stockton, B.P. Fors, E.C. Butcher, and U.H. Andrian, L-selectin-mediated leukocyte adhesion in vivo: microvillous distribution determines tether efficiency but not rolling velocity, J. Exp. Med. 189, 37 (1999).

C. Sun, C. Migliorini, and L. Munn, Red blood cells initiate leukocyte rolling in postcapillary expansions: a Lattice-Botlzmann analysis, Biophys. J. 85, 208 (2003).

C.A. Taylor and M.T. Draney, Experimental and Computational Methods in Cardiovascular Fluid Mechanics, Annu. Rev. Fluid Mech. 36, 197 (2004).

W.E. Thomas, E. Trintchina, M. Forero, V. Vogel, and E.V. Sokurenko, Bacterial adhesion to target cells enhanced by shear force, Cell 109(7), 913 (2002).

R. Tran-Son-Tay, H. P. Ting-Beall, D. V. Zhelev, and R. M. Hochmuth. 1994. Viscous behavior of leukocytes. In: Cell Mechanics and Cellular Engineering, V. C. Mow, F. Guilak, R. Tran-Son-Tay, and R. M. Hochmuth, editors. Springer-Verlag, New York. 22–32.

R. Tran-Son-Tay, D. Needham, A. Yeung, and R. M. Hochmuth, "Time-dependent recovery of passive neutrophils after large deformation," Biophys. J. 60, 856 (1991).

G. Tryggvason, B. Bunner, A. Esmaeeli, D. Juric, N. Al-Rawahi, W. Tauber, J. Han, S. Nas, and Y.-J. Jan, A front-tracking method for the computations of multiphase flows, J. Comput. Phys. 169, 708 (2001).

M. A. Tsai, R. S. Frank, and R. E. Waugh, "Passive mechanical behavior of human neutrophils: Power-law fluid," Biophys. J. 65, 2078 (1993).

Y.-H. Tseng and J.H. Ferziger, A ghost-cell immersed boundary method for flow in complex geometry, J. Comput. Phys. 192, 593 (2003).

A. Turhan, L.A. Weiss, N. Mohandas, B.S. Coller, P.S. Frenette, Primary role for adherent leukocytes in sickle cell vascular occlusion: a new paradigm, Proc. Natl. Acad. Sci. USA 99, 3047 (2002).

H.S. Udaykumar, R. Mittal, P. Rampunggoon, A. Khanna, A sharp interface Cartesian grid method for simulating flows with complex moving boundaries, J. Comput. Phys. 174 (2001) 345–380.

S.O. Unverdi and G. Tryggvason, A front-tracking method for viscous, incompressible, multi-fluid flows, J. Comput. Phys. 100, 25 (1992).

R. Verzicco R, J. Mohd-Yusof, P. Orlandi, and D. Haworth, LES in complex geometries using boundary body forces, AIAA J. 38, 427 (2000).

D. Vestweber and J.E. Blanks, Mechanisms that regulate the function of the selections and their ligands, Physiol. Rev. 79, 181 (1999).

Vink H, Duling BR, Identification of distinct luminal domains for macromolecules, erythrocytes, and leukocytes within mammalian capillaries. Circ Res 79:581–589 (1996).

U. H. von Andrian, S. R. Hasslen, S. Erlandsen, and E. C. Butcher, "A central role for microvillous receptor presentation in leukocyte adhesion under flow," Cell 82, 989 (1995).

N. Wang, J.P. Butler, and D.E. Ingber, Mechanotransduction across the cell surface and through the cytoskeleton Science 260, 1124 (1993).

S. Weinbaum, X. Zhang, Y. Han, H. Vink, and S.C. Cowin, Mechanotransduction and flow across the endothelial glycocalyx, Proc. Natl. Acad. Sci. USA 100, 7988–7995 (2003).

C. H. K. Williamson, Oblique and parallel modes of vortex shedding in the wake of a circular cylinder at low Reynolds numbers, J. Fluid Mech. 206, 579 (1989).

T.A. Yago, A. Leppanen, H. Qiu, W.D. Marcus, M.U. Nolbert, and C. Zhu, R.D. Cummings, and R.P. McEver, Distinct molecular and cellular contributions to stabilizing selectin-mediated rolling under flow, J. Cell Biol 158, 787 (2002).

T.Ye, R. Mittal, H. S. Udaykumar, and W. Shyy, An accurate Cartesian grid method for viscous incompressible flows with complex immersed boundaries, *J. Comput. Phys.* **156**, 209 (1999).

A. Yeung and E. Evans, Cortical shell-liquid core model for passive flow of liquid-like spherical cells into micropipets, Biophys J. 56(1), 139 (1989).

Y. Zang, R.L. Street, J.R. Koseff, A non-staggered grid, fractional step method for time-dependent incompressible Navier–Stokes equations in curvilinear coordinates, J. Comput. Phys. 114 (1994) 18–33.

C. Zhu, Kinetics and mechanics of cell adhesion, J. Biomech. 33, 23 (2000).

Part II:

D. Arnett, The role of mixing in astrophysics, Astrophys. J. Suppl. 127, 213 (2000).

G. Baker, D.R. Caflisch, and M. Siegel, Singularity formation during the Rayleigh-Taylor instability, J. Fluid Mech. 252, 51 (1993).

M. Brouillette, The Richtmyer-Meshkov instability, Annu. Rev. Fluid Mech. 34, 445 (2002).

S. Chandrasekhar, Hydrodynamic and Hydromagnetic Stability (Oxford University Press, Oxford (1961).

P. Colella and P.R. Woodward, The piecewise parabolic method (PPM) for gas-dynamical simulations, J. Comp. Phys. 54, 174 (1984).

A. L. Cook, W. H. Cabot and P. L. Miller, The mixing transition in Rayleigh–Taylor instability, J. Fluid Mech. (2004), 511, 333 (2004).

D. G. Dritschel, simulations with contour-advective semi-Lagrangian (CASL) code in a periodic domain with a small-amplitude, sinusoidal, thin vortex layer show roll-ups prior to the multivalue time when the vortex layer first becomes multivalued (private communication, 2001).

D.G. Dritschel and M.H.P. Ambaum , A contour-advective semi-Lagrangian numerical algorithm for simulating fine-scale conservative dynamical fields, Q. J. R. Meteorol. Soc. 123, 1097 (1997).

D.G. Dritschel, P.H. Haynes, M.N. Juckes, and T.G. Sheperd, The stability of a two-dimensional vorticity filament under uniform strain,"J. Fluid Mech. 230, 647 (1991).

J. Hawley and N.J. Zabusky, Vortex paradigm for shock accelerated density stratified interfaces,"Phys. Rev. Lett. 63,1241 (1989).

R.L. Holmes, G. Dimonte, B. Fryxell, M.L. Gittings, J.W. Grove, M. Schneider, D.H. Sharp, A.L. Velikovich, R.P. Weaver, and Q. Zhang, Richtmyer-Meshkov instability growth: experiment, simulation and theory,"J. Fluid Mech. 389, 55 (1999).

T.Y. Hou, J.S. Lowengrub, and M.J. Shelley, The long-time motion of vortex sheets with surface tension,"Phys. Fluids 9, 1933 (1997).

J.W. Jacobs, and J.M. Sheeley, Experimental study of incompressible Richtmyer-Meshkov instability, Phys. Fluids 8, 405 (1996).

J.W. Jacobs and V.V. Krivets, PLIF flow visualization of the nonlinear development and transition to turbulence of Richtmyer-Meshkov instability, in Proceedings of the 23rd International Symposium on Shock Waves, Fort Worth, Texas, USA (2001).

B.D. Jones and J.W. Jacobs, A membraneless experiment for the study of Richtmyer–Meshkov instability of a shock-accelerated gas interface, Phys. Fluids 9, 3078 (1997).

N. K. Kevlahan, The vorticity jump across a shock in a non-uniform flow, J. Fluid Mech. 341, 371 (1997).

A. D. Kotelnikov, J. Ray, and N.J. Zabusky, Vortex morphologies on reaccelerated interfaces: visualization, quantification and modeling of one- and two-mode compressible and incompressible environments, Phys. Fluids 12, 3245 (2000).

R.H. Kraichnan, Inertial ranges in two-dimensional turbulence, Phys. Fluids 10, 1417 (1967).

R. Krasny and M. Nitsche, The onset of chaos in vortex sheet flow, J. Fluid Mech. 454, 47 (2002).

D. Layzer, On the instability of superposed fluids in a gravitational field, Astrophys. J. 122, 1 (1955).

D.-K. Lee, G. Peng, and N.J. Zabusky, Circulation rate of change: A vortex approach for understanding accelerated inhomogeneous flows through intermediate times, Physics of Fluids 18, 097102 (2006).

M. Lesieur, C. Staquet, P. Le Roy, and P. Comte, The mixing layer and its coherence examined from the point of view of two- dimensional turbulence, J. Fluid Mech. 192, 511 (1988).

R. J. LeVeque, Numerical methods for conservation laws. Lectures in Mathematics, ETH Zurich, Brikhauser Verlag (1992).

J. Lindl, Development of the indirect-drive approach to inertial confinement fusion and the target physics basis for ignition and gain, Phys. Plasmas 2, 3933 (1995).

D. Meiron and M. Meloon, Richtmyer-Meshkov instability in compressible stratified fluids, in Proceedings of the 6th International Workshop on the Physics of Compressible Turbulent Mixing, 337 (1997).

E.E. Meshkov, Interface of two gases accelerated by a shock wave, Fluid Dynamics 4, 101 (1969).

G. Peng, N. J. Zabusky and S. Zhang, Vortex-accelerated secondary baroclinic vorticity deposition and late-intermediate time dynamics of a two-dimensional Richtmyer–Meshkov interface, Phys Fluids 15, 3730 (2003).

S. B. Pope, Turbulent Flows, Cambridge University Press, Cambridge England, Sec. 6.7.4 (2000).

D. H. Porter, A. Pouquet, and P. R. Woodward, Kolmogorov-like spectra in decaying three-dimensional supersonic flows, Physics Fluids 6, 2133 (1994).

J.K. Prasad, A. Rasheed, S. Kumar and B. Sturtevant, The late-time development of the Richtmyer-Meshkov instability, Phys. Fluids 12, 2108 (2000).

D.I. Pullin, Contour dynamics method, Annu. Rev. Fluid Mech. 24, 89 (1992).

J. Reinaud, L. Joly, and P. Chassaing, The baroclinic instability of the two-dimensional shear layer, Phys. Fluids 12, 2489 (2000).

R.D. Richtmyer, Taylor instability in shock acceleration of compressible fluids, Comm. Pure and Appl. Math. 13, 297 (1960).

O. Sadot, L. Erez, U. Alon, D. Oron, L.A. Levin, G. Erez, G. Ben-Dor, and D. Shvarts, Study of nonlinear evolution of single-mode and two-bubble interaction under Richtmyer-Meshkov instability, Phys. Rev. Lett. 80, 1654 (1998).

R. Samtaney and N.J. Zabusky, Circulation deposition on shock-accelerated planar and curved density-stratified interfaces: models and scalings laws, J. Fluid Mech. 269, 45 (1994).

R. Samtaney and D.I. Pullin, On initial-value and self-similar solutions of the compressible Euler equations, Phys. Fluids 8, 2650 (1996).

R. Samtaney and N.J. Zabusky, Visualization, feature extraction and quantification of numerical visualizations of high gradient compressible flows, in Flow Visualization: Techniques and Example (eds. A.J. Smits and T. T. Lim), Chapter 12 (2000).

M. Soteriou and A.F. Ghoniem, Effects of the free-stream density ratio on free and forced spatially developing shear layers, Phys. Fluids 7, 2036 (1995).

C. Staquet, Two-dimensional secondary instability in a strongly stratified shear layer, J. Fluid Mech. 296, 73 (1995).

B. van Leer, Towards the ultimate conservative difference methods. J. Comput. Phys. 32, 101 (1979).

J.G. Wouchuk, Growth rate of the linear Richtmyer-Meshkov instability when a shock is reflected, Phys Rev E 63 056303 (2001).

J. Yang, T. Kubota, and E.E. Zukoski, Applications of shock induced-mixing to supersonic combustion, AIAA J. 31, 854 (1993.)

Y. Yang, Q. Zhang and D. H. Sharp. Small Amplitude Theory of Richtmyer-Meshkov Instability, Phys. of Fluids A, 5, 1856 (1994).

D.L. Youngs, Three-dimensional numerical simulations of turbulent mixing by Rayleigh – Taylor instability, Phys. Fluids A3, 1312 (1991).

N.J. Zabusky, Vortex paradigm for accelerated inhomogeneous flows: visiometrics for the Rayleigh-Taylor and Richtmyer-Meshkov environments, Annu. Rev. Fluid Mech. 31, 495 (1999).

N.J. Zabusky, N.J., Gupta, S., Samtaney, R. and Gulak, Y., Localization and spreading of contact discontinuity layers in simulations of compressible dissipationless flows. J. Comput. Phys. (2003)

N.J. Zabusky, A. Kotenlikov, Y. Gulak, and G. Peng, Amplitude growth rate of a Richtmyer-Meshkov unstable two-dimensional interface to intermediate times, J. Fluid Mech. 475, 147 (2003).

N.J. Zabusky, J. Ray, and R. Samtaney, Vortex models for the Richtmyer Meshkov instability, in Proceedings of the 5th International workshop on Physics of Compressible Turbulent Mixing, eds. R. Youngs, J. Glimm & B. Boyton, (1995).

S. Zhang, Richtmyer-Meshkov initiated, vortex accelerated inhomogeneous turbulence: high performance computing and visiometrics, Ph.D. thesis, Rutgers University, NJ, January, 2004.

Q. Zhang and S. Sohn, Nonlinear theory of unstable fluid mixing driver by shock wave, Phys. Fluids 9, 1106 (1997).

S. Zhang, N. J. Zabusky, G. Peng, and S. Gupta, Shock Gaseous Cylinder Interactions: Dynamically validated initial conditions provide excellent agreement between experiments and numerical simulations to late-intermediate time, Phys. Fluids 16, 1203 (2004).

Curriculum Vita

Gaozhu Peng

1995 - 1999 B.S. in Applied Mechanics, Peking University, Beijing, China

2000 - 2003 M.S. in Mechanical and Aerospace Engineering, Rutgers-The State University of New Jersey, N.J., U.S.A.

2003 - 2007 Ph.D. in Mechanical and Aerospace Engineering, Rutgers-The State University of New Jersey, N.J., U.S.A.

Journal Publications

Zabusky, N.J., Kotelnikov, A.D., Gulak, Y., and Peng, G. 2003, "Amplitude growth rate of a Richtmyer—Meshkov unstable two-dimensional interface to intermediate times," Journal of Fluid Mechanics 475, 147.

Peng, G., Zabusky, N.J., and Zhang, S. 2003, "Jet and vortex flows in a shock/hemispherical-bubble-on-wall configuration," Laser Particle Beams 21 (4), 449.

Peng, G., Zabusky, N.J., and Zhang, S. 2003, Vortex-accelerated secondary baroclinic vorticity deposition and late-intermediate time dynamics of a two-dimensional Richtmyer–Meshkov interface, Physics of Fluids 15 (12), 3730.

Zhang, S., Zabusky, N.J., Peng, G., and Gupta, S. 2004, "Shock gaseous cylinder interactions: Dynamically validated initial conditions provide excellent agreement between experiments and numerical simulations to late–intermediate time," Physics of Fluids 16 (5), 1203.

Zhang, S., Peng, G., and Zabusky, N.J., 2005, "Vortex bilayers, vortex projectiles and decaying inhomogeneous turbulence for shock – planar heavy curtain," Journal of Turbulence 6, N3, 1.

Lee, D-K., Peng, G. and Zabusky, N.J. 2006, “Circulation rate of change: A vortex approach for understanding accelerated inhomogeneous flows through intermediate times ,” Physics of Fluids 18, 097102.

Zabusky, N.J., Sun, Z. and Peng, G. 2006, “Measures of chaos and equipartition in integrable and nonintegrable lattices,” Chaos 16, 013130.

Conference Presentations

Peng, G., Zhu, H., Wu, J., and Yang, L. “Comparison of numerical simulation of wind load on tall buildings by the digital wind-tunnel with the test of aerodynamic wind-tunnel,” Proceedings of International Conference on Applied Computational Fluid Dynamics, Beijing, Oct 17-20, 2000 (Best Paper Award).

Peng, G., Gupta, S., Zhang, S. and Zabusky, N.J. “Dispersal of mass and circulation following shock-sphere and shock-cylinder interactions,” Proceedings of the 8th International Workshop on Physics of Compressible Turbulent Mixing (IWPCTM), Pasadena, CA, Dec 9 -14, 2001.

Zabusky, N.J., Gupta, S., Samtaney, R., Gulak, Y. and Peng, G. “Localization and spreading of interfaces (contact discontinuities) in PPM and WENO simulations of the inviscid compressible Euler equations,” Proceedings of the 8th International Workshop on Physics of Compressible Turbulent Mixing (IWPCTM), Pasadena, CA, Dec 9 -14, 2001.

Peng, G. and Zabusky, N.J. “Vortex and Jet Flows in a shock hemispherical bubble-on-wall Configuration,” 54th Meeting of American Physical Society/Division of Fluid Dynamics (APS/DFD), San Diego, CA, 2001.

Peng, G., Zabusky, N.J. and Zhang, S. “Secondary vorticity deposition and long-time dynamics of a Richtmyer-Meshkov interface,” 55th Meeting of American Physical Society/Division of Fluid Dynamics (APS/DFD), Dallas, TX, 2002.

Zhang, S., Zabusky, N.J. and Peng, G. “Blast wave/bubble interaction in 2D and 3D,” 55th Meeting of American Physical Society/Division of Fluid Dynamics (APS/DFD), Dallas, TX, 2002.

Zhang, S., Chen, J., Zabusky, N.J. and Peng, G. “Feature tracking analysis and inhomogeneous turbulence,” 56th Meeting of American Physical Society/Division of Fluid Dynamics (APS/DFD), Meadowland, NJ, 2003.

Peng, G., Bagchi, P. and Zabusky, N.J. “Leukocyte and endothelium interactions in shear flows: adhesion, rolling, cell deformability and morphology,” 57th Meeting of American Physical Society/Division of Fluid Dynamics (APS/DFD), Seattle, WA, 2004.

Zabusky, N.J. and Peng, G. “Vortex accelerated vorticity deposition and circulation growth-rate: Sinusoidal RM interface, shock-cylinder interaction and mixing layers,” 57th Meeting of American Physical Society/Division of Fluid Dynamics (APS/DFD), Seattle, WA, 2004.

Zabusky, N.J. and Peng, G. “Accelerated inhomogeneous (e.g. Richtmyer-Meshkov) flows: A-dot at intermediate times, vortex-accelerated vortex deposition and turbulence,” 57th Meeting of American Physical Society/Division of Fluid Dynamics (APS/DFD), Seattle, WA, 2004.

Peng, G. and Zabusky, N.J. “Numerical simulations of cell interactions under shear flows in complex geometries,” 58th Meeting of American Physical Society/Division of Fluid Dynamics (APS/DFD), Chicago, IL, 2005.

Zabusky, N.J. and Peng, G. “Scaling behavior for vorticity ‘drift’ form high-gradient interfaces in Richtmyer-Meshkov flows,” 58th Meeting of American Physical Society/Division of Fluid Dynamics (APS/DFD), Chicago, IL, 2005.

Bagchi, P., Doddi, S. and Peng, G. “Hydrodynamic interaction among blood cells in microcirculation”, 58th Meeting of American Physical Society/Division of Fluid Dynamics (APS/DFD), Chicago, IL, 2005.

Zabusky, N.J. and Peng, G. “Vorticity deposition and evolution in shock-accelerated flows: Analysis, Computation and Experiment”, Proceedings of the LANL symposium on Modeling and Simulation of Variable Density and Compressible Turbulent Mixing, Los Alamos National Laboratory, August 3-5, 2005.

Zabusky, N.J. and Peng, G. and Cook, A “Vorticity evolution and interaction at high-gradient interfaces in Richtmyer-Meshkov and Rayleigh-Taylor flows”, Proceedings of the 10th International Workshop on Physics of Compressible Turbulent Mixing (IWPCTM), Paris, France, June, 2006.

Zabusky, N.J. and Zhang, S. and Peng. G,” Vorticity deposition and evolution in shock-accelerated flows: Analysis, Computation and Experiment”, Symposium on Modeling and Simulation of Variable Density and Compressible Turbulent Mixing. Los Alamos National Lab, August 2005